INTERACTION

OF DROPLETS AND FOAMS WITH

SOLID/POROUS SUBSTRATES

by

Omid Arjmandi-Tash

A doctoral thesis submitted in partial fulfilment of the requirements for the award of Doctor of Philosophy of Loughborough University

February 2017

CERTIFICATE OF ORIGINALITY

This is to certify that I am responsible for the work submitted in this thesis, that the original work is my own except as specified in acknowledgements or in footnotes, and that neither the thesis nor the original work therein has been submitted to this or any other institution for a degree.

ABSTRACT

Current problems on the interaction of complex liquids (i.e. droplets or foams) with complex surfaces (i.e. soft deformable or porous surfaces) are addressed in the following areas: (1) wetting of deformable substrates and surface forces, (2) kinetics of wetting and spreading of non-Newtonian liquids over porous substrates, (3) kinetics of spreading of non-Newtonian solutions over hair, (4) free drainage of foams produced from non-Newtonian solutions, and (5) foam drainage placed on porous substrates.

Equilibrium of liquid droplets on deformable substrates was investigated and the effect of disjoining pressure action in the vicinity of the apparent three phase contact line was taken into account. It was proven that the deformation of soft solids is determined by the action of surface forces inside the transition zone.

Spreading/imbibition of blood, which is a power law shear thinning non-Newtonian liquid, over a dry porous layer was investigated from both theoretical and experimental points of view. It was found that blood droplet spreading/imbibition over porous substrates shows two different behaviours: (i) *partial wetting* case with three subsequent stages: initial fast spreading, constant maximum droplet base and the shrinkage of the droplet base; (ii) *complete wetting* case with only two stages: initial fast spreading and the shrinkage of the droplet base.

The wetting of hair tresses by aqueous solutions of two commercially available polymers, Aculyn^{TM} 22 (A22) and Aculyn^{TM} 33 (A33) was investigated experimentally. Both A22 and A33 solutions demonstrate well pronounced shear thinning behaviour. Initial contact angle of the A22 and A33 solutions on hair tresses was about 100^{o}. The A22 droplets remained on the hair tress after spreading for at least half an hour. However, a fast penetration of the A33 droplets inside the hair tresses was observed when advancing contact angle in the course of spreading reached a critical value of about 60^{o}. This could be explained by Cassie−Wenzel wetting transition which is caused by filling the pores inside the porous media by liquid.

The influence of non-Newtonian rheology of A22 and A33 solutions on foam drainage was also investigated experimentally and a new theory of foam drainage was presented for the case of free drainage. For lowly viscous polymeric solutions

and under the assumption of rigid surface of the Plateau border, the predicted values of the time evolution of the foam height and liquid content were in good agreement with the experimental data. However, in the case of highly viscous solutions an interfacial mobility at the surface of the Plateau border has to be taken into account.

A completely new theory of foam drainage placed on porous substrate was developed. It was found that there are three different regimes of the process: (i) a *rapid imbibition*, the imbibition into the porous substrate dominates as compared with the foam drainage; (ii) an *intermediate imbibition*, that is, the imbibition into the porous substrate and the rate of drainage are comparable; (iii) a *slow imbibition*, the rate of drainage inside the foam is higher than the imbibition into the porous substrate for a period of time and a free liquid layer is formed over the porous substrate.

ACKNOWLEDGEMENTS

I would like to express my sincere appreciation and gratitude to my supervisor, Prof Victor Starov, for his academic guidance and enthusiastic encouragement throughout these three years. I feel honoured to have had a chance to work with such a great scientist and learn from him. I really appreciate all his suggestions and advice during our never-ending meetings. He was definitely the best supervisor I have had so far during my education.

My special thanks goes to Dr Anna Trybala, my friend and my current co-supervisor for all her suggestions and strong supports during my PhD.

I am very thankful to my former co-supervisor, Dr Hemaka Bandulasena for his valuable guidance during the first two years of my PhD.

I really appreciate all the efforts and supports of Prof Tatiana Gambaryan-Roisman, the coordinator of CoWet project.

I would like to express my gratitude to my friends and colleagues, Dr Gulraiz Ahmad, Mr Pedro Santos-Silva, Dr Ali Nabavi, Dr Sina Saremi Yarahmadi, Dr Nina Kovalchuk, Dr Tzu Chieh Chao, Dr Faiz Mahdi and Dr Andrei Bureiko for their advice, supports and taking part in joint research.

This research was supported mainly by European Science Foundation Marie Curie ITN grant CoWet and partially by Engineering and Physical Research Council, UK grant EP/J010596/1; Procter & Gamble, USA; European Space Agency under grants PASTA and MAP EVAPORATION; and COST project MP1106.

Finally and most importantly, a huge “Thank you” to the love of my life, Nazli, for her unyielding devotion, patience and unwavering love, my beloved parents, and my brothers for their faith in me, encouragement and whole-hearted support.

TABLE OF CONTENTS

LIST OF FIGURES

LIST OF TABLES

CHAPTER 1

INTRODUCTION

1.1 Background

Complex liquids are binary mixtures of two phases, in which at least one phase is liquid. These binary mixtures might consist of solid and liquid phases (e.g. suspensions and polymer/surfactant solutions), gas and liquid phases (e.g. foams), or two immiscible liquid phases (e.g. emulsions).[1] Complex surfaces might include solid or soft substrates demonstrating chemical heterogeneities, porous structures or random topological patterns.[2]

Complex liquids are present in our everyday lives. They are widely utilised in food, cosmetics, pharmacy, mining, petroleum, chemical and environmental industries. The interaction of these complex liquids with complex surfaces occurs frequently not only in our daily lives but also in different technological advances.

Blood is a complex colloidal suspension. Blood samples can be collected using a complex thin porous surface such as cotton fibres, cellulous fibres or polymer membranes (dried blood spot sampling method). In this method of sampling, the blood droplets are preserved inside a complex porous layer as dried spot specimen.[3]

Many cosmetics such as skin-care creams and hair-care products are formulated to be applied on skin and hair which are complex surfaces. Complex polymer/surfactant solutions (in the form of droplets or foams) interact with human hair during application of shampoos, conditioners or hair colorants.[4]

Recent investigations have confirmed that foam, which is a complex liquid, is an efficient alternative method of drug delivery on the skin of patients (a complex surface). Although lotions, creams, gels and ointment are the most common topical vehicle delivery systems, foams are delivery systems which grow in popularity in dermatology.[5-8]

In addition, the contact between complex liquids and complex surfaces takes place in many conventional, and modern micro- and nanotechnologies including micro- and nanofluidics, micro-electromechanical systems, functional printing and coating,

and regeneration medicine. In these technologies, complex liquids and surfaces are exploited to control, optimize and build up new technological processes.[9-12]

In all the above-mentioned examples, understanding the interaction between complex liquids and complex surfaces at interfaces at different nano, meso and macro length scales is essential in order to enhance product quality and functionality in multidisciplinary applications. In addition, the interaction condition of complex liquids with complex surfaces is very important because, for example in some cases, it can affect the kinetics of delivery of active substances from complex liquids to the target places inside the complex surfaces. In order to make a proper choice of the process parameters and improve the performance of the system, the properties of the complex liquids should be considered in connection with the properties of complex surfaces.

1.2 Aims and objectives

The aim of this research focuses around expanding our understanding of complex liquids (in the form of droplets and foams) and their interactions with complex surfaces (such as soft solid and porous substrates) at interfaces from the view point of different length scales. Such interfaces and the related interfacial phenomena are widespread in our routine lives, many industrial applications, and established and novel technologies.

In particular, the aims of this thesis work can be summarized in the following different research packages:

- Develop an understanding and a mathematical modelling of equilibrium of droplets over a soft solid substrate as a complex surface, and find the effect of fundamental factors, and different parameters and forces, especially surface forces action on the equilibrium contact angle and the deformation of soft deformable substrate.
- Investigate the kinetics of wetting and spreading of blood droplets as a complex non-Newtonian liquid over different thin porous substrates from both theoretical and experimental points of view. This process is a representation of dried blood spot sampling method.
- Develop an experimental method to investigate wetting and spreading of two commercially available non-Newtonian polymeric solutions, Aculyn™ 22

and Aculyn^{TM} 33, over hair tresses. These polymeric solutions are widely used in hair-care and cosmetic products.

- Develop a mathematical modelling for the free drainage of foams produced from the above-mentioned non-Newtonian polymeric solutions and compare the predicted results with the measured experimental data.
- Develop a new theory of interaction of foam, as a complex liquid, with a porous substrate, as a complex surface, and investigate the parameters affecting the kinetics of release of liquid from foam into the pores of porous media.

1.3 Thesis layout

The thesis has been written in eight chapters. Chapter 1 is an introduction, which is followed by a literature review in Chapter 2. Chapters 3 to 7 present the theoretical modeling, experimental methods and the results of the research. All the findings presented in theses chapters have been published in 9 peer-reviewed journals (shown in the next section). The descriptions of each chapter are given below:

- Chapter 1 is an introduction of background and problems which require to be addressed, and it mentions the motivation for the current research. Furthermore, it presents the aims and objectives, and the layout of the thesis.
- Chapter 2 is a literature review of fundamental researches on the interaction of liquids in the form of droplets or foams with solid/porous substrates. It presents the theoretical and experimental findings in three different sections: (i) It starts by fundamental description of wettability, the equilibrium condition of a liquid droplet over solid substrate and the effect of surface forces action in the vicinity of three-phase contact line. (ii) It continues by introducing the available theories on the moving contact line and the dynamic contact angle, and the current problems and investigations on the kinetics of wetting and spreading of droplets over different substrates. (iii) In the last section of the literature review basic definitions about foam, foam geometry and foam drainage are reviewed and then the interaction of foam with porous surfaces is discussed.

- Chapter 3 presents a mathematical model for equilibrium wetting of a soft solid substrate by a liquid droplet and it focuses on the effect of surface forces action on the equilibrium contact angle, and the profiles of both the droplet and the soft solid substrate underneath.
- Chapter 4 starts with a description of the difference between partial wetting and complete wetting of a porous substrate by a liquid droplet and then it continues with developing a mathematical model for the kinetics of wetting and spreading of non-Newtonian blood droplets over porous substrates in the case of complete wetting. The last section is dedicated to analyse the experimental data and compare them with the predicted results.
- Chapter 5 presents the experimental method and results of wetting and spreading of non-Newtonian polymeric solutions, Aculyn^{TM} 22 and Aculyn^{TM} 33, on hair tresses.
- Chapter 6 presents a mathematical model for the free drainage of foams produced from power-law non-Newtonian liquids and then it draws a comparison between the predicted results and the measured experimental data for the drainage of foams formed by the above-mentioned polymeric solutions.
- Chapter 7 introduces a completely new theory of foam drainage placed on a porous substrate and then it predicts different regimes for the process based on the effect of different parameters related to the properties of both the foam and the porous substrate.
- Chapter 8 shows the main conclusions of the thesis, and gives some recommendations for future studies.

1.4 Dissemination from the PhD thesis

1.4.1 Peer-reviewed journal publications

1. O. Arjmandi-Tash, N. Kovalchuk, A. Trybala, I. Kuchin, V. Starov, “kinetics of wetting and spreading over various surfaces”, Langmuir, 2017, Invited Feature Article (Just Accepted). **Chapter 3, 4** and **5**.

2. O. Arjmandi-Tash, A. Trybala, F. M. Mahdi, N. Kovalchuk, V. Starov, “Foam free drainage of non-Newtonian polymeric solutions”, Colloids and Surfaces A: Physicochemical and Engineering Aspects, 2016 (In press). **Chapter 6**.
3. G. Ahmed, V. V. Kalinin, O. Arjmandi-Tash, V. Starov, “Equilibrium of droplets on a deformable substrate: Influence of disjoining pressure”, Colloids and Surfaces A: Physicochemical and Engineering Aspects, 2016 (In press). **Chapter 3**.
4. T. C. Chao, O. Arjmandi-Tash, D. B. Das, V. Starov, “Simultaneous spreading and imbibition of blood droplets over porous substrates: partial wetting”, Colloids and Surfaces A: Physicochemical and Engineering Aspects, 2016, 505, 9-17. **Chapter 4**.
5. A. Trybala, A. Bureiko, N. Kovalchuk, O. Arjmandi-Tash, Z. Liu, V. Starov, “Wetting properties of cosmetic polymeric solutions on hair tresses”, Colloids and Interface Science Communications, 2015, 9, 12-15. **Chapter 5**.
6. O. Arjmandi-Tash, N. Kovalchuk, A. Trybala, V. Starov, “Foam drainage placed on a porous substrate”, Soft Matter, 2015, 11, 3643-3652. **Chapter 7**.
7. A. Bureiko, O. Arjmandi-Tash, N. Kovalchuk, A. Trybala, V. Starov, “Interaction of foam with a porous medium: theory and calculations”, The European Physical Journal Special Topics, 2015, 224, 459-471. **Chapter 7**.
8. T. C. Chao, O. Arjmandi-Tash, D. B. Das, V. Starov, “Spreading of blood drops over dry porous substrate: complete wetting case”, Journal of Colloid and Interface Science, 2015, 446, 218-225. **Chapter 4**.
9. N. Kovalchuk, A. Trybala, O. Arjmandi-Tash, V. Starov, “Surfactant enhanced spreading: experimental achievements and possible mechanisms”, Advances in Colloid and Interface Science, 2016, 233, 155-160.
10. A. Trybala, O. Arjmandi-Tash, N. Kovalchuk, V. Starov, “Spearing and evaporation of blood”, Advances in Colloid and Interface Science, 2017, (Under review).
11. O. Arjmandi-Tash, A. Trybala, V. Starov, “Foam drainage on a thin porous substrate”, Langmuir, 2017, (In preparation).

1.4.2 Invited oral presentations

1. Staff/Student Seminar at Department of Chemical Engineering, Loughborough University, Loughborough, UK, October 2016, Topic: Interaction of droplets and foams with porous substrate.
2. Seminar at P&G Beauty Care Research & Development, Procter & Gamble Company, Cincinnati, Ohio, US, October 2016, Topic: Foam drainage on porous substrate.

1.4.3 Oral presentations

1. O. Arjmandi-Tash, S. Subramanian, F. M. Mahdi, A. Trybala, N. M. Kovalchuk, V. Starov "Foam Drainage: Free and Interaction with Porous Substrates", ECIS-2016, Rome, Italy.
2. O. Arjmandi-Tash, V. Starov, "Interaction of foams with a porous support", CoWet Winter Training school- 2016, Madrid, Spain.
3. O. Arjmandi-Tash, A. Trybala, F. M. Mahdi, V. Starov, "Free drainage of non-Newtonian foams", SGIC-2016, Athens, Greece.
4. O. Arjmandi-Tash, V. Starov, "Interaction of foams with a porous support", CoWet Winter Training school- 2016, Mainz, Germany.
5. O. Arjmandi-Tash, N. Kovalchuk, A. Trybala, A. Bureiko, V. Starov, "Polymer foams in hair care products", Haircare & Transplantation 2015, Philadelphia, USA.
6. O. Arjmandi-Tash, T. C. Chao, V. Starov, D. B. Das, "Spreading of Blood over Porous Substrate", B&D2015, Potsdam-Golm, Germany.
7. O. Arjmandi-Tash, V. Starov, "Interaction of foams with a porous support", CoWet Sumer Training School-2015, Madrid, Spain.
8. O. Arjmandi-Tash, V. Starov, "Interaction of foams with a porous support", CoWet Winter School-2015, Loughborough, UK.

1.4.4 Poster presentations

1. O. Arjmandi-Tash, T. C. Chao, D. B. Das, V. Starov "Blood droplet spreading/imbibition over porous substrates: complete and partial wetting", ECIS-2016, Rome, Italy.

2. T. C. Chao, O. Arjmandi-Tash, D. B. Das, V. Starov “Partial wetting of porous substrates by blood droplets”, IMA8-2016, Bad Honnef, Germany.
3. O. Arjmandi-Tash, V. Starov, “Interaction of foams with a porous support”, CoWet Winter Training school- 2016, Mainz, Germany.
4. O. Arjmandi-Tash, V. Starov. “Interaction of foams with a porous support”, Inspiring Research-2015, Loughborough University, Loughborough, UK.
5. O. Arjmandi-Tash, V. Starov, “Interaction of foams with a porous support”, CoWet Sumer Training School-2015, Madrid, Spain.
6. O. Arjmandi-Tash, V. Starov, T. C. Chao, D. B. Das, “Spreading of Blood Drops over Dry Porous Substrate: Complete Wetting Case”, IACIS 2015, Mainz, Germany.
7. O. Arjmandi-Tash, V. Starov, “Foam Drainage in Presence of a Porous Support: Theory and Computer Simulations”, Nanotechnology-2015, Dubai, UAE.
8. O. Arjmandi-Tash, V. Starov, “Interaction of foams with a porous support”, CoWet Winter School-2015, Loughborough, UK.

1.4.5 Awards and prizes

- **Contribution to Knowledge award**, awarded by Loughborough University, Loughborough, UK.
- **Travel Grant** from European Cooperation in Science and Technology (COST MP1106) for participating in Smart and Green Interfaces Conference held in Athens, Greece.

CHAPTER 2

LITERATURE RIVIEW

Overview

In this chapter theoretical and experimental findings on the interaction of droplets or foams with solid/porous substrates will be reviewed. In the first section, equilibrium of droplets over solid substrates will be discussed and the effect of surface forces action in the vicinity of three-phase contact line will be demonstrated. The available theories on the moving contact line and the dynamic contact angle, and the current problems and investigations on the kinetics of wetting and spreading of droplets over different substrates will be presented in the second section. In the third section, firstly some basic definitions about foam, foam geometry and foam drainage will be reviewed and then the interaction of foam with porous surfaces will be discussed.

2.1 Equilibrium of droplets over solid substrates and surface forces

Wettability or the equilibrium condition of a liquid droplet over solid substrate is frequently described using the well-known Young equation:

$$\mathrm{Cos}\,\theta_e = \frac{\gamma_{sv} - \gamma_{sl}}{\gamma}, \tag{2.1}$$

where γ, γ_{sv} and γ_{sl} are liquid-vapour, solid-vapour and solid-liquid interfacial tensions, respectively. This equation relates the three interfacial tensions to the contact angle of the droplet over solid surfaces. This contact angle is an important parameter in interface science as it is a representation of hydrophobicity or hydrophilicity of a solid substrate. According to the value of contact angle, a droplet shows three different behaviours over a solid substrate:[13,14] (i) nonwetting behaviour, in which the equilibrium contact angle is higher than 90° (Fig. 2.1(a)), for example an aqueous droplet over Teflon; (ii) partial wetting behaviour, the equilibrium contact angle is less than 90° (Fig. 2.1(b)), for example in the case of aqueous droplet over glass or mica, and (iii) complete wetting behaviour, in which droplet spreads out completely over the surface and there is dynamic contact angle,

θ_d (t), which normally decreases over the time of spreading (Fig. 2.1(c)), for example, oil droplet on a glass substrate or aqueous droplets on a hydrophilized silicon wafer.

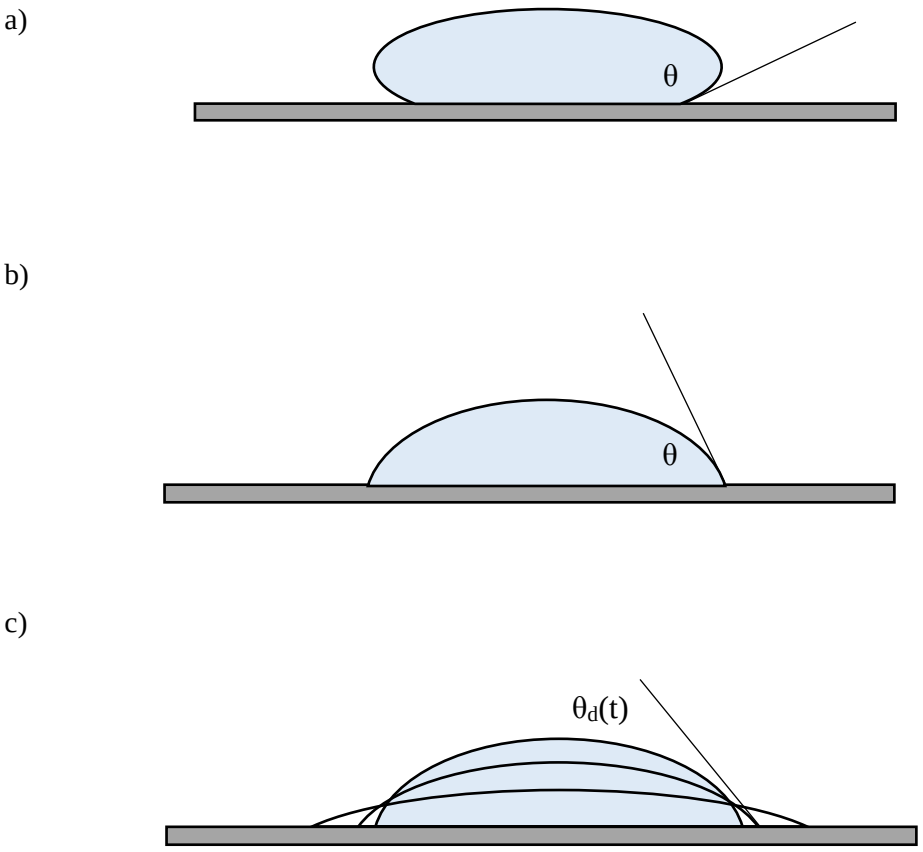

Figure 2.1: Three different behaviours of droplets over solid substrates: a) nonwetting case, contact angle is bigger than 90°; b) partial wetting case, contact angle is in between 0 and 90° and c) complete wetting case, the droplets spreads out completely with dynamic contact angle.

Eq. (2.1) is simply the balance of horizontal forces at the three-phase contact line. It indicates that the complete wetting behaviour corresponds to the cases in which $\gamma_{sv} > \gamma_{sl} + \gamma$, that is, all the forces in horizontal direction cannot be compensated at any contact angle; partial wetting case is related to $0 < \text{Cos } \theta_e < 1$, and nonwetting behaviour corresponds to the cases in which, $-1 < \text{Cos } \theta_e < 0$. Taking into account the previous consideration, it seems that the above mentioned three different

behaviours, complete wetting, partial wetting and nonwetting cases can be determined using the values of the three interfacial tensions γ_{sl}, γ_{sv} and γ. However, the problem is more complex than this because the quantities γ_{sl} and γ_{sv} cannot be directly measured. Therefore, Eq. (2.1) gives only a qualitative description of the behaviour of the system, which is often used for solving the inverse problem, that is, determining $\gamma_{sv} - \gamma_{sl}$ by means of experimental values of γ and θ.[13,14]

According to[14] an alternative to Eq. (2.1) is to consider equilibrium liquid profile in the vicinity of the apparent three-phase contact line, where there is the action of surface forces. Surface forces are well-known in colloid and interface science, where they are widely used to determine the behaviour and properties of colloidal suspensions and emulsions, such as stability, instability, interactions, rheology and so on.[15] DLVO theory is commonly used to rationalize forces acting between interfaces, colloidal particles or droplets.[15] The range of action of surface forces is generally in the order of 0.1 μm;[15] therefore, surface forces play a role in the vicinity of three phase contact line, where the liquid profile tends to be of zero thickness.

2.1.1 Disjoining/conjoining pressure and its components

Disjoining/conjoining pressure is a manifestation of the action of surface forces, which indicates the behaviour of liquid profile close to the solid substrates. Although several physical phenomena contribute to the appearance of disjoining/conjoining pressure, it has been shown in[15] that the main features of disjoining/conjoining pressure isotherm can be well captured by three additive contributions:

1) The electrostatic component arising from the overlapping of the electrical double layers:

$$\Pi_E = RTc_0(\exp(\varphi) + \exp(-\varphi)) - 2RTc_0 - \frac{(RT)^2\varepsilon\varepsilon_0}{2F^2}\left(\frac{\partial\varphi}{\partial y}\right)^2, \quad (2.2)$$

where R is universal gas constant, T is temperature in ^{o}K and, F is Faraday's constant; ε and ε_0 are respectively dielectric constants of water and vacuum; c_0 is electrolyte concentration; y is the coordinate normal to the liquid-vapor interface, and φ is dimensionless electric potential in F/RT unit.

The electric potential φ in Eq. (2.2) is related to the surface charge density σ as[15]

$\sigma_h = \varepsilon\varepsilon_0 \frac{RT}{F}\left(\frac{\partial\varphi}{\partial y}\right)_{y=h}$ for the liquid/vapour interface;

$\sigma_s = -\varepsilon\varepsilon_0 \frac{RT}{F}\left(\frac{\partial\varphi}{\partial y}\right)_{y=0}$ for the solid/liquid interface;

2) The structural component is usually related to the interfacial layers as a result of water molecule dipoles orientation.

This component is considered in[16] by the following two terms expression:

$$\Pi_S = K_1 \exp(-h/\lambda_1) + K_2 \exp(-h/\lambda_2)\,, \tag{2.3}$$

where K_1, K_2 and λ_1, λ_2 are the experimental constants corresponding to a magnitude and characteristic length of the short-range (1) and long-range (2) structural interactions, respectively;

3) The van der Waals or molecular dispersion component:[15]

$$\Pi_M(h) = \frac{A}{6\pi h^3}\,, \tag{2.4}$$

where $A = -A_H$, A_H is the Hamaker constant. It should be noted that the van der Waals component effect is greatly exaggerated in most of the literature.[14] $\Pi_M(h) \to \infty$ at $h \to 0$, however, disjoining/conjoining pressure is a macroscopic value, that is valid only at $h >>$ molecular dimension. Under the latter condition and for aqueous solutions, other components of the disjoining/conjoining pressure contribute equally or more than the van der Waals component.

The sum of the above-mentioned components leads to the following disjoining/conjoining pressure isotherm:[15, 16]

$$\Pi(h) = \Pi_M(h) + \Pi_E(h) + \Pi_S(h) \tag{2.5}$$

Schematic presentation of three possible shapes of disjoining/conjoining pressure isotherms is given in Fig. 2.2.[14] Curve 1 in Fig. 2.2 corresponds to the complete wetting case where the attractive van der Waals component play a significant role. Curve 2 corresponds to the partial wetting case in which disjoining/conjoining pressure is the sum of three above-mentioned components as is shown in Eq. (2.5): electrostatic, structural and dispersion components. These three components lead to a S-shaped isotherm as is illustrated in curve 2 in Fig. 2.2. Curve 3 corresponds to non-wetting cases.

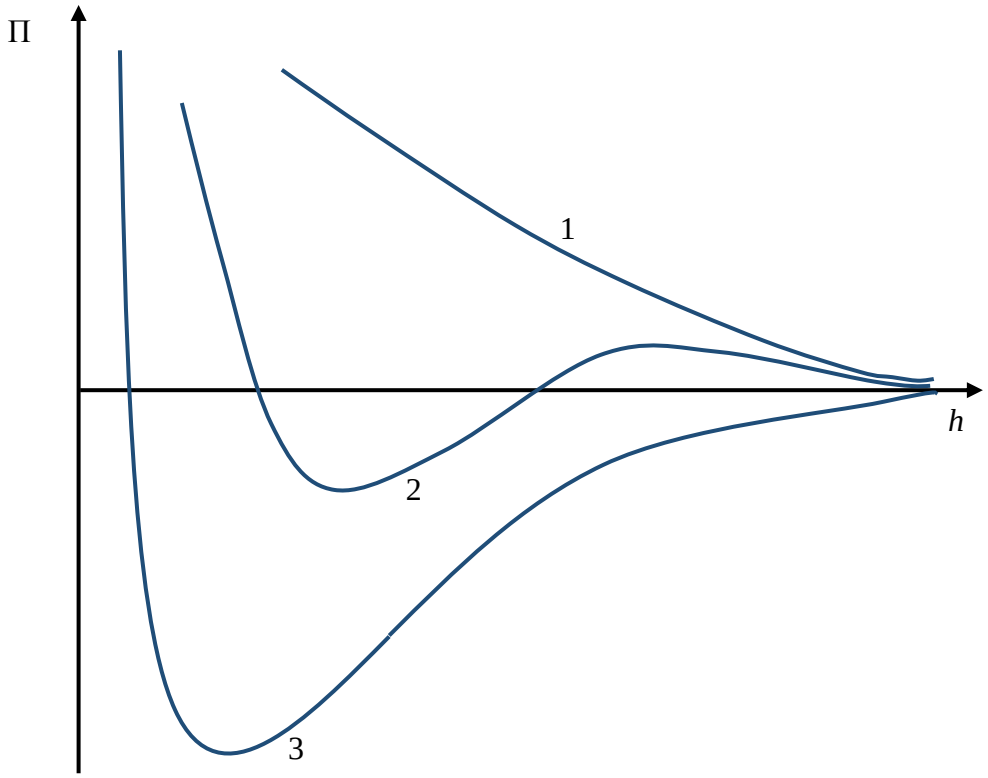

Figure 2.2: Schematic presentation of three types of disjoining/conjoining pressure isotherms: 1) complete wetting case, 2) partial wetting case and 3) nonwetting case.[14]

2.1.2 Thermodynamic equilibrium and its conditions

A droplet on homogenous flat solid substrate reaches a thermodynamic equilibrium if the chemical potentials of liquid molecules in the whole system are equal and taking into account the latter consideration the following three equilibrium conditions should be satisfied:[14]

1) Equilibrium of liquid in the droplet with its vapour phase
2) Equilibrium of vapour phase with the solid substrate
3) Equilibrium of liquid in the droplet with the solid substrate

The first condition is satisfied if the chemical potential of liquid molecules inside the drop is equal to the chemical potential of liquid molecules in the ambient vapour phase. This equality leads to the so-called Kelvin's equation:[17]

$$P_e = \frac{RT}{v_m} \ln \frac{p_{sat}}{p}, \tag{2.6}$$

where $P_e = P_v - P_l$, P_v is the pressure in the vapour phase, P_l is the pressure in the liquid phase; R is the gas universal; T is the temperature in K; v_m is the molar volume of the liquid, p is vapour pressure at equilibrium with the liquid drop and p_{sat} is the saturated vapour pressure at temperature T.

For a droplet which has a convex curvature, pressure inside the droplet is higher than the pressure in the ambient vapour phase; therefore, the excess pressure inside the droplet, P_e, has a negative value. Accordingly, the left hand side of Eq. (2.6) is negative and for the sake of equality the p should be bigger than $p_{sat,}$ in the right hand side of the equation. The latter means that the droplet can be at equilibrium only with over-saturated vapour.[14]

According to[14] there is an adsorbed liquid film (a monolayer or several layers of the adsorbed liquid molecules) on the solid substrate. Starov et al. showed that this adsorbed liquid film is required to satisfy the second condition of the thermodynamic equilibrium and it is impossible for a bare solid substrate without the adsorbed liquid film to be at the thermodynamic equilibrium with the vapour in the surrounding air.[14]

The third thermodynamic equilibrium condition requires the minimization of the excess free energy of the liquid droplet over solid substrate. The excess free energy of a two dimensional cylindrical droplet with a negligible action of gravity is:[13,14,18]

$$\Phi = \gamma S_e + P_e V_e + F_{surface\ forces} \tag{2.7}$$

where S_e and V_e are the excess of the liquid-vapour surface area and the excess of the volume, respectively, and $F_{surface\ forces}$ is the excess free energy associated with the action of surface forces.

Using the unknown profile of the liquid droplet, $h(x)$, Eq. (2.7) can be rewritten as:[14]

$$\Phi = \int_0^\infty f(h, h')dx, \tag{2.8}$$

where

$$f(h, h') = \left[\begin{array}{c} \gamma\left(\sqrt{1 + h'^2} - 1\right) + P_e(h - h_e) \\ + \int_h^\infty \Pi(h)dh - \int_{h_e}^\infty \Pi(h)dh \end{array} \right]. \tag{2.9}$$

In above equations x is the tangential coordinate and h_e is the equilibrium thickness of the adsorbed liquid film on the solid substrate (which was described earlier).

Under equilibrium conditions the excess free energy, Eq. (2.8), should reach minimum value. To satisfy this condition the first variation of excess free energy, Eq. (2.8), should be zero, which results in an Euler equation and it gives an equation for the droplet profile under the equilibrium conditions:[14]

$$\frac{\partial f}{\partial h} - \frac{d}{dx}\frac{\partial f}{\partial h'} = 0, \tag{2.10}$$

or

$$\frac{\gamma h''}{(1 + h'^2)^{3/2}} + \Pi(h) = P_e. \tag{2.11}$$

Eq. (2.11) is the well-known Laplace-Derjaguin equation and its first term in left hand side relates to the capillary pressure action and the second term corresponds to the action of disjoining/conjoining pressure. As mentioned earlier the range of surface forces action is in the order of 0.1 μm, that is, far from the three phase contact line where h>> 0.1 μm, the action of disjoining/conjoining pressure can be neglected.

2.1.3 Equilibrium contact angle on a non-deformable substrate and surface forces

According to the above-mentioned thermodynamic equilibrium conditions, Starov et al. described an overall profile for a droplet on a solid substrate with three subdivided regions (Fig. 2.3):[14] 1) a spherical cap region where is outside the range of surface forces action, 2) a transition zone, in which both capillary and surfaces forces are important, and 3) an adsorbed equilibrium liquid film on the solid substrate ahead of the droplet.

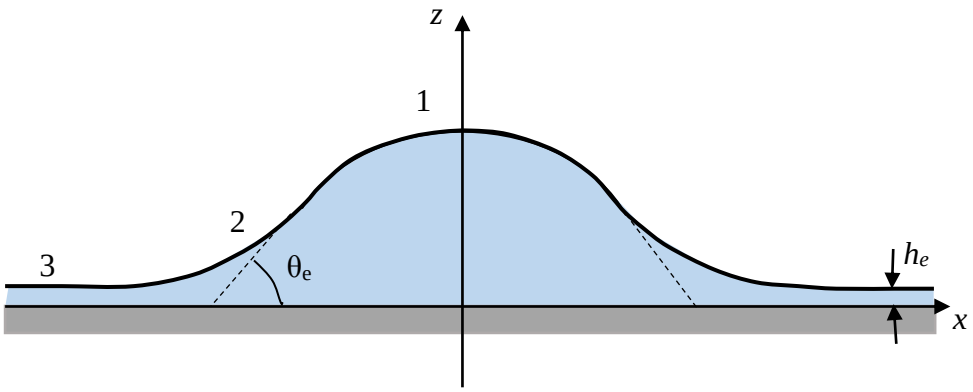

Figure 2.3: Equilibrium droplet over solid substrate, 1- Spherical cap, in which capillary force dominates, 2- Transition zone, in which both capillary and surfaces forces are important, 3- an adsorbed equilibrium liquid film ahead of droplet.[14]

In the case of partial wetting, that is, equilibrium contact angle, $\theta_e > 0$, the shape of the transition zone between the spherical cap region and the thin adsorbed liquid film on a solid substrate can be expressed via the disjoining pressure isotherm, $\Pi(h)$.[14] The equilibrium excess pressure, P_e, inside the droplet can be expressed according to Kelvin's equation and the equilibrium contact angle of a two dimensional droplet can be expressed using the well-known Derjaguin–Frumkin equation:[14]

$$\cos\theta_e = 1 + \frac{\Pi(h_e)h_e}{\gamma} + \frac{1}{\gamma}\int_{h_e}^{\infty}\Pi(h)dh. \qquad (2.12)$$

The latter equation determines the equilibrium contact angle using measurable physical properties, that is, surface forces action in the vicinity of the three phase contact line.

In chapter 3 the above mentioned approach for the equilibrium of droplet over non-deformable solid substrate is applied to the case of deformable solid substrate and the effect of surface forces on the equilibrium contact angle and deformation of soft deformable substrate is investigated.

2.2 Kinetics of wetting and spreading of droplets over solid substrates

In the previous section, equilibrium of droplets over solid substrates has been discussed and the action of surface forces in the vicinity of three-phase contact line has been demonstrated. In this section the current theories and investigations on the kinetics of wetting and spreading of droplets over different substrates will be discussed.

Wetting and spreading of liquids over solid surfaces has been investigated in the literature from both theoretical and experimental points of view.[14,19-29] Spreading dynamics and contact line motion have been described by several theoretical models, which can be categorised into hydrodynamic models[24,26,27,30-37] and molecular kinetic theory models[19,38,39].

In hydrodynamic models, it is well known that singularity appears at three phase contact line if a non-slip boundary condition is used to solve the Navier-Stokes equations. To address this issue the moving contact line region is divided into different zones and several microscopic hypotheses such as precursor film,[40] slip conditions,[24] diffusion interface[36,41-48] and non-Newtonian effects[34,49-51] are proposed to remove the singularity at the three-phase contact line.

In molecular kinetic theory models, the drop spreading is regarded as adsorption/desorption of molecules in the moving contact line region where energy dissipation occurs due to this adsorption/desorption process of fluid particles on solid substrate (Fig. 2.4). A combination of both hydrodynamic models and molecular kinetic theory models is also proposed in the literature[52-54] for spreading of liquids over solid surfaces.

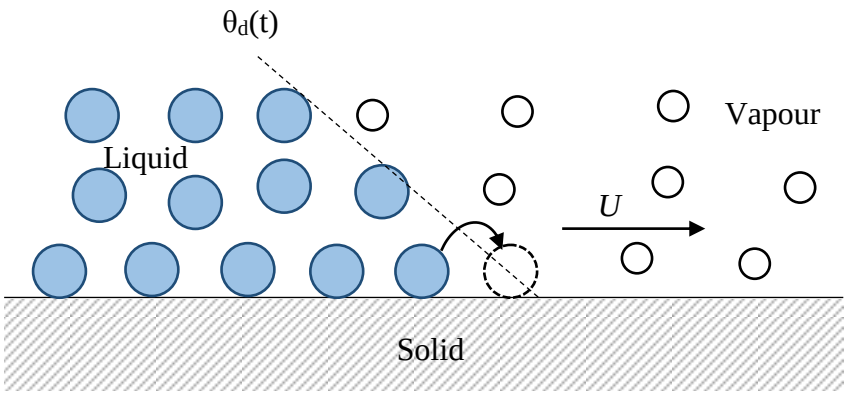

Figure 2.4: Schematic of adsorption/desorption of molecules in the vicinity of moving contact line in molecular kinetic theory models.[19,39]

In a number of the approaches the kinetics of wetting is described without consideration of surface forces acting in the vicinity of three-phase moving contact line. The commonly used approach is the one based on Blake and Haynes model[39] which was applied later for the case of electrowetting[55] and it suggests surface diffusion as a driving force for spreading (molecular kinetic theory models shown in Fig. 2.4). According to[39] surface diffusion leads to an effective slippage and it eliminates the friction singularity at the moving three-phase contact line.

Starov et al.[14] suggested the application of the previously discussed hypothesis in the case of equilibrium based on the effect of surface forces action in the vicinity of the three-phase contact line (generally explained in Section 2.1), to the case of wetting dynamics. Accordingly, the whole part in the vicinity of three-phase contact line was magnified and subdivided into four regions (Fig.2.5):[14,56] 1) a spherical cap region in the bulk of the spreading droplet, which is included to demonstrate the dynamic contact angle, $\theta_d(t)$, after matching all the regions illustrated in Fig. 2.5; 2) Region 2, in which the hydrodynamic flow deforms the spherical cap shape; 3) Region 3, in which disjoining/conjoining pressure comes into play and its action is becoming more important than the capillary forces as the profile reaches the solid substrate. Surface forces action dominates and becomes the only driving force for the spreading at the end of Region 3. 4) Surface diffusion region, where the macroscopic description of the spreading process is impossible and its characteristic length scale in the direction of the surface normal is in the order of the molecular size.

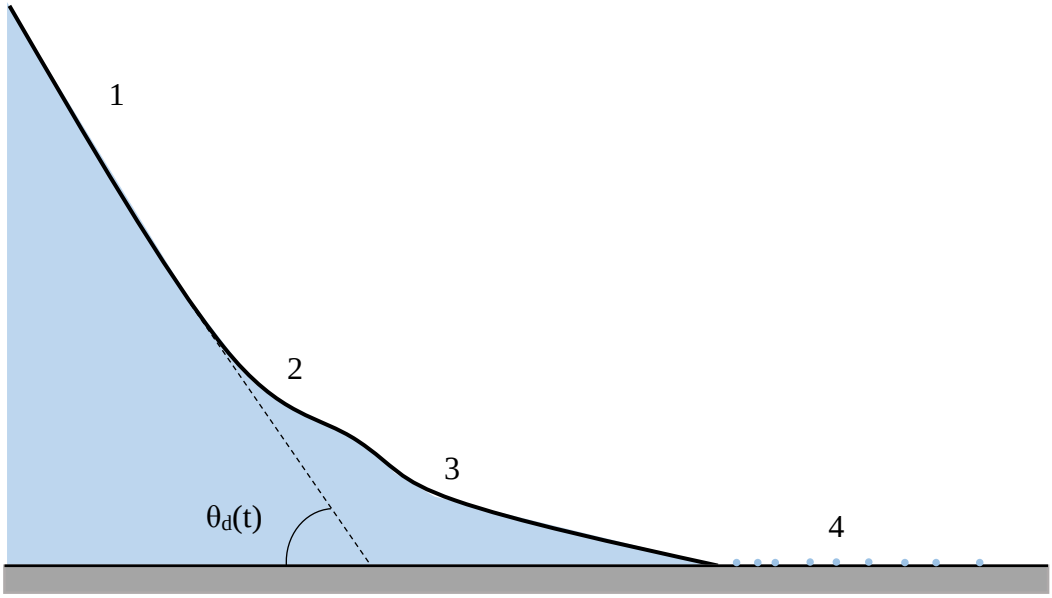

Figure 2.5: A magnified schematic of the vicinity of the moving three-phase contact line in the case of complete wetting with a dynamic contact angle: 1- a spherical cap part of the droplet which shows the dynamic contact angle, $\theta_d(t)$, by intersection of its tangent with the solid substrate; 2- region of the deformed spherical shape by the action of the hydrodynamic force; 3- region of the action of surface forces in which this action is becoming more important than the capillary pressure as the profile reaches the solid substrate; 4- surface diffusion region, where the macroscopic description of the spreading process is impossible.[14]

In[26] the theory of the spreading of an axisymmetric Newtonian liquid droplet over a plane solid substrate is developed and the predicted results showed a good agreement with the available experimental data. Both disjoining/conjoining and capillary pressures were taken into account and it has been established that a singularity at the three phase contact line can be removed by the action of surface forces.[26,27]

As discussed above, wetting and spreading of pure Newtonian liquids over solid surfaces has been well documented in the literature. However, most commonly found liquids in our everyday life such as blood, shampoos, hair colorants and paints are colloidal suspensions or polymeric solutions which show non-Newtonian behaviour. Furthermore, the surfaces where these solutions are commonly applied are porous such as skin, hair tresses or textile materials. Wetting and spreading of non-Newtonian liquids over smooth homogeneous surfaces have been theoretically investigated in the literature using both hydrodynamic[57-61] and molecular kinetic

theory models[62]. However, the spreading and wetting conditions of a drop on a porous substrate are obviously different due to the presence of a porous layer. This process has been investigated in the case of spreading/imbibition of Newtonian liquids.[63-65]

Wetting and spreading of biological fluids have been less widely studied in spite of the potential applications in medical science. Brutin et al.[66-69] investigated the wetting, spreading and evaporation dynamics of blood droplets, which show a shear thinning non-Newtonian behaviour, over solid surfaces. They found a spreading law of $L \sim t^{0.65}$ (where L is the radius of the drop base) at early stages of spreading in which the process is controlled by a competition between viscous and surface tension forces while at later stages of spreading, the spreading exponent ($L \sim t^{0.19}$) was higher than that of Tanner's law (i.e. $L \sim t^{0.1}$) due to the effect of Marangoni stresses and humidity.

In chapter 4, theoretical and experimental findings on kinetics of wetting and spreading of blood, a non-Newtonian colloidal suspension, over different thin porous substrates are presented, while in chapter 5 wetting and spreading of two commercially available non-Newtonian polymeric solutions, Aculyn™ 22 and Aculyn™ 33, on hair tresses are investigated experimentally.

2.3 Foam and foam drainage, and interaction with porous surfaces

In the previous sections, equilibrium and dynamic interaction of droplets with solid/porous surfaces has been discussed, and some of the current problems and the available theories on the wetting and spreading of droplet over solid/porous substrates were reviewed. In this section, in order to investigate the interaction of foams with porous surfaces, some of the properties of foam like foam drainage will be reviewed and the application of foam interaction with porous surfaces will be discussed.

Foams are multiphase colloidal systems, which are formed by trapping a gas in a continuous phase (liquid or a solid). Foams are widely used in personal care products and they often arise during cleaning and dispensing processes. They pop up in lightweight mechanical materials and affect absorbing components in cars, heat exchangers and textured wallpapers. Foams are widely utilised in food, cosmetics,

pharmacy, mining, petroleum and gas industries.[70-72] That is why they attract scientific attention already over many decades.[73-79]

A liquid foam consists of packed bubbles which are separated by liquid phase. The amount of liquid within the foam can be represented by liquid volume fraction, $\varphi = V_{liq}/V_{foam}$, where V_{liq} is the volume of liquid dispersed in a foam with a volume of V_{foam}. A foam can have a liquid volume fraction from about zero to 26-36%, the maximum limiting value, at which the packed deformed bubbles split into individual bubbles and retain their spherical shape.[74,80] Although foams are composed of a complex disordered structure, it turns out that dry foams (i.e. low liquid volume fraction) can be classified as the following three distinct interconnected elements (Fig. 2.6) with simplified and exact geometries (Kelvin bubbles):[80]

1) Films or lamellaes, which are the regions between two compressed bubbles and separate them from each other.
2) Channels or Plateau borders, which are the liquid-filled volumes between three compressed bubbles, or the regions at intersection of three films or lamellaes.
3) Nodes or junctions, which are the liquid-filled volumes between four compressed bubbles, or the regions at intersection of four channels or Plateau borders.

The liquid flow in between the gas bubbles through Plateau borders, nodes and films in foam driven by capillarity and/or gravity forces is referred to as drainage (Fig. 2.6). In the case of foams built up by Newtonian liquids, equations of drainage were deduced using the combination of the liquid momentum and mass balance equations.[81-85] The drainage equations in the case of Newtonian liquids have been solved numerically and/or analytically in different prototype situations including free drainage, where liquid drains out of a foam due to the influence of gravity and capillarity,[81-86] wetting of a dry foam, where a dry foam is in contact with a liquid at its base and the liquid rises to the top by capillarity,[87,88] forced drainage, where liquid is added to the top of foam column producing a traveling wave,[85,86,89-91] and pulsed drainage, where a small volume of liquid is injected at the top of a foam and left to evolve.[85,92-94] A especial case of these situations is the gravity-free case, where a liquid flows in a foam in the absence of significant gravitational forces and the motion of the liquid is governed by the capillarity only.[87,95,96]

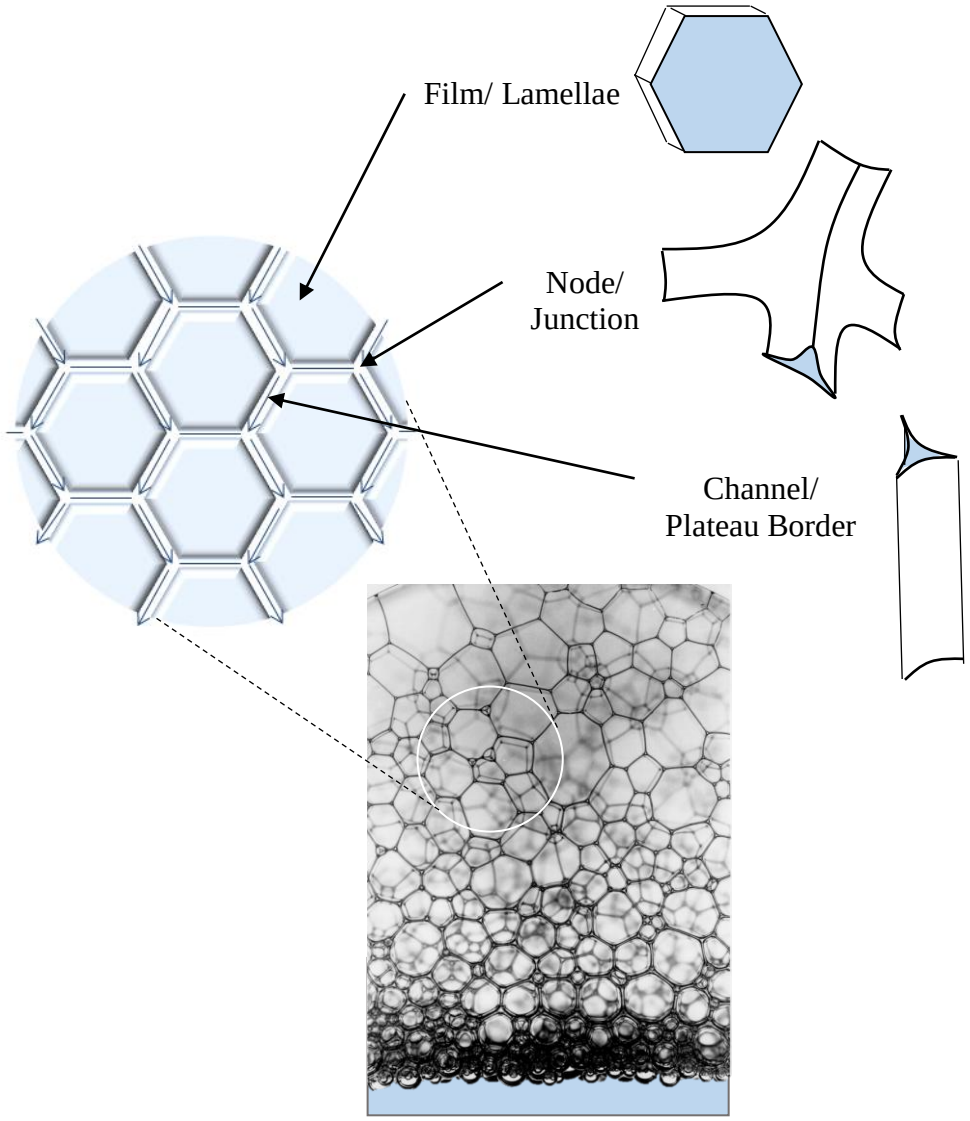

Figure 2.6: Schematic of foam geometry and foam drainage through three distinct interconnected elements, film/lamellae, node/junction, and channel/Plateau border.

The studies on drainage kinetics are of a significant importance for industry. Accordingly, theories of foam drainage have been developed over the last decades[92,97] and a number of techniques and methods such as foam pressure drop technique,[70] Eiffel Tower construction,[98] and Plateau border apparatus experiment[99] have been proposed to control and/or accelerate the rate of liquid drainage. The rate of liquid drainage in these techniques can be adjusted by a controlled reduction of the pressure at the top and/or at the bottom of the foam column, by varying the shape and geometry of the container, and by changing the surface properties of the foaming solution, respectively. Despite a considerable progress in controlling the rate of foam drainage and understanding foam properties, there is still no

straightforward way to create foam with desirable properties suitable for a specific application.

For many applications, particularly in pharmacy and cosmetics, foams are built up and stabilised by polymers. In general polymeric additives make the foaming solution shear thinning non-Newtonian fluids. On the other hand, often the surfaces where foam is applied on are porous (skin, hair, textile materials). The interaction of foam with a porous substrate can affect the kinetics of the release of active substances from foam into the substrate. Accordingly, this interaction should be taken into consideration for finding optimal formulations. However, at the moment not only there is no comprehensive theory of foam drainage of non-Newtonian solutions, but there is also no theory available to describe interaction of foams with porous substrates.

In chapter 6, a theoretical model for free drainage of foams produced from power-law non-Newtonian shear thinning liquids is presented and the predicted results are compared with experimental data for the drainage of foams produced from Aculyn™ 22 and Aculyn™ 33 polymeric solutions, while in Chapter 7, a completely new mathematical model of interaction of foams with porous surfaces is introduced.

Nomenclature 2

A_H	Hamaker constant
c_0	electrolyte concentration
F	Faraday's constant
$F_{surface\ forces}$	excess free energy associated with the action of surface forces
h	film thickness, equilibrium liquid profile, droplet height
h_e	precursor film thickness
K_1	parameters related to the magnitude of the short-range structural forces
K_2	parameters related to the magnitude of the long-range structural forces

L	radius of the droplet base
p	vapor pressure over a curved interface
p_{sat}	saturated vapor pressure over a flat liquid surface
P	non-equilibrium pressure, applied pressure from a droplet to its substrate
P_e	excess (equilibrium) pressure
P_l	pressure inside the liquid
P_v	pressure in the ambient vapor
R	universal gas constant
S_e	excess of the liquid-vapour surface area
t	time
T	temperature
v_m	molar volume the liquid
V_e	excess of the volume
x	coordinate axis
y	coordinate normal to the liquid-air interface

Greek Symbols

γ	liquid-vapour interfacial tension
γ_{sv}	solid-vapour interfacial tension
γ_{sl}	solid-liquid interfacial tension
ε	dielectric constant of water
ε_0	dielectric constant of vacuum
θ_e	equilibrium contact angle
θ_d	dynamic contact angle

λ_1	parameter related to the characteristic length of the short-range structural forces
λ_2	parameter related to the characteristic length of the long-range structural forces
$\boldsymbol{\Pi}$	disjoining/conjoining pressure isotherm
Π_E	electrostatic component of disjoining/conjoining pressure
Π_M	molecular or van der Waals component of disjoining/conjoining pressure
$\boldsymbol{\Pi}_S$	structural component of disjoining/conjoining pressure
σ_s	surface charge density for the solid/liquid interface
φ	dimensionless electric potential
Φ	excess free energy of a droplet

CHAPTER 3

WETTING OF DEFORMABLE SUBSTRATES AND SURFACE FORCES

Overview

In this chapter theoretical findings on wetting of deformable substrate and the effect of surface forces on the equilibrium contact angle and deformation of deformable substrate are presented. The results of investigations are in press in *Colloids and Surfaces A: Physicochemical and Engineering Aspects*, 2016 and reused in this chapter with permission. Initially in this chapter, disjoining pressure action in the vicinity of the apparent three phase contact line is taken into account and it is shown that the disjoining pressure action determines the substrate deformation. Then a simplified linear disjoining pressure isotherm and a simple Winkler's model of substrate deformation are used which allows deducing an analytical solutions for both the liquid profile and substrate deformation. In the next section, the apparent equilibrium contact angle that the droplet makes with the substrate and the profiles of both droplet and deformable substrate are calculated and their dependency on the system parameters is investigated.

3.1 Introduction

Equilibrium of a liquid droplet on a solid substrate is frequently described based on Young's equation.[100] This simplified equation involves the balance of the horizontal forces leaving the vertical force unbalance. The latter is possible in the case of a rigid substrate but should be reconsidered in the case of deformable substrates. It has been shown in[14] that disjoining pressure action in the vicinity of the apparent three phase contact line results in a deformation of a deformable solid substrate.

Note that direct application of Young's equation leads to deformation singularity at the three phase contact line, i.e. the substrate deformation goes to infinity:[101-105] these investigation revealed that all the equilibrium properties (i.e. contact angle, droplet radius, etc.) of the system under consideration rely upon the selected

artificial length parameter which determines a width of zone near the contact line where surface tension is applied. It is shown below that disjoining pressure, which is a real physical phenomenon, determines the deformation of deformable surfaces. The shape of the disjoining pressure isotherm determines the shape and the contact angle of the droplet at equilibrium.[14]

The problem of equilibrium of the droplet on a deformable substrate has recently gained a lot of interest. A number of experimental studies[104,106-111] were recently conducted to investigate deformation of deformable substrates by liquid droplets near the apparent contact line. However, there still exists a gap in theoretically understanding of the problem, because the real physical phenomenon, disjoining pressure action in the vicinity of the three phase contact line, has been mostly ignored: the latter resulted in an artificial singularity at the three phase contact line. Below a mathematical model is presented which incorporates the effect of both capillary and disjoining pressure on the substrate deformation.

3.2 Theory

3.2.1 Disjoining pressure and deformation of deformable substrate

In the case of partial wetting, that is, equilibrium contact angle, $\theta_e > 0$, the shape of the transition zone between the bulk of the liquid droplet and the thin film on a rigid substrate can be expressed via the disjoining pressure isotherm, $\Pi(h)$.[14] The equilibrium excess pressure, P_e, inside the droplet can be expressed according to Kelvin's equation and the equilibrium contact angle of a two dimensional droplet can be expressed using the disjoining pressure isotherm as follows:[14]

$$\cos\theta_{e,2D} = 1 + \frac{\Pi(h_e)h_e}{\gamma} + \frac{1}{\gamma}\int_{h_e}^{\infty}\Pi(h)dh. \tag{3.1}$$

In Eq. (3.1) S-shaped disjoining pressure isotherm, $\Pi(h)$, that is, the case of partial wetting is used. As a first step the transition zone between a two-dimensional droplet on a deformable substrate and a flat film having $\theta_e > 0$ is examined qualitatively following Ref.[112]. The liquid droplet forms a wedge changing to flat equilibrium film of thickness, h_e, far from the droplet (Fig. 3.1).

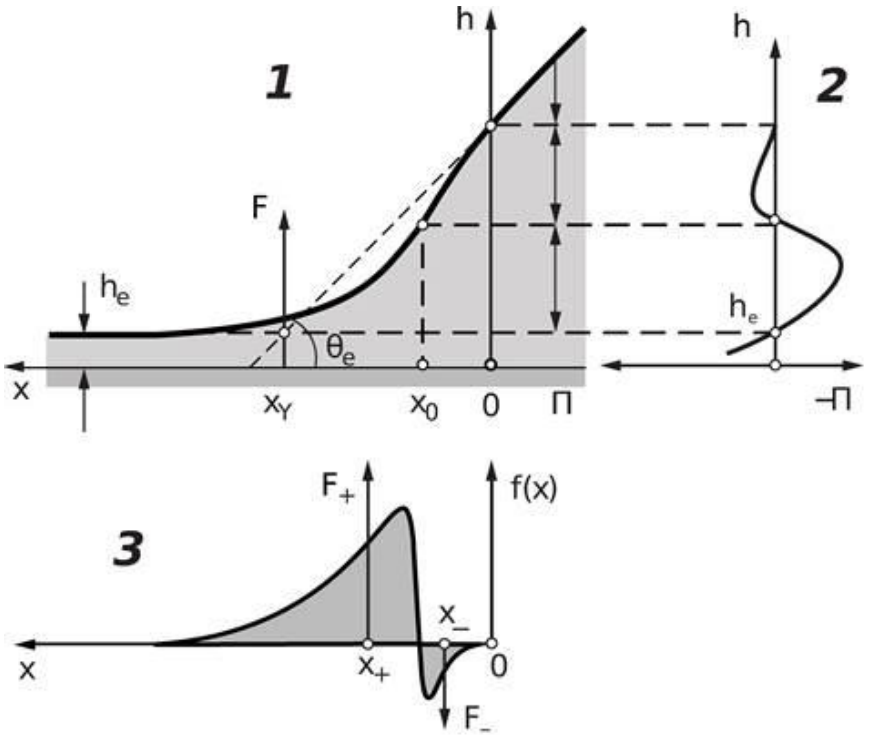

Figure 3.1: 1- Profile of transition zone $h(x)$ between bulk liquid and flat wetting film, 2- S-shaped disjoining pressure isotherm, $\Pi(h)$, and 3- Profile of normal pressures acting on substrate; $x\pm$ are the positions where the vertical forces are exerted. Reproduced with permission from Ref.[113]. Copyright © 2016 Elsevier B.V.

The origin is taken at $x = 0$, which is a point on the profile lying beyond the influence of surface forces (Fig. 3.1). The profile of the transition zone, $h(x)$, can be calculated according to Eq. (3.2), which includes the influence of both capillary and disjoining pressure:[14]

$$\gamma K(x) + \Pi(h) = \frac{\gamma h''}{[1 + (h')^2]^{3/2}} + \Pi(h) = P_e. \tag{3.2}$$

where, $h' = dh/dx$; $h'' = d^2h/dx^2$; and P_e is the excess pressure in the droplet. In the region of the flat equilibrium film, $h'' = 0$ and $\Pi(h_e) = P_e$. In the bulk of the liquid, beyond the influence of the surface forces, $\Pi = 0$ and $P_e = \gamma/R$, where R is the radius of curvature of the droplet. In the case of a planar wedge (Fig. 3.1), $R = \infty$ and $P_e = 0$. Therefore, it can be concluded from Eq. (3.2):

$$\Pi(h) = -\frac{\gamma h''}{[1 + (h')^2]^{\frac{3}{2}}}, \tag{3.3}$$

The resultant force on the substrate is given by the following equation:

$$F = \int_0^\infty \Pi(h)dx. \tag{3.4}$$

Substituting the disjoining pressure isotherm $\Pi(h)$ according to Eq. (3.3) into Eq. (3.4) results in:

$$F = -\gamma \int_0^\infty \left\{ \frac{h''}{[1+(h')^2]^{\frac{3}{2}}} \right\} dx = \gamma \frac{h'(0)}{\sqrt{\left[1+\left(h'(0)\right)^2\right]}} = \frac{\gamma \tan\theta_e}{\sqrt{[1+\tan^2\theta_e]}} \tag{3.5}$$

$$= \gamma \sin\theta_e.$$

Boundary conditions used in the expression above (Eq. (3.5)) are, $h'(\infty) = 0$ and $h'(0) = \tan\theta_e$. This shows that the integration performed over the local values leads to same expression as the vertical component of the surface tension from the Young's equation. In contrast to Young's, the force is not exerted at a specific point, but it is distributed over the region where disjoining pressure acts, i.e. transition zone. Based on this conclusion a mathematical model is derived in the next section.

3.2.2 Mathematical model

In this section a mathematical model is deduced for a liquid droplet on a deformable substrate. A simple Winkler's model for the deformable solid deformation is used below. According to the Winkler's model there is a linear relationship between the local deformation and the applied local stress.[113,114]

Fig. 3.2 shows a schematic diagram of the liquid droplet on a deformable substrate. Deformation in the deformable substrate is local and is directly proportional to the applied pressure, P. According to the Winkler's model:

$$h_s = -KP, \tag{3.6}$$

where, K is the elasticity coefficient, h_s is the local deformation of the substrate due to the presence of the applied pressure, P, from the droplet above, see Fig. 3.2.

Let P_{air} be the pressure in the ambient air. Under the action of the pressure from the ambient air the solid deformation is:

$$h_{se} = -KP_{air}. \tag{3.7}$$

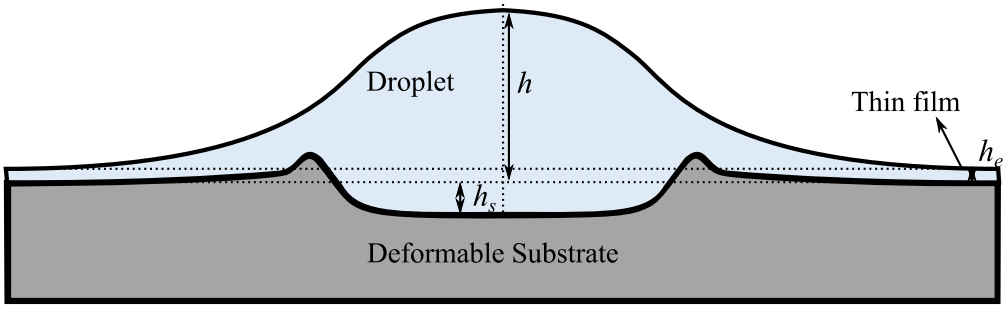

Figure 3.2: Schematic diagram of the liquid droplet on a deformable substrate. Reproduced with permission from Ref.[113]. Copyright © 2016 Elsevier B.V.

The deformed solid substrate is covered by equilibrium liquid thin film, which is calculated according to combination of well-known Kelvin's equation and disjoining pressure isotherm:[14]

$$\Pi(h_e) = P_e = \frac{RT}{v_m} \ln \frac{p_{sat}}{p}, \tag{3.8}$$

where, v_m is the molar volume of the liquid, T is the temperature in K, R is the gas constant, vapour pressure, p, which is higher than the saturated pressure p_{sat}. Reminder, a droplet can be at the equilibrium with oversaturated vapour only.

The excess free energy of the equilibrium thin film on the deformed solid per unit area is given by,

$$\frac{F_{e,film}}{S_{film}} = \gamma + \gamma_s + P_e h_e + \frac{h_{se}^2}{2K} + \int_{h_e}^{\infty} \Pi(h) dh, \tag{3.9}$$

where, $P_e = P_{air} - P_{liquid}$, γ and γ_s are liquid-vapour and solid-liquid interfacial tensions. This free energy should be subtracted from the free energy of the droplet on the deformable substrate; otherwise the excess free energy of the droplet is infinite. Hence, the excess free energy of the droplet on a deformable solid substrate is as follows (Fig. 3.2):

$$F - F_{e,film} = \gamma \Delta S + \gamma_s \Delta S_s + P_e \Delta V + F_{surface\ forces} + F_{deformation}, \tag{3.10}$$

where Δ means "as compared with a flat equilibrium film".

Eq. (3.10) can be rewritten as:

$$F - F_{e,film} = 2\pi \int_0^{\infty} f(h, h', h_s, h'_s) dr, \tag{3.11}$$

where

$$f(h,h',h_s,h'_s) = r\left[\begin{array}{c}\gamma\sqrt{1+h'^2(r)}-\gamma+\gamma_s\sqrt{1+h'^2_s(r)}-\gamma_s+\\ P_e(h-h_s)-P_e h_e+\frac{h_s^2}{2K}-\frac{h_{se}^2}{2K}\\ +\int_{h-h_s}^{\infty}\Pi(h)dh-\int_{h_e}^{\infty}\Pi(h)dh\end{array}\right]. \quad (3.12)$$

In above equations r is the length along radial direction. The expression under the integral in Eq. (3.11) tends to zero as r tends to infinity.

Under equilibrium conditions the excess free energy, Eq. (3.11), should reach minimum value. To satisfy this condition the first variation of excess free energy, Eq. (3.11), should be zero, which results in two Euler equations for the droplet and deformable substrate profiles:

$$\frac{d}{dr}\left(\frac{\partial f}{\partial h'}\right)-\frac{\partial f}{\partial h}=0, \quad (3.13)$$

$$\frac{d}{dr}\left(\frac{\partial f}{\partial h'_s}\right)-\frac{\partial f}{\partial h_s}=0. \quad (3.14)$$

Substitution of the expression for f from Eq. (3.12) into Eqs. (3.13) and (3.14) results in the following system of second order differential equations:

$$\frac{\gamma}{r}\frac{d}{dr}\frac{rh'}{(1+h'^2)^{1/2}}+\Pi(h-h_s)=P_e, \quad (3.15)$$

$$\frac{\gamma_s}{r}\frac{d}{dr}\frac{rh'_s}{(1+h'^2_s)^{1/2}}-\Pi(h-h_s)-\frac{h_s}{K}=-P_e. \quad (3.16)$$

Eqs. (3.15) and (3.16) form a system of two differential equations for two unknown profiles: the liquid droplet, $h(r)$, and deformed solid substrate, $h_s(r)$.

In the case of a low slope approximation, $h'^2 \ll 1$ the profile of the droplet $h(r)$ and profile of the substrate, $h_s(r)$, satisfy the following set of second order ordinary differential equations:

$$\gamma\left(h''+\frac{h'}{r}\right)+\Pi(h-h_s)=P_e, \quad (3.17)$$

$$\gamma_s\left(h''_s+\frac{h'_s}{r}\right)-\Pi(h-h_s)-\frac{h_s}{K}=-P_e. \quad (3.18)$$

Eq. (3.17) is different from the usual capillary equation for the droplet on a rigid substrate, because now the disjoining pressure term depends on the profile of the deformable substrate, $h_s(r)$, which is determined according to Eq. (3.18). Eqs. (3.17) and (3.18) are coupled and can be solved numerically only; however, below

the problem is simplified even further to obtain an analytical solution. For this purpose a very simple disjoining pressure isotherm (linear function of h (Fig. (3.3)) is adopted:

$$\Pi(h) = \begin{cases} P_1 - ah & at\ \ h \le t_1 \\ 0 & at\ \ h > t_1 \end{cases}. \tag{3.19}$$

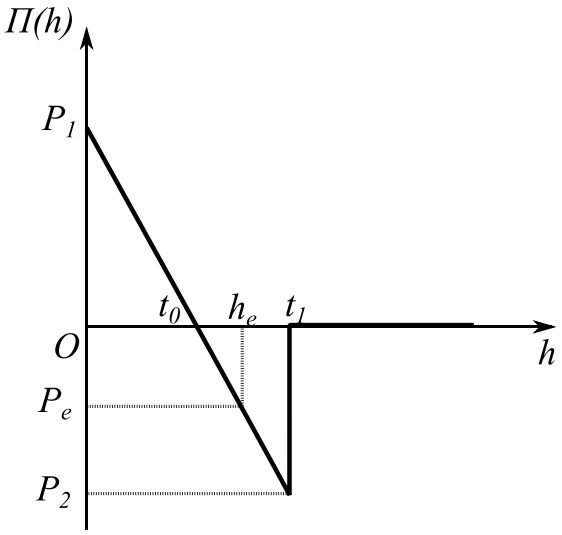

Figure 3.3: Simplified disjoining pressure isotherm adopted for calculations. Reproduced with permission from Ref.[113]. Copyright © 2016 Elsevier B.V.

where P_1 and t_0 are defined in Fig. 3.3, t_1 is the range of surface forces action. The corresponding radial length from the origin to the point of height t_1 is L_1, see Fig. 3.4. The slope a of the $\Pi(h)$ dependency is given by:

$$a = \frac{P_1 - P_e}{h_e}. \tag{3.20}$$

The selected linear dependency of the disjoining pressure isotherm $\Pi(h)$ on h according to Eq. (3.19) still captures the essential properties of the disjoining pressure isotherm in spite of considerable simplification: (i) it satisfies the stability condition, $\Pi'(h) < 0$ when $h < t_1$; (ii) the influence of surface forces is short range and radius of its action is defined by t_1; (iii) it corresponds to the partial wetting case at the proper choice of the disjoining pressure parameters (see below). Although similar type of isotherm has been used in past to determine the shape of the transition zone, it has not been used for droplets on deformable substrates.[115] In the future a disjoining pressure which corresponds to real systems will be used.

3.2.2.1 Three dimensional axisymmetric droplets on a non-deformable substrate

Earlier only two dimensional droplets on non-deformable substrates were considered and the expression for the equilibrium contact angle, Eq. (3.1), was deduced.[14] In this part an expression for a contact angle of axisymmetric three dimensional droplets is deduced and compared with the corresponding contact angle for two-dimensional droplets according to Eq. (3.1).

Fig 3.4 shows a schematic diagram of a three-dimensional droplet on a non-deformable solid substrate, where L_1 is the length from the origin to the point where the influence of the surface forces comes into play, L is the effective radius of the droplet base, $\theta_{e,nd}$ is the equilibrium contact angle the droplet makes with the solid substrate, R is the radius of the droplet curvature, where $R = -\frac{2\gamma}{P_e}$.

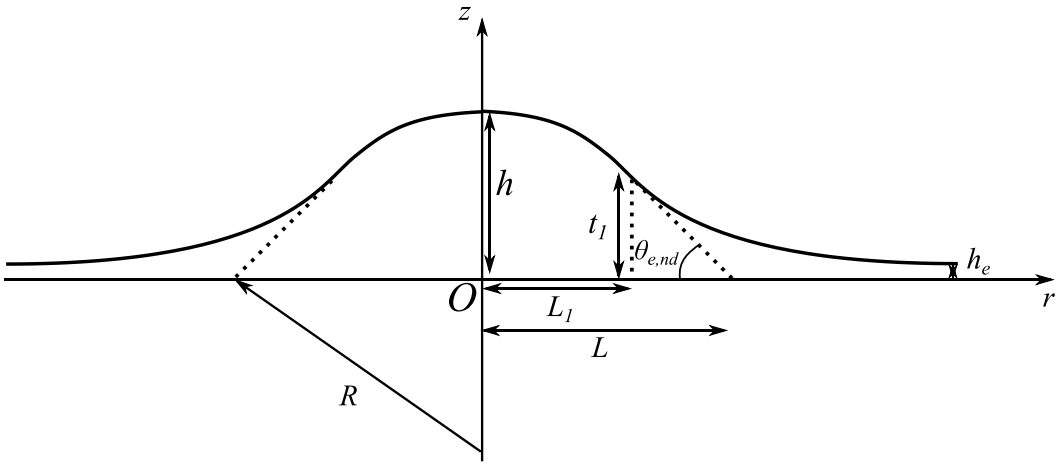

Figure 3.4: Schematic diagram of a 3D droplet on a non-deformable solid substrate. Reproduced with permission from Ref.[113]. Copyright © 2016 Elsevier B.V.

For a solid non-deformable substrate Eqs. (3.17) and (3.18) reduces to:

$$\gamma\left(h'' + \frac{h'}{r}\right) + \Pi(h) = P_e. \tag{3.21}$$

For the bulk of the liquid droplet, i.e. the spherical region in which $h > t_1$, $\Pi(h) = 0$. Hence, in this region Eq. (3.21) transforms into:

$$\gamma\left(h'' + \frac{h'}{r}\right) = P_e. \tag{3.22}$$

Solution of this equation is:

$$h(r) = Ar^2 + B, \tag{3.23}$$

where integration constants, A and B, can be determined from boundary conditions at $r = 0$ and $r = L$ and this solution is marked by a subscript *out*:

$$h_{out}(r) = -\frac{r^2}{2R} + \frac{R\sin^2\theta_{e,nd}}{2} \text{ or } h_{out}(r) = \frac{-r^2 + L^2}{2R}. \tag{3.24}$$

For the transition region in the case of non-deformable solid substrate Eq. (3.21) along with the disjoining pressure isotherm given by Eq. (3.19) results in:

$$h'' + \frac{h'}{r} - \frac{ah}{\gamma} = \frac{P_e - P_1}{\gamma}. \tag{3.25}$$

Solution of Eq. (3.25) marked by a subscript *in* is as follows:

$$h_{in} = h_e + C_{1,nd}K_0(r\lambda), \tag{3.26}$$

where, $\lambda = \sqrt{\frac{a}{\gamma}}$, K_0 is the modified Bessel function of second kind of zero order, $C_{1.nd}$ is an integration constant. Solutions (3.24) and (3.26) should satisfy the boundary conditions: $h_{out}(L_1) = h_{in}(L_1) = t_1$; $h'_{out}(L_1) = h'_{in}(L_1)$, which gives three equations for determination of the three unknown coefficients $C_{1,nd}, \theta_{e,nd}$ and L_1. Solution results in,

$$C_{1,nd}K_0(L_1\lambda) = \frac{L_1}{R\lambda}, \tag{3.27}$$

$$\theta_{e,nd} = \sqrt{\frac{2}{R}\left(h_e + \frac{L_1}{R\lambda} + \frac{L_1^2}{2R}\right)}, \tag{3.28}$$

$$L_1 = R\lambda(t_1 - h_e). \tag{3.29}$$

The latter allows determining the effective radius of the droplet, L:

$$L = \sqrt{L_1^2 + 2Rt_1}. \tag{3.30}$$

Introducing: $P_2 = a(t_0 - t_1)$, Eq. (3.28) can be rewritten as,

$$\theta_{e,nd} = \sqrt{\frac{1}{\gamma a}[P_e^2 - P_1P_e - P_2P_e + P_2^2]}. \tag{3.31}$$

The equilibrium contact angle was previously determined according to Eq. (3.1). According to the simplified isotherm (Fig. 3.3) this contact angle can be calculated as:

$$\theta_{e,2D} = \sqrt{2\left\{-\frac{P_e h_e}{\gamma} - \frac{a}{\gamma}\left[t_0(t_1 - h_e) - \frac{1}{2}(t_1^2 - h_e^2)\right]\right\}}. \quad (3.32)$$

3.2.2.2 Three dimensional droplets on a deformable substrate

Fig. 3.5 shows a schematic diagram of a droplet on a deformable solid substrate. The same as before the simplified linear disjoining pressure isotherm according to Eq. (3.19) is used. In Fig. 3.5, $\theta_{e,d}$ is the apparent macroscopic equilibrium contact angle of the droplet with the deformable substrate.

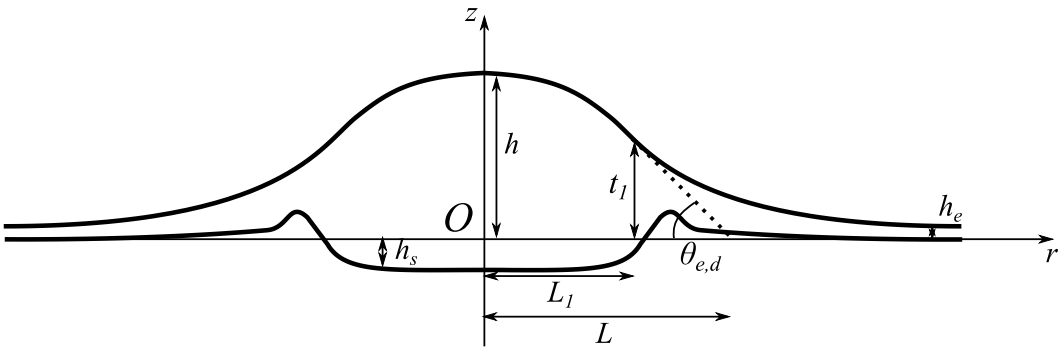

Figure 3.5: Schematic diagram of droplet on a deformable substrate. Reproduced with permission from Ref.[113]. Copyright © 2016 Elsevier B.V.

For the bulk of the liquid droplet, i.e. the spherical region ($0 < r < L_1$), $h - h_s > t_1$, Eq. (3.18) becomes:

$$-\gamma_s\left(h_s'' + \frac{h_s'}{r}\right) + \frac{h_s}{K} = P_e. \quad (3.33)$$

Solving the above equation results in:

$$h_{s,out} = KP_e + C_{3,dg} I_0(r\beta), \quad (3.34)$$

where I_0 is the modified Bessel function of first kind of zero order, β is equal to $\frac{1}{\sqrt{K\gamma_s}}$ and $C_{3.dg}$ is an integration constant. Bulk droplet solution remains same as Eq. (3.24). Note that for $r = 0$, $h_{s,out} = KP_e + C_{3,dg}$.

For the transition region $(r > L_1)$, the droplet profile and the deformed substrate profile governed by Eqs. (3.17) and (3.18) can be respectively simplified to,

$$h'' + \frac{h'}{r} - \frac{a(h - h_s)}{\gamma} = \frac{P_e - P_1}{\gamma}, \tag{3.35}$$

and

$$h_s'' + \frac{h_s'}{r} - h_s\left(\frac{aK + 1}{\gamma_s K}\right) + \frac{ah}{\gamma_s} = -\left(\frac{P_e - P_1}{\gamma_s}\right). \tag{3.36}$$

The system of two linear differential equations of the second order (3.35) and (3.36) should be solved. In order to deduce the solution of the system of Eqs. (3.35) and (3.36) an unknown solution is introduced in the following form:

$$y(r) = h(r) + \alpha h_s(r), \tag{3.37}$$

where $y(r)$ is a new unknown function which is a linear combination of both profiles, h_s, the deformed substrate, and h, the droplet. In Eq. (3.37), α is a constant to be determined. The first and second derivatives of y are:

$$\begin{aligned} y' &= h' + \alpha h_s', \\ y'' &= h'' + \alpha h_s''. \end{aligned} \tag{3.38}$$

Let us multiply Eq. (3.36) with α and add it to Eq. (3.35) which results in:

$$\begin{aligned} h'' + \alpha h_s'' + \frac{1}{r}(h' + \alpha h_s') - \frac{ah}{\gamma} + \frac{a\alpha h}{\gamma_s} + \frac{ah_s}{\gamma} - \frac{\alpha h_s}{\gamma_s}\left(\frac{aK + 1}{K}\right) \\ = \frac{P_e - P_1}{\gamma} - \alpha\left(\frac{P_e - P_1}{\gamma_s}\right). \end{aligned} \tag{3.39}$$

Using values of y, y', y'' and substituting them into Eq. (3.39) results in:

$$\begin{aligned} y'' + \frac{y'}{r} - a\left(\frac{1}{\gamma} - \frac{\alpha}{\gamma_s}\right)y + h_s\left[a\alpha\left(\frac{1}{\gamma} - \frac{\alpha}{\gamma_s}\right) + \frac{a}{\gamma} - \frac{\alpha}{\gamma_s}\left(\frac{aK + 1}{K}\right)\right] \\ = (P_e - P_1)\left(\frac{1}{\gamma} - \frac{\alpha}{\gamma_s}\right). \end{aligned} \tag{3.40}$$

To calculate function $y(r)$ from Eq. (3.40) let us suppose that the constant in square bracket is equal to zero, i.e.:

$$a\alpha\left(\frac{1}{\gamma} - \frac{\alpha}{\gamma_s}\right) + \frac{a}{\gamma} - \frac{\alpha}{\gamma_s}\left(\frac{aK + 1}{K}\right) = 0, \tag{3.41}$$

which is a quadratic equation in α. α can be determined from the above equation and has two roots:

$$\alpha_{1,2} = \frac{-\left(-\frac{\gamma_s}{\gamma} + \left(\frac{aK + 1}{aK}\right)\right) \pm \sqrt{\left(-\frac{\gamma_s}{\gamma} + \left(\frac{aK + 1}{aK}\right)\right)^2 + \frac{4\gamma_s}{\gamma}}}{2}, \tag{3.42}$$

where $\alpha_1 > 0$ and $\alpha_2 < 0$. The latter results in two different functions $y(r)$ and from Eq. (3.40) these functions must satisfy,

$$y'' + \frac{y'}{r} - a\left(\frac{1}{\gamma} - \frac{\alpha}{\gamma_s}\right) y = (P_e - P_1)\left(\frac{1}{\gamma} - \frac{\alpha}{\gamma_s}\right). \tag{3.43}$$

Therefore, the two unknown functions y become:

$$y_i = h_e + C_{i,dg} K_0\left(r\sqrt{a\left(\frac{1}{\gamma} - \frac{\alpha_i}{\gamma_s}\right)}\right), \tag{3.44}$$

where $i = 1, 2$. Let $\phi_i = \sqrt{a\left(\frac{1}{\gamma} - \frac{\alpha_i}{\gamma_s}\right)}$. Then the above equation can be written as:

$$\begin{aligned} y_1 &= h_e + C_{1,dg} K_0(r\phi_1), \\ y_2 &= h_e + C_{2,dg} K_0(r\phi_2). \end{aligned} \tag{3.45}$$

where $y_1 = h + \alpha_1 h_s$ and $y_2 = h + \alpha_2 h_s$. Evaluating h and h_s from solutions above results in:

$$h_{s,in} = \frac{C_{1,dg} K_0(r\phi_1) - C_{2,dg} K_0(r\phi_2)}{\alpha_1 - \alpha_2}, \tag{3.46}$$

and

$$h_{in} = \frac{\left[h_e(\alpha_1 - \alpha_2) - \alpha_2 C_{1,dg} K_0(r\phi_1) + \alpha_1 C_{2,dg} K_0(r\phi_2)\right]}{\alpha_1 - \alpha_2}. \tag{3.47}$$

where K_0 is the modified Bessel function of second kind of zero order, $C_{1.dg}$and $C_{2.dg}$ are integration constants. Solutions represented by Eqs. (3.24), (3.34), (3.46), and (3.47) must satisfy the following boundary conditions: $h_{out}(L_1) = h_{in}(L_1)$; $h'_{out}(L_1) = h'_{in}(L_1)$; $h_{s,out}(L_1) = h_{s,in}(L_1)$; $h'_{s,out}(L_1) = h'_{s,in}(L_1)$; and $h(L_1) - h_s(L_1) = t_1$ which gives five equations for determination of the five unknown coefficients $C_{1,dg}, C_{2,dg}, C_{3,dg}, L_1$ and L. In all case under consideration below the following inequalities are satisfies: $L_1\phi_1 > 5$, $L_1\phi_2 > 5$, $\frac{L_1}{\sqrt{\gamma_s K}} > 5$. Hence, the following approximate relations can be used:

$$\begin{aligned} &\frac{K_0(L_1\phi_1)}{K_1(L_1\phi_1)} \sim 1 \\ &\frac{K_0(L_1\phi_2)}{K_1(L_1\phi_2)} \sim 1 \\ &\frac{I_0(L_1\beta)}{I_1(L_1\beta)} \sim 1 \end{aligned} \tag{3.48}$$

Using approximations in Eq. (3.48) and the above mentioned boundary conditions, Eqs. (3.24), (3.34), (3.46), and (3.47), are solved and the unknown coefficients are calculated. Examining the Bessel functions in Eqs. (3.34), (3.46), and (3.47) it can be inferred that $\frac{1}{\phi_1}$, $\frac{1}{\phi_2}$ and $\frac{1}{\beta}$ are all essentially length scales. ϕ_1 and ϕ_2 are present in Eqs. (3.46) and (3.47) and they influence the transition region. Note that ϕ_2 is always greater than ϕ_1 substituting the real values of a, γ, γ_s and α_i (see below) and therefore, $\frac{1}{\phi_2}$ length scale will have lesser effect in comparison to $\frac{1}{\phi_1}$ length scale. From Eq. (3.34) it is evident that $\frac{1}{\beta}$ scale influences the bulk of the droplet. These length scales play an important role when physical parameters are varied and will be discussed in more details in the next section.

3.3 Results and discussion

3.3.1 Non-deformable substrate: Effect of variation of P_e on $\theta_{e,nd}$

Equilibrium contact angles $\theta_{e,nd}$ and $\theta_{e,2D}$ are functions of the excess pressure, P_e, according to Eqs. (3.28) and (3.32). In this section this dependency is presented. The parameters of the disjoining pressure isotherm are presented in Table 3.1. $|P_e|$ is varied from 0 to $|P_2|$. Fig. 3.6 shows the behaviour of equilibrium contact angle when the excess pressure is varied. Fig. 3.6(a) demonstrates the variation at $t_0 = 7 \times 10^{-7}$cm and Fig. 3.6(b) shows variation at $t_0 = 2 \times 10^{-6}$cm. In both cases, two-dimensional equilibrium contact angle $\theta_{e,2D}$, calculated according to Eq. (3.32), is higher than three-dimensional equilibrium contact angle calculated according to Eq. (3.31). It was shown earlier[14] $\theta_{e,2D}$ can only increase with the decrease in P_e, which is in agreement with both Figs. 3.6(a) and 3.6(b). However, it turns out that the dependency of the contact angle in the three dimensional case, $\theta_{e,nd}$, differs substantially from the two dimensional case (always higher) and it can go via minimum as a function of P_e (Figs. 3.6(a)). If the value of t_0 is increased and brought closer to t_1 then $\theta_{e,nd}$ is an increasing function of P_e with no minimum.

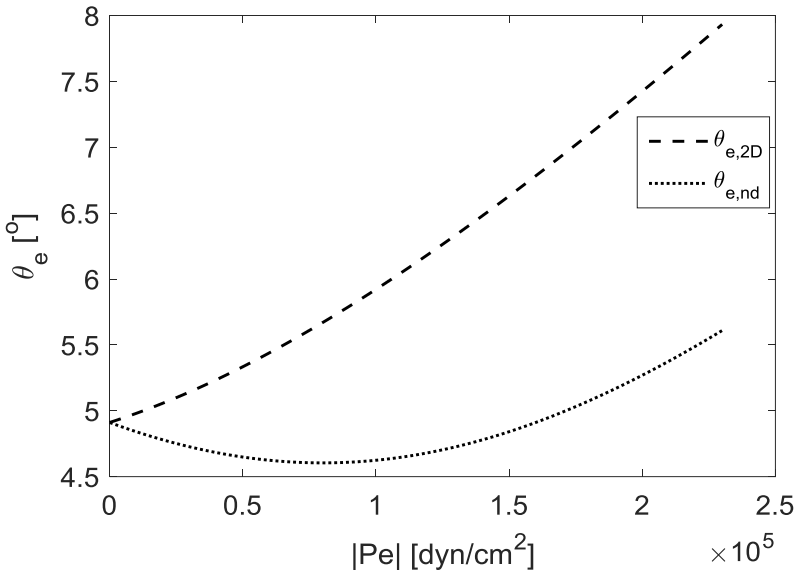

a) $t_0 = 7 \times 10^{-7}$ cm

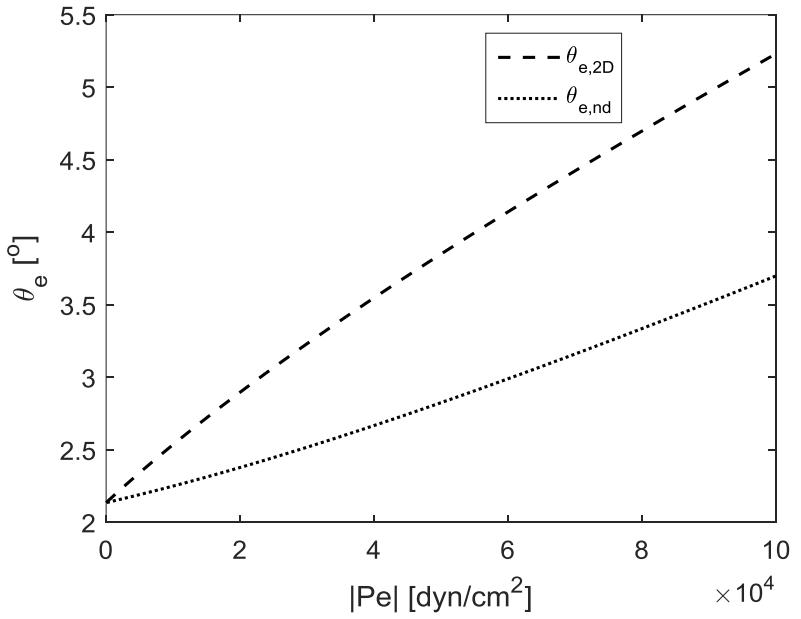

b) $t_0 = 2 \times 10^{-6}$ cm

Figure 3.6: Non-deformable substrate: Effect of variation of excess pressure, P_e on two-dimensional, $\theta_{e,2D}$, and three-dimensional, $\theta_{e,nd}$, equilibrium contact angles. Reproduced with permission from Ref.[113]. Copyright © 2016 Elsevier B.V.

Table 3.1: Parameters of the disjoining pressure isotherm for non-deformable substrate case. Reproduced with permission from Ref.[113]. Copyright © 2016 Elsevier B.V.

Physical Property	Value
γ	72 dyn/cm
t_1	3×10^{-6}cm
a	1×10^{11} dyn/cm^3
$\lvert P_e \rvert$	$0 - \lvert P_2 \rvert$ dyn/cm^2

3.3.2 Deformable substrate

In the vicinity of the three phase contact line disjoining pressure comes into play. Therefore, substrate deformation near the contact line depends largely upon the parameters of the disjoining pressure isotherm. In this section the effect of variation of P_e, a, K and γ_s on substrate deformation and its subsequent effect on the droplet profile is discussed. Fig 3.7 schematically shows different lengths in the region of deformation: L_1 is the length from the axis of symmetry to the point C, where surface forces start to act in the radial direction. $h_{s,max}$ is the maximum height of deformation and $h_{s,min}$ is the minimum height of deformation. Two points are generated on the deformed substrate around point *C*, one in the spherical region, A, and the other in transition region, B, where the slope, $\frac{dh_s}{dr}$, is very small and it drops below 1×10^{-4}. Note that h_s approaches to $KP_e + C_{3,dg}$ as r approaches to zero, see Eq. (3.34). On the other hand h_s approaches to zero as r tends to infinity, see Eq. (3.46). Therefore, $h_s(r = P_1) \sim KP_e + C_{3,dg}$ and $h_s(r = B) \sim 0$ due to the very small slope. Distance between C and A is denoted as Δ_1 (i.e. region of influence of disjoining pressure in the bulk of the droplet) and distance between C and B is denoted by Δ_2 (i.e. region of influence of disjoining pressure in the transition region). It will be shown below that the disjoining pressure effects are transferred from the transition region to the bulk of the droplet and it affects the deformation of the substrate between A and C. Therefore, $\Delta_1 + \Delta_2$ is defined as the total region of influence of disjoining pressure on the deformable substrate. Note that length scales, $\frac{1}{\phi_1}$, $\frac{1}{\phi_2}$, and $\frac{1}{\beta}$, introduced in Section 3.2.2.2 are valid for the relevant regions of the

influence of disjoining pressure, i.e. $\frac{1}{\phi_1}$ and $\frac{1}{\phi_2}$ are applicable to Δ_2 and $\frac{1}{\beta}$ is applicable to Δ_1.

Table 3.2 shows the parameters of the disjoining pressure isotherm used in the case of deformable substrate unless stated otherwise. The profile of the droplet and the subsequent changes in the deformable substrate are plotted (see Fig. 3A.1 in Appendix 3.A) using equations deduced in Sections 3.2.2.1 and 3.2.2.2. It shows that for non-deformable substrate case the height of the droplet at $r = 0$ is greater than the deformable case and it also indicates that for deformable substrate the apparent equilibrium contact angle is lower than in the case of non-deformable substrate. The deformable substrate behaves in the same manner as predicted in Fig. 3.5.

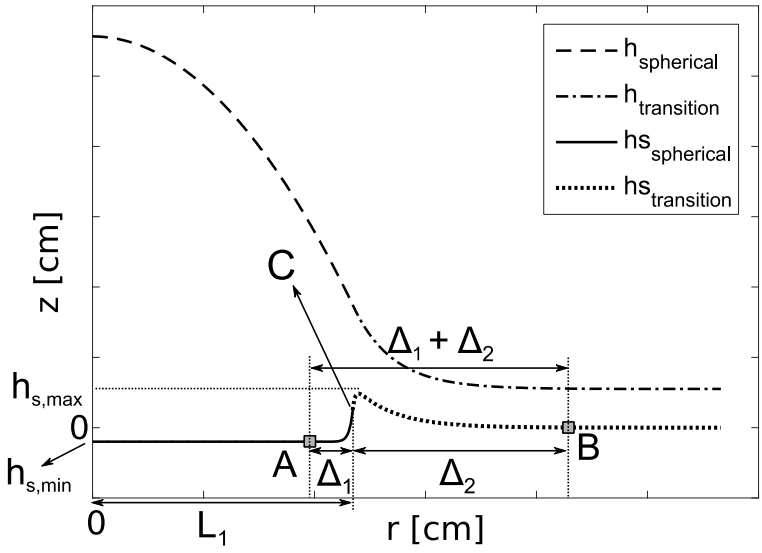

Figure 3.7: Lengths affected by variation of parameters, P_e, a, K and γ_s for a droplet on a deformable substrate. Reproduced with permission from Ref.[113]. Copyright © 2016 Elsevier B.V.

Table 3.2: Properties of the disjoining pressure isotherm for deformable substrate case. Reproduced with permission from Ref.[113]. Copyright © 2016 Elsevier B.V.

Physical Property	Value
γ	72 dyn/cm
t_1	3×10^{-6}cm
t_0	7×10^{-7} cm
a	1×10^{11} dyn/cm^3
K	1×10^{-11} cm^3/dyn
P_e	-1×10^{5} dyn/cm^2
γ_s	1 dyn/cm

3.3.2.1 Effect of variation of excess pressure, P_e

Excess pressure is varied according to $0 \leq |P_e| \leq |P_2|$. In order to compare the results of the apparent equilibrium contact angle on deformable substrate with the one on non-deformable substrate, the value of K is decreased gradually from 1×10^{-11} to 1×10^{-13} cm^3/dyn. All other physical parameters of the disjoining pressure isotherm are kept constant as shown in Table 3.2 except t_0 which is equivalent to 7×10^{-7}cm for the results presented in Fig. 3A.2(a) (Appendix 3.A) and is equivalent to 2×10^{-6}cm for the results in Fig. 3A.2(b) (Appendix 3.A). Dependency of $\theta_{e,d}$ in Fig. 3A.2(a) (Appendix 3.A) has a minimum and it becomes an increasing function as t_0 is increased and brought closer to t_1 (see Fig. 3A.2(b) in Appendix 3.A). Fig. 3A.2 shows that $\theta_{e,d}$ is less than $\theta_{e,nd}$ for all values of $K > 0$. According to Eq. (3.20) the equilibrium flat film thickness h_e increases as the excess pressure, P_e decreases. In its turn increasing the equilibrium film thickness causes $h_{s,max}$ to decrease and the $h_{s,min}$ of substrate to decrease. $h_{s,max}$ and $h_{s,min}$ both have a linear dependence on P_e as shown in Fig. 3.8. Fig. 3.9 shows the variation of the total region of influence of disjoining pressure with the variation of excess pressure (as P_e is reduced, i.e. becomes more negative). $\Delta_1 + \Delta_2$ decreases as P_e is reduced (This is also supported by Fig. 3.11).

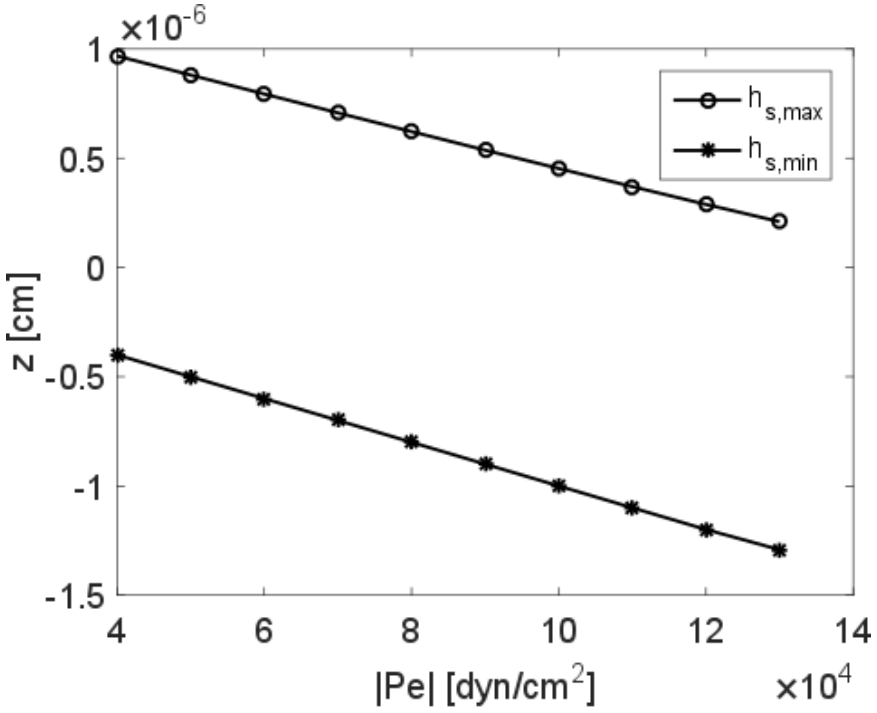

Figure 3.8: Effect of variation of P_e: Maximum and minimum height of substrate deformation as a function of excess pressure ($40000 \leq |P_e| \leq 130000$ dyn/cm^2). Reproduced with permission from Ref.[113]. Copyright © 2016 Elsevier B.V.

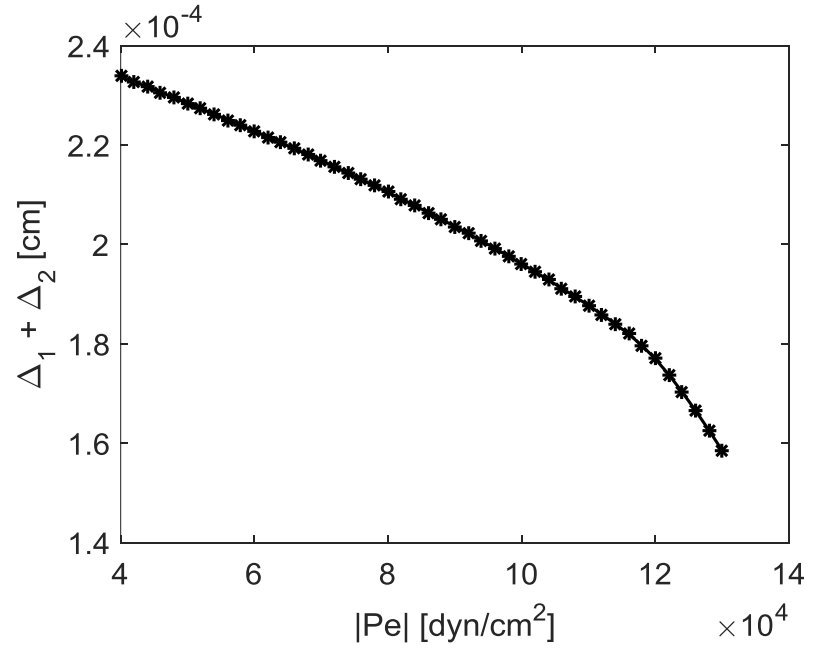

Figure 3.9: Effect of variation of P_e on the region of influence of disjoining pressure. Reproduced with permission from Ref.[113]. Copyright © 2016 Elsevier B.V.

Fig. 3.10 presents the variation of the ratios of $\Delta_2/\left(\frac{1}{\phi_1}+\frac{1}{\phi_2}\right)$, $\Delta_2/\left(\frac{1}{\phi_1}\right)$, $\Delta_2/\left(\frac{1}{\phi_2}\right)$, and $\Delta_1/\left(\frac{1}{\beta}\right)$ (region of influence of the disjoining pressure in the bulk of the droplet and the transition region to the relevant length scales) as a function of P_e. It is clear from the plots that $\Delta_2/\left(\frac{1}{\phi_1}+\frac{1}{\phi_2}\right)$, $\Delta_2/\left(\frac{1}{\phi_1}\right)$, and $\Delta_2/\left(\frac{1}{\phi_2}\right)$ are all decreasing with decrease in P_e. Length scale $\frac{1}{\phi_2}$ is smaller than $\frac{1}{\phi_1}$, that is the reason its ratio, $\Delta_2/\left(\frac{1}{\phi_2}\right)$, is higher than that of $\frac{1}{\phi_1}$, $\Delta_2/\left(\frac{1}{\phi_1}\right)$ (compare Fig. 3.10(b) and Fig. 3.10(c)). Because Δ_2 is influenced by both $\frac{1}{\phi_1}$ and $\frac{1}{\phi_2}$ length scales, therefore sum of these length scales is used later in the discussion. The plot for $\Delta_1/\left(\frac{1}{\beta}\right)$ illustrates that the ratio first increases to a maximum value and then decreases. Fig. 3.11 shows the profiles of the droplet and substrate with variation in P_e. It is clear that an increase in P_e will cause h_e to decrease, which subsequently affects the height and span of the droplet to increase. Therefore causing the extent of the deformation in the radial direction to increase, but generates a decrease in the depth to which the substrate gets deformed.

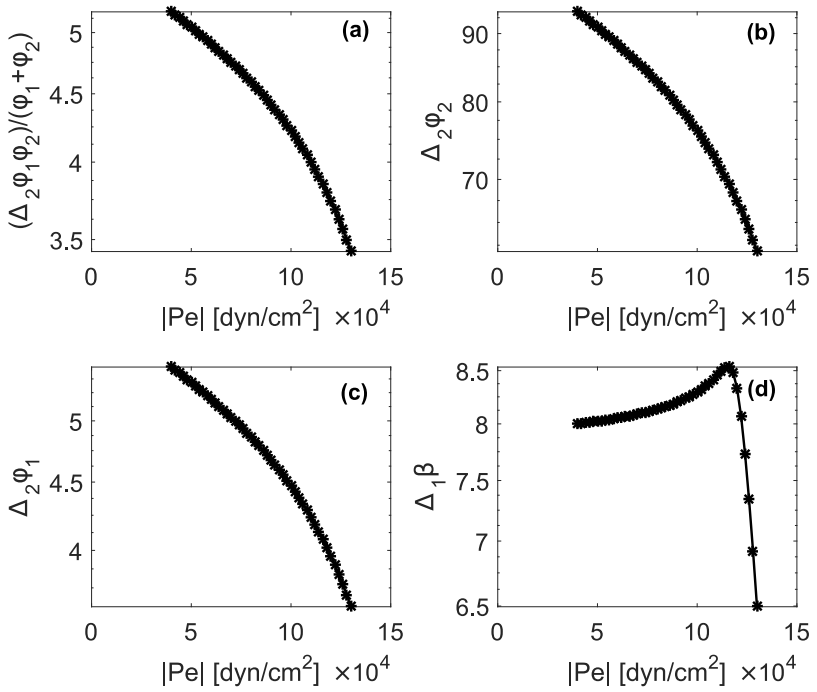

Figure 3.10: Ratio of regions of influence of disjoining pressure to relevant scale plotted against P_e. Reproduced with permission from Ref.[113]. Copyright © 2016 Elsevier B.V.

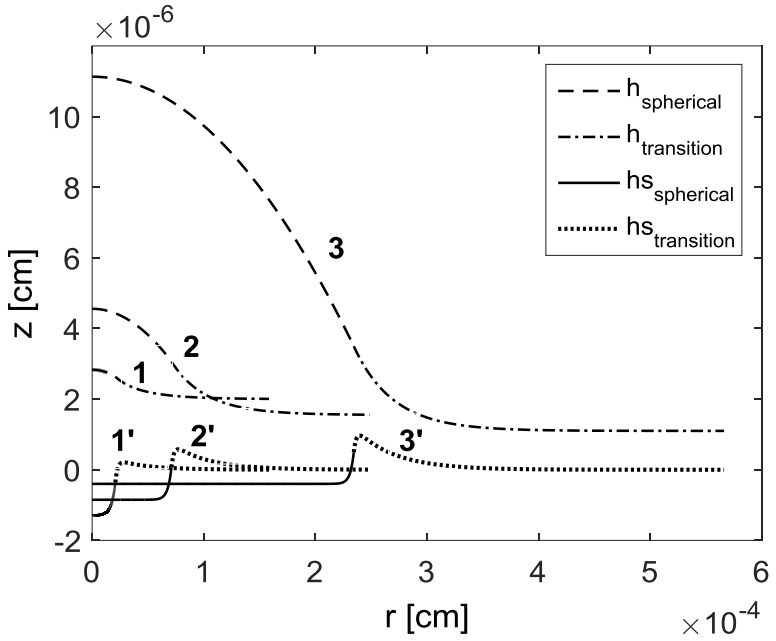

Figure 3.11: Effect of variation of P_e: Profiles of the droplet and substrate deformation, which are under consideration: $1, 1' - |P_e| = 130000$ dyn/cm^2, $2, 2' - |P_e| = 85000$ dyn/cm^2, $3, 3' - |P_e| = 40000$ dyn/cm^2. Reproduced with permission from Ref.[113]. Copyright © 2016 Elsevier B.V.

3.3.2.2 Effect of variation of slope of the disjoining pressure isotherm a

The value of a is increased in the following range $1 \times 10^{11} \leq a \leq 1 \times 10^{12}$ dyn/cm^3 to see the effects on depth of deformation and shape of the droplet. The equilibrium contact angle for deformable substrates increases as the slope increases (see Fig. 3A.3 in Appendix 3.A). Fig. 3A.4 (provided in in Appendix 3.A) shows the variation of the substrate deformation as the slope is increased. Increasing a causes $h_{s,max}$ to increase, but $h_{s,min}$ remains constant. Fig. 3.12 shows the profile of the droplet and the change in deformation profile as a is varied. It is in agreement with the results discussed in the previous plots, i.e. $\theta_{e,d}$ increases, $h_{s,max}$ increases and $h_{s,min}$remains constant with an increase in a as shown in Fig. 3.12. The total region of influence of disjoining pressure increases with an increase in the slope of the disjoining pressure isotherm (see Fig. 3A.5 in Appendix 3.A). Fig. 3A.6 (provided in Appendix 3.A) presents the variation of the ratios (region of influence of the disjoining pressure in the bulk of the droplet, $\Delta_1/\left(\frac{1}{\beta}\right)$, or the transition region, $\Delta_2/\left(\frac{1}{\phi_1}+\frac{1}{\phi_2}\right)$, to the relevant length scales) with an increase in a. Both ratios

increase with an increase in the slope of disjoining pressure isotherm. Fig. 3.12 also shows that slope *a* also influences the droplet profile: with an increase in the slope *a* of the disjoining pressure isotherm, the maximum height of the droplet increases which correspondingly increases the effective radius of the droplet.

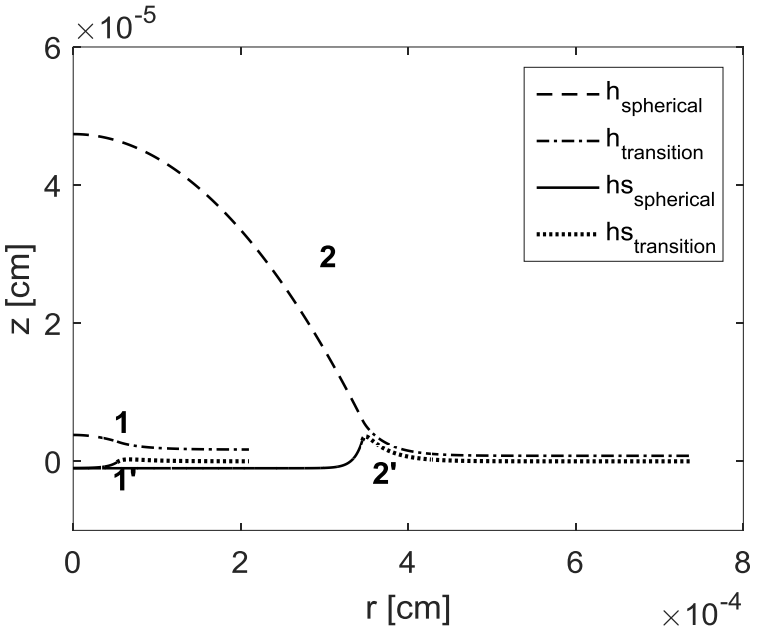

Figure 3.12: Effect of variation of a: Profiles of the droplet and substrate deformation, which are under consideration: $1, 1' - \ a = 1 \times 10^{11}$ dyn/cm^3, $2, 2' - \ a = 1 \times 10^{12}$ dyn/cm^3. Reproduced with permission from Ref.[113]. Copyright © 2016 Elsevier B.V.

3.3.2.3 Effect of variation of elasticity coefficient, K

Elasticity coefficient determines the maximum depth to which the substrate gets deformed. In this section the elasticity coefficient is varied according to $1 \times 10^{-13} \leq K \leq 1 \times 10^{-11}$ cm^3/dyn. Fig. 3A.7 (provided in Appendix 3.A) shows that as K is increased (i.e. for a more elastic substrate) the $\theta_{e,d}$ decreases slightly. Fig. 3A.8 (provided in Appendix 3.A) describes the behavior of the substrate deformation when K is increased. As K increases, $h_{s,max}$ increases and $h_{s,min}$ decreases linearly. Note that as $K \to 0$ both $h_{s,max} \to 0$ and $h_{s,min} \to 0$. Fig. 3A.9 (provided in Appendix 3.A) depicts that the total region of influence of disjoining pressure increases with an increase in elasticity coefficient. Fig. 3A.10 (provided in Appendix 3.A) presents the variation of the ratios (region of influence of the

disjoining pressure in the bulk of the droplet, $\Delta_1/\left(\frac{1}{\beta}\right)$, or the transition region, $\Delta_2/\left(\frac{1}{\phi_1}+\frac{1}{\phi_2}\right)$, to the relevant length scales) with an increase in K. Both ratios increase with an increase in the elasticity coefficient, but $\Delta_2/\left(\frac{1}{\phi_1}+\frac{1}{\phi_2}\right)$ becomes constant around elasticity coefficient of 6×10^{-12}. The influence of decreasing the elasticity coefficient causes the profile of the droplet to approach the profile for non-deformable substrate which is evident from Fig. 3.13. Where "ND" stands for Non-Deformable substrate and "D" stands for Deformable substrate.

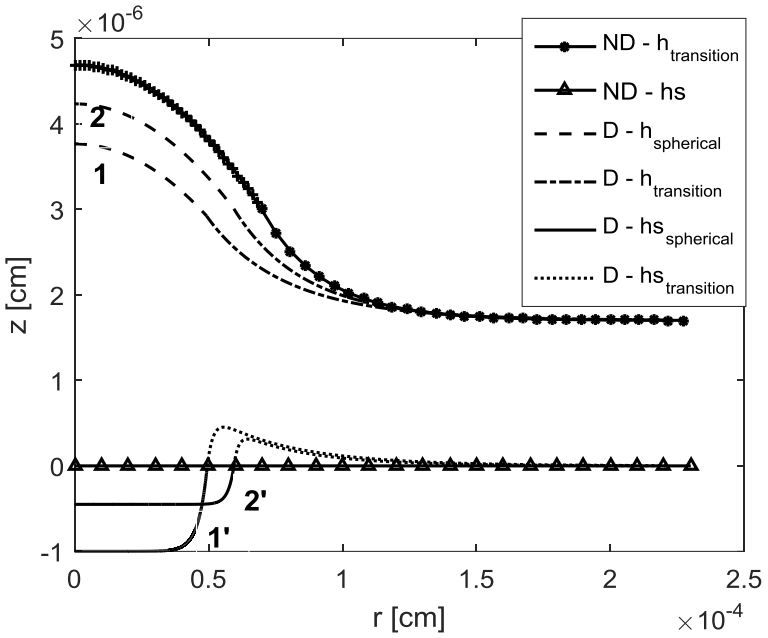

Figure 3.13: Effect of variation of K: Profiles of the droplet and substrate deformation, which are under consideration: $1, 1' - K = 1\times10^{-11}$ cm^3/dyn, $2, 2' - K = 4.5\times10^{-12}$ cm^3/dyn. Reproduced with permission from Ref.[113]. Copyright © 2016 Elsevier B.V.

3.3.2.4 Effect of variation of substrate surface tension, γ_s

According to Eq. (3.34) the substrate deformation dependency on the radius is described by Bessel function, $I_0(r\beta)$. This dependency show if $\gamma_s \to 0$ then the value $r\beta$ tends to infinity and so does $I_0(r\beta)$, however, simultaneously $C_{3,dg}$ tends to zero. Therefore, solution for h_s under the bulk of the droplet approaches KP_e for small γ_s. Substrate surface tension is varied according to $0.001 \le \gamma_s \le 30$ dyn/cm.

Increasing γ_s causes $\theta_{e,d}$ to increase slightly as shown in Fig. 3A.11 (provided in Appendix 3.A). Fig. 3A.12 (provided in Appendix 3.A) shows that $h_{s,max}$ decreases with increase in γ_s , whereas $h_{s,min}$decreases as γ_s increases. It shows that $h_{s,max}$ reaches maximum values as γ_s approaches zero. Total region of influence of disjoining pressure increases with an increase in γ_s, see Fig. 3A.13 (provided in Appendix 3.A). Fig. 3A.14 (provided in Appendix 3.A) presents the variation of the ratios (region of influence of the disjoining pressure in the bulk of the droplet, $\Delta_1/\left(\frac{1}{\beta}\right)$, or the transition region, $\Delta_2/\left(\frac{1}{\phi_1}+\frac{1}{\phi_2}\right)$, to the relevant length scales) with an increase in γ_s. Both ratios decrease with an increase in substrate's surface tension. Fig. 3.14 shows that there is a smooth transition of the substrate deformation from the bulk droplet to the region of thin films. However, when γ_s tends to zero this smooth transition in the substrate deformation tends to transform into a sharp jump (Fig. 3.14) and $h_{s,max}$ reach a maximum value when γ_s tends to zero.

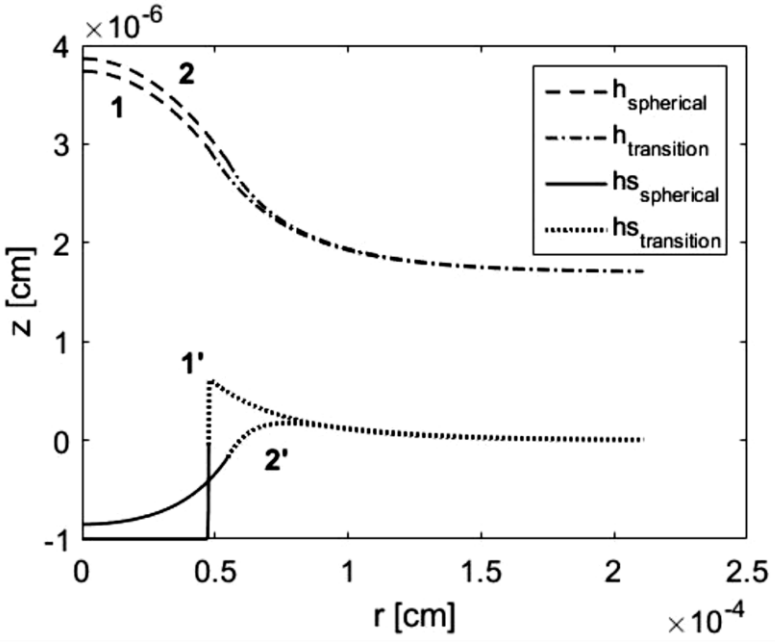

Figure 3.14: Effect of variation of $\boldsymbol{\gamma_s}$: Profiles of the droplet and substrate deformation , which are under consideration: $1, 1' - \gamma_s = 0.001$ dyn/cm, $2, 2' - \gamma_s = 30$ dyn/cm. Reproduced with permission from Ref.[113]. Copyright © 2016 Elsevier B.V.

3.4 Conclusions

Equilibrium of liquid droplets on deformable substrates is investigated. Disjoining pressure action in the vicinity of the apparent three phase contact line is taken into account. It is shown that the disjoining pressure action determines the substrate deformation. A simplified linear disjoining pressure isotherm and simple Winkler's model to account for the substrate deformation are used which allows deducing an analytical solutions for both the liquid profile and substrate deformation. The apparent equilibrium contact angle that the liquid makes with the substrate is calculated and its dependency on the system parameters is investigated. It is shown that the contact angles on the deformable substrate are always lower than on the corresponding non-deformable substrate. It is also shown that the estimated equilibrium contact angles of two-dimensional droplets on a non-deformable substrate are bigger as compared to three-dimensional droplets. Four parameters namely, excess pressure, slope of the disjoining pressure isotherm, elasticity coefficient of the substrate and substrate's surface tension, have been identified to affect the selected disjoining pressure isotherm. These parameters are varied independently to quantify their influence on the shape of the droplet and the deformation in the substrate. A region of influence of disjoining pressure on the deformable substrate is defined which is present under the transition zone and under the bulk of the droplet. Region of influence of disjoining pressure is decreased with decrease in excess pressure. For other parameters, slope of disjoining pressure isotherm, elasticity coefficient of the substrate and substrate's surface tension, it tends to increase as the parameters are increased. Reducing excess pressure reduces the apparent equilibrium contact angle, therefore causing the droplet to wet (i.e. small apparent equilibrium contact angle) the deformable substrate. This results in the depth of deformation to increase with a decrease in excess pressure. Increasing slope of the disjoining pressure isotherm increases the apparent equilibrium contact angle and the span of the droplet, but does not affect the maximum depth of substrate deformation. Elasticity coefficient has a direct effect on the depth of deformation of the substrate, i.e. increasing it causes the depth of deformation to increase. Apparent contact angle is less affected from an increase in elasticity coefficient. Surface tension of the deformable substrate substantially influences the profile of the substrate deformation. For lower values of substrate's surface tension, the deformation tends to a jump inside the transition zone. Interestingly this jump

created in the substrate cause a slight change in the profile of the droplet, i.e. the apparent contact angle increases slightly.

Nomenclature 3

a	slope of the disjoining pressure isotherm, $N.m^{-3}$
$C_{1,nd}$	integration constant
$C_{1,dg}$	integration constant
$C_{2,dg}$	integration constant
$C_{3,dg}$	integration constant
F	excess free energy of the droplet, N.m
$F_{e,film}$	excess free energy of the equilibrium thin film on the deformed solid, N.m
h	height of the fluid above the substrate, m
h_e	precursor film thickness, m
h_s	depth of deformation of the substrate, m
K	Elasticity, $m^3.N^{-1}$
L	effective radius of the droplet, m
L_1	length from the centre of the droplet to the point where surface forces (disjoining pressure) start to act, m
P_e	equilibrium excess pressure, Pa
r	length along radial direction, m
R	radius of curvature of the droplet, m
t_1	height of the droplet at which surface forces (disjoining pressure) start to act, m

Greek Symbols

$1/\beta$	length scale in the bulk of the droplet, m
γ	surface tension of the fluid, $N.m^{-1}$
γ_s	surface tension of the substrate, $N.m^{-1}$
Δ_1	region of influence of disjoining pressure in the bulk of the droplet, m
Δ_2	region of influence of disjoining pressure in the transition zone, m
θ_e	equilibrium contact angle
$\theta_{e,2D}$	two-dimensional equilibrium contact angle
$\theta_{e,nd}$	apparent equilibrium contact angle on a non-deformable substrate
$\theta_{e,d}$	apparent equilibrium contact angle on a deformable substrate
$\Pi(h)$	disjoining pressure isotherm, Pa
$1/\phi_1$, $1/\phi_2$	Length scales in the transition zone, m

Subscripts

ND	Non-deformable substrate
D	Deformable substrate
spherical	Bulk region of the droplet
transition	Region from bulk of the droplet to the thin film
out	Solution of the bulk/spherical part of the droplet
in	Solution of the transition region

Appendix 3.A

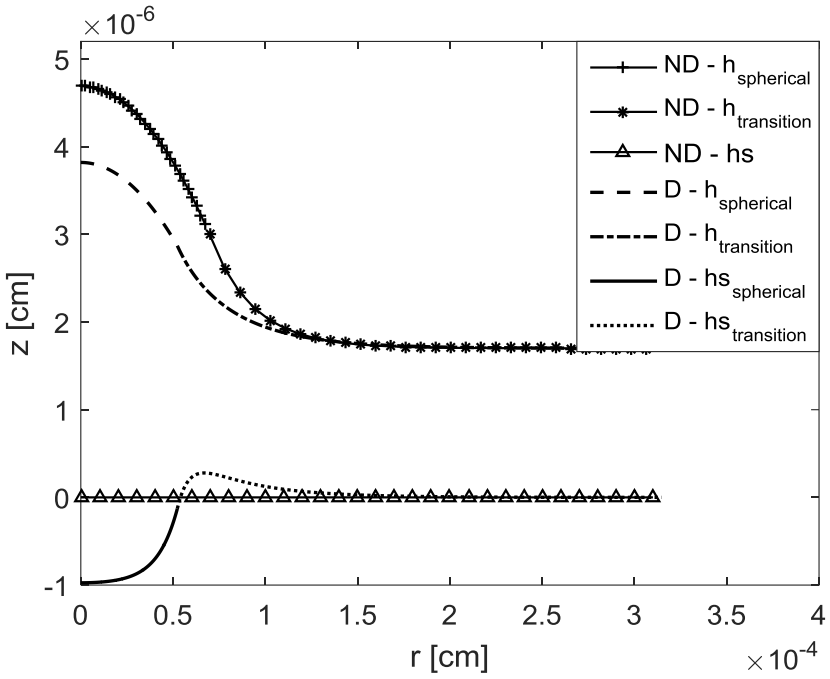

Figure 3A.1: Comparison between the profiles of the droplet and substrate for Non-Deformable (ND) and Deformable (D) substrate, where $\gamma_s = 10$ dyn/cm. Reproduced with permission from Ref.[113]. Copyright © 2016 Elsevier B.V.

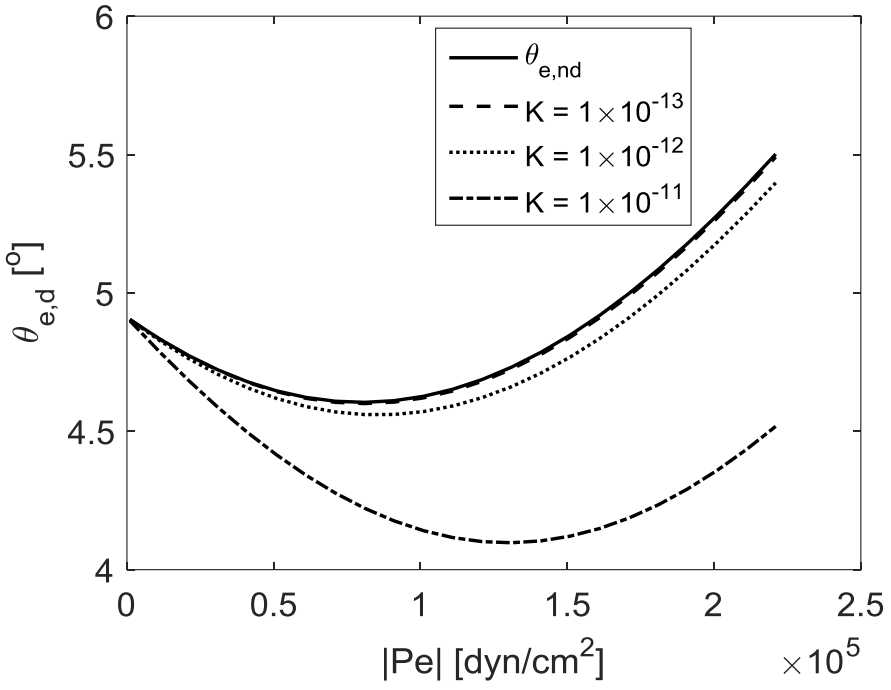

a) $t_0 = 7 \times 10^{-7}$ cm

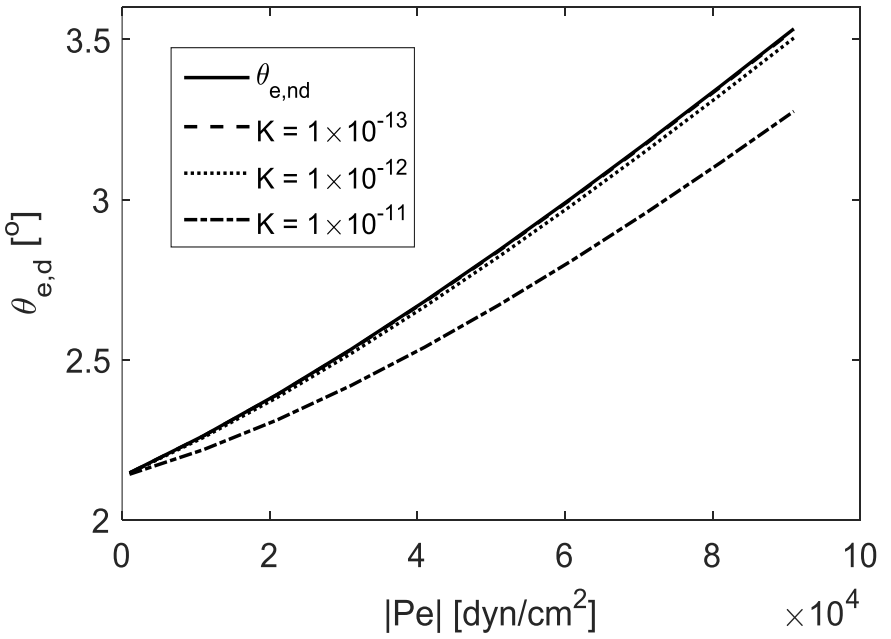

b) $t_0 = 2 \times 10^{-6}$ cm

Figure 3A.2: Effect of variation of P_e: Change in $\theta_{e,d}$ for different values of elasticity coefficient, K. Reproduced with permission from Ref.[113]. Copyright © 2016 Elsevier B.V.

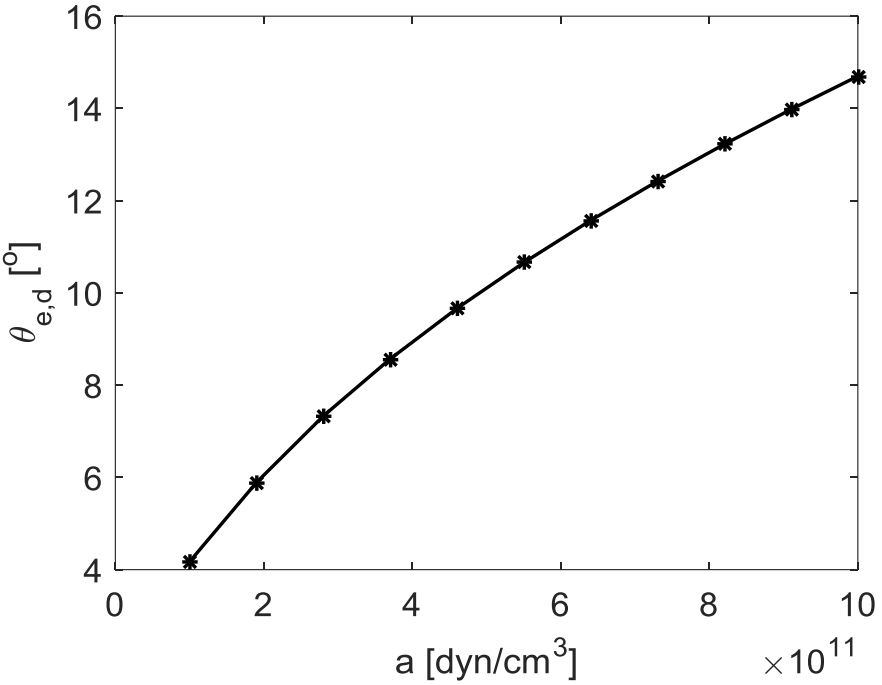

Figure 3A.3: Effect of variation of a: Change in apparent equilibrium contact angle. Reproduced with permission from Ref.[113]. Copyright © 2016 Elsevier B.V.

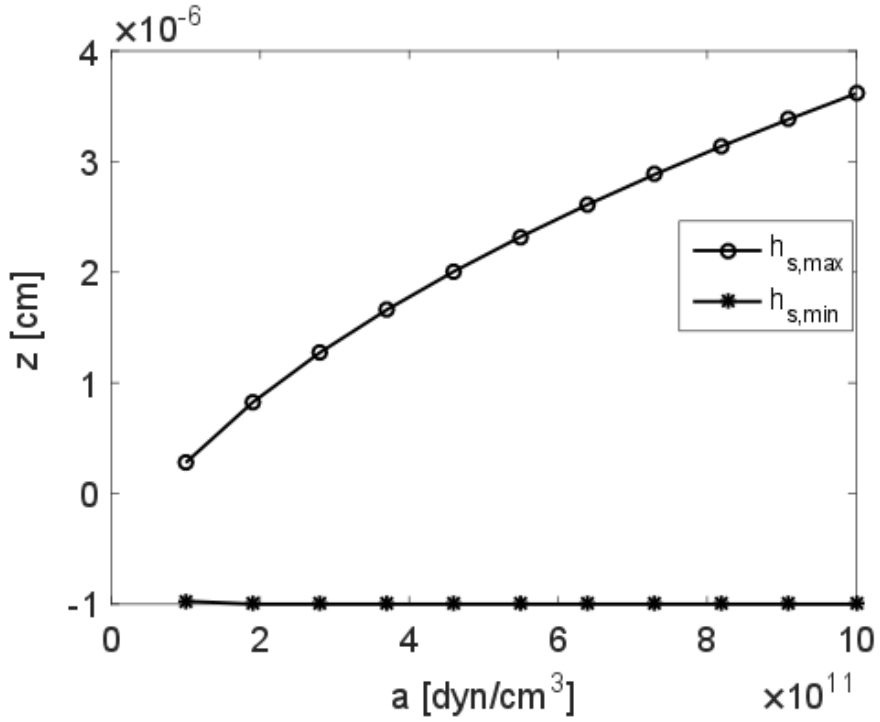

Figure 3A.4: Effect of variation of a: Change in substrate deformation. Reproduced with permission from Ref.[113]. Copyright © 2016 Elsevier B.V.

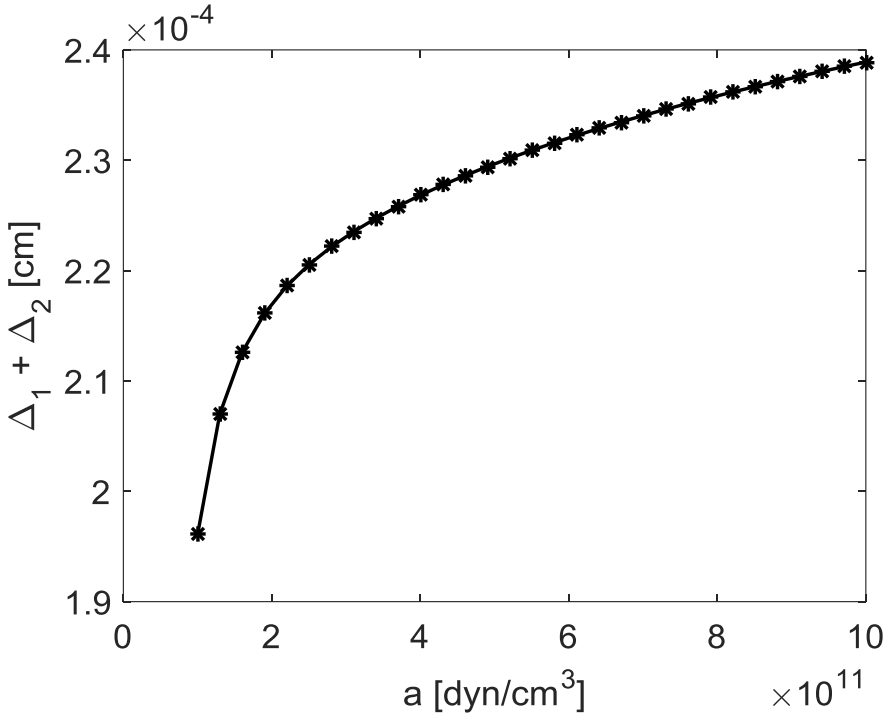

Figure 3A.5: Effect of variation a on the total region of influence of disjoining pressure. Reproduced with permission from Ref.[113]. Copyright © 2016 Elsevier B.V.

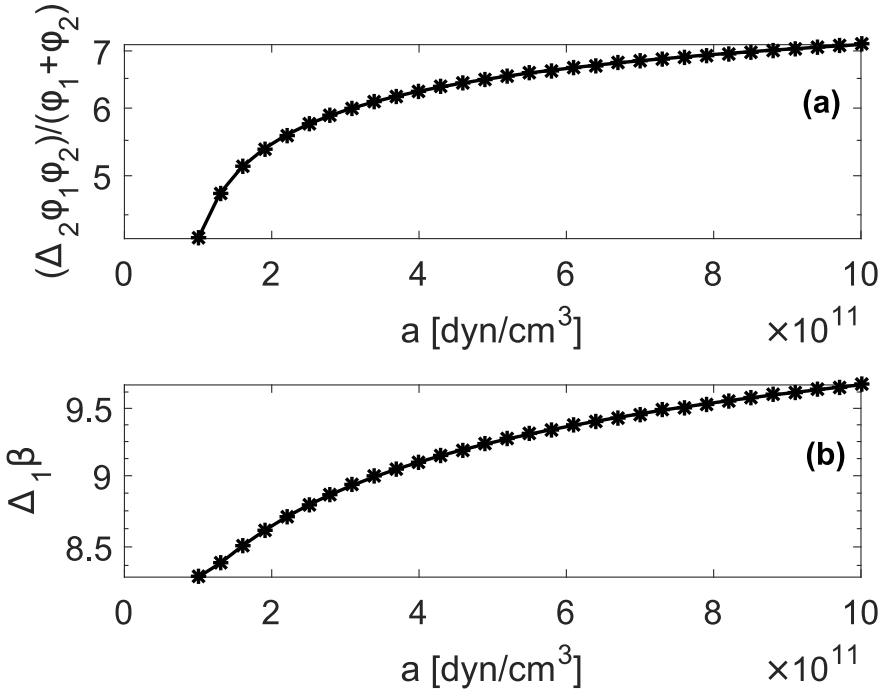

Figure 3A.6: Ratio of regions of influence of disjoining pressure to relevant scale plotted against a. Reproduced with permission from Ref.[113]. Copyright © 2016 Elsevier B.V.

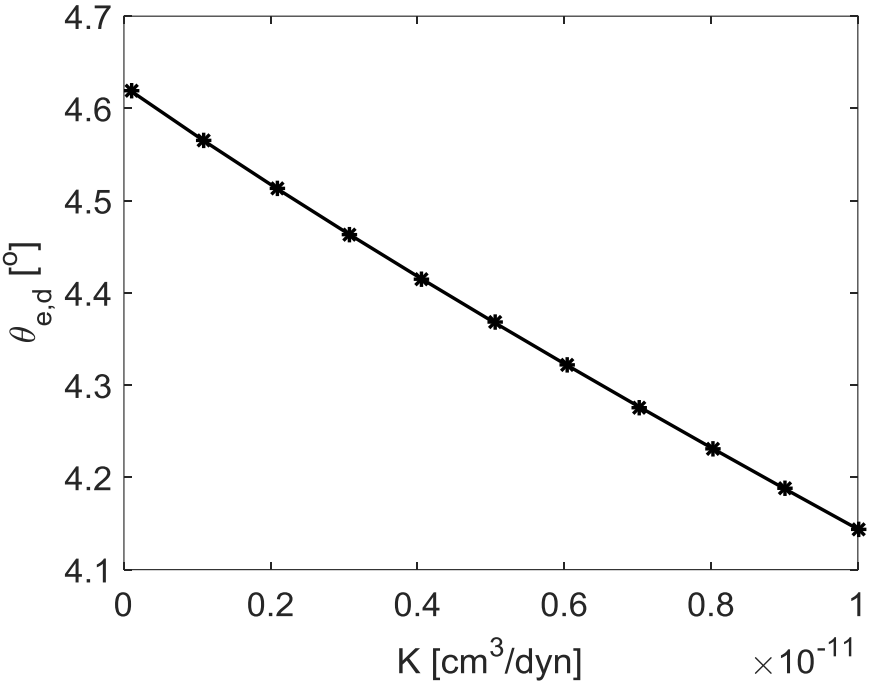

Figure 3A.7: Effect of variation of K: Change in apparent equilibrium contact angle. Reproduced with permission from Ref.[113]. Copyright © 2016 Elsevier B.V.

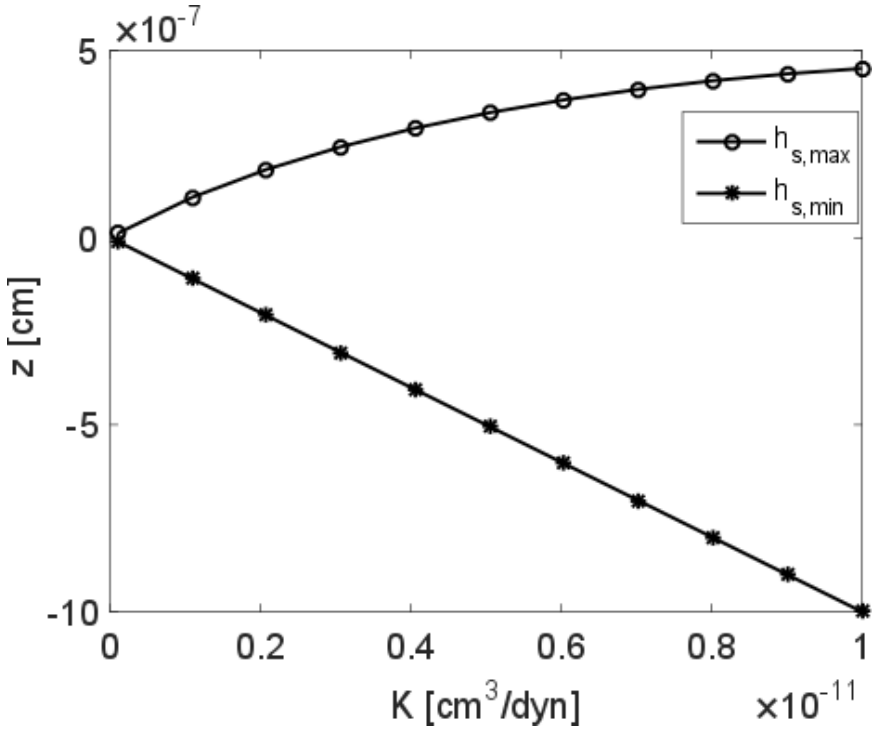

Figure 3A.8: Effect of variation of K: Change in substrate deformation. Reproduced with permission from Ref.[113]. Copyright © 2016 Elsevier B.V.

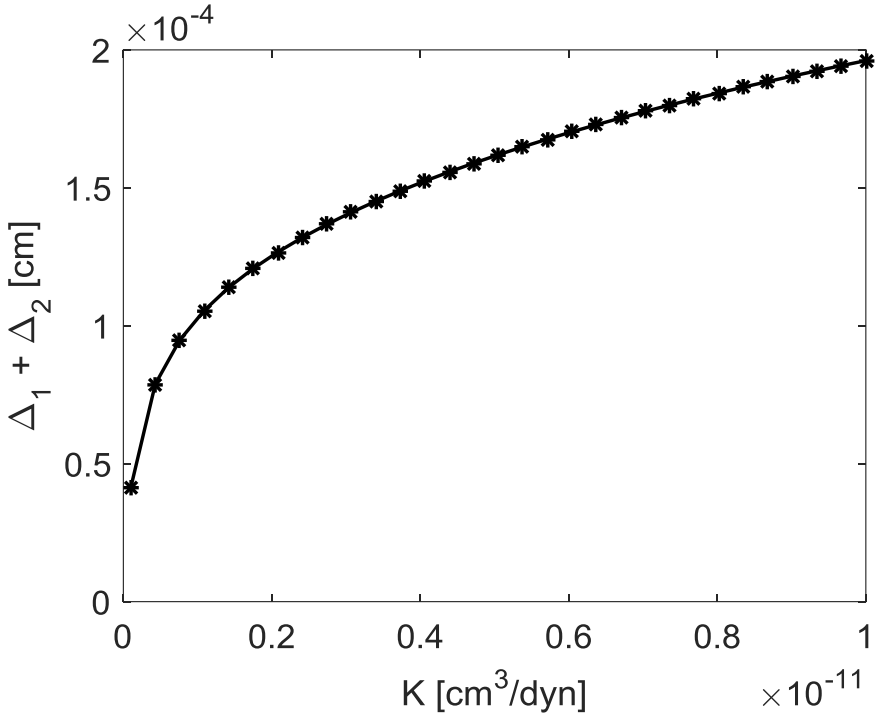

Figure 3A.9: Effect of variation *K* on the total region of influence of disjoining pressure. Reproduced with permission from Ref.[113]. Copyright © 2016 Elsevier B.V.

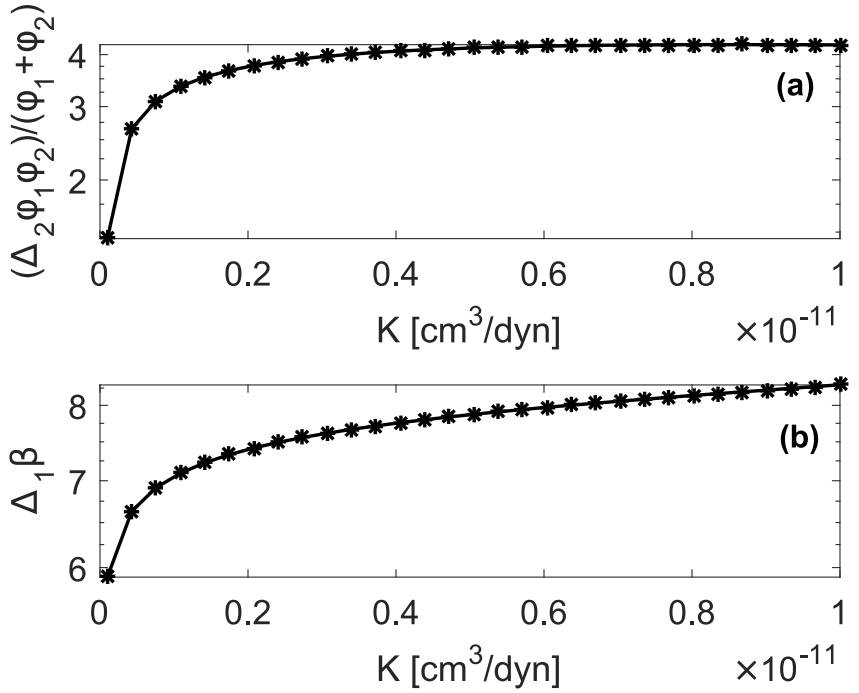

Figure 3A.10: Ratio of regions of influence of disjoining pressure to relevant scale plotted against *K*. Reproduced with permission from Ref.[113]. Copyright © 2016 Elsevier B.V.

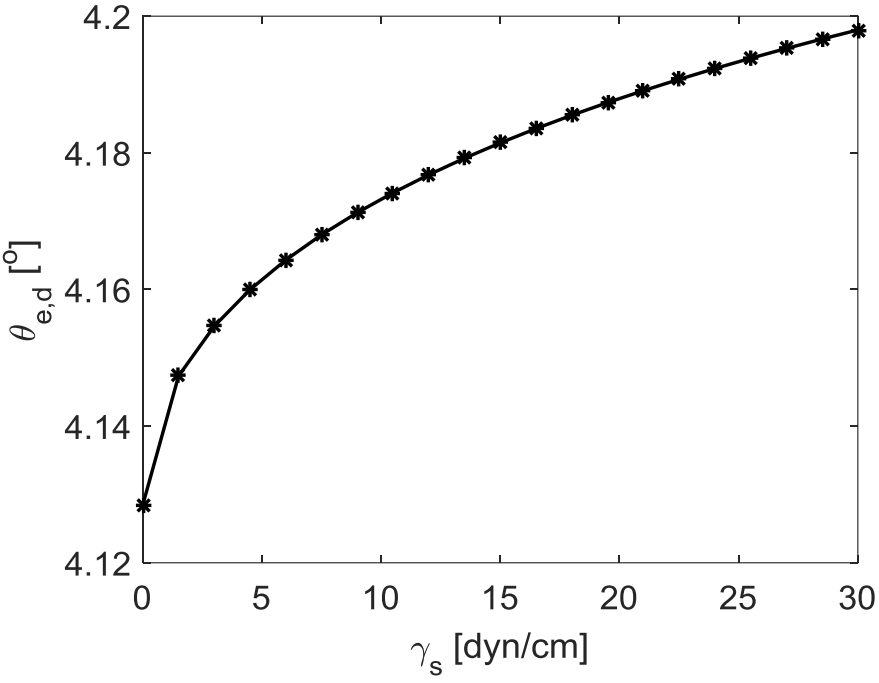

Figure 3A.11: Effect of variation of γ_s: Change in apparent equilibrium contact angle. Reproduced with permission from Ref.[113]. Copyright © 2016 Elsevier B.V.

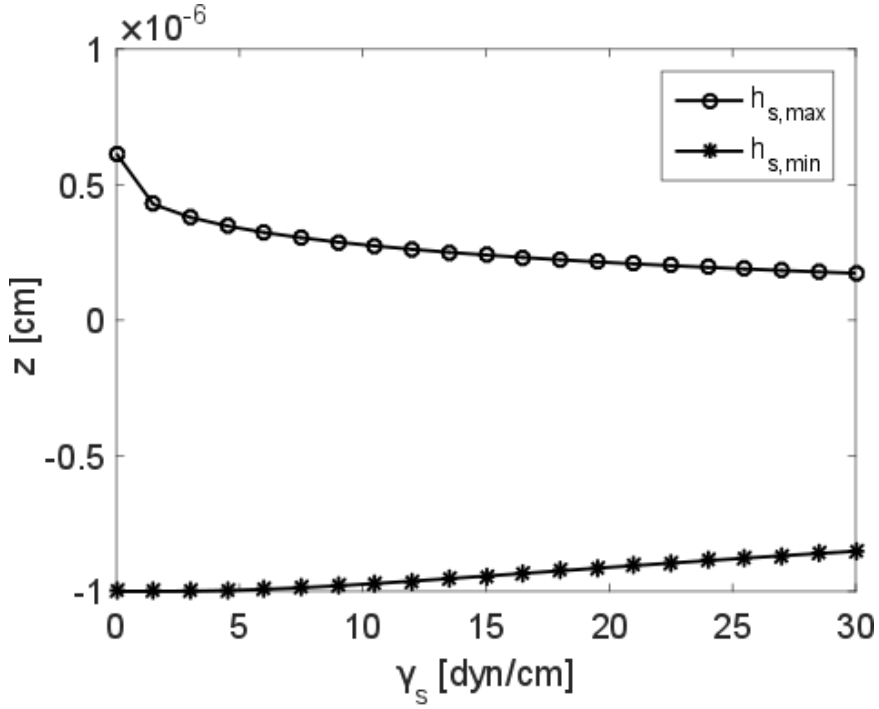

Figure 3A.12: Effect of variation of γ_s: Change in substrate deformation. Reproduced with permission from Ref.[113]. Copyright © 2016 Elsevier B.V.

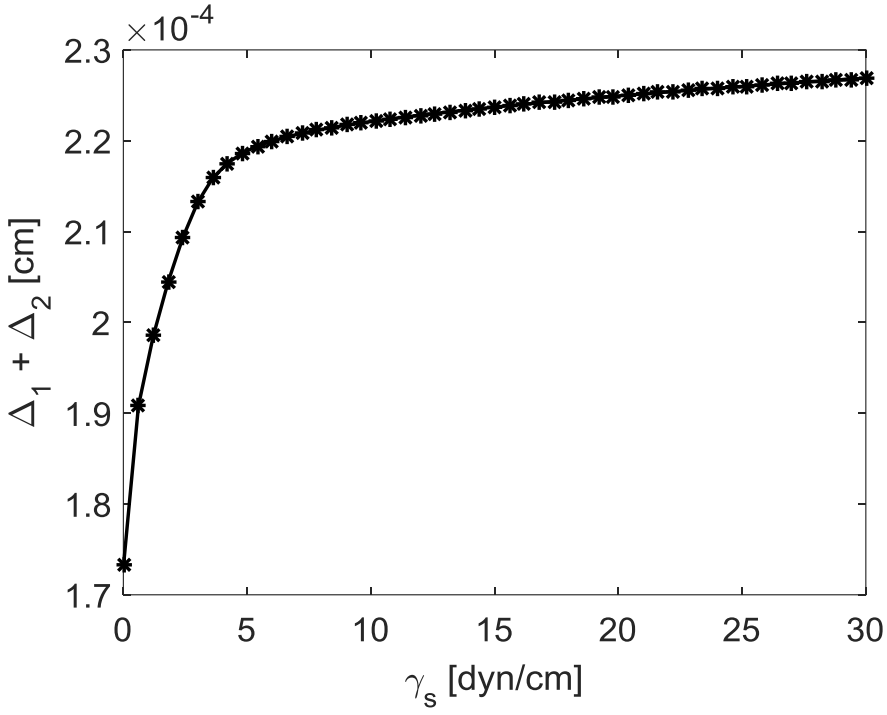

Figure 3A.13: Effect of variation γ_s on the total region of influence of disjoining pressure. Reproduced with permission from Ref.[113]. Copyright © 2016 Elsevier B.V.

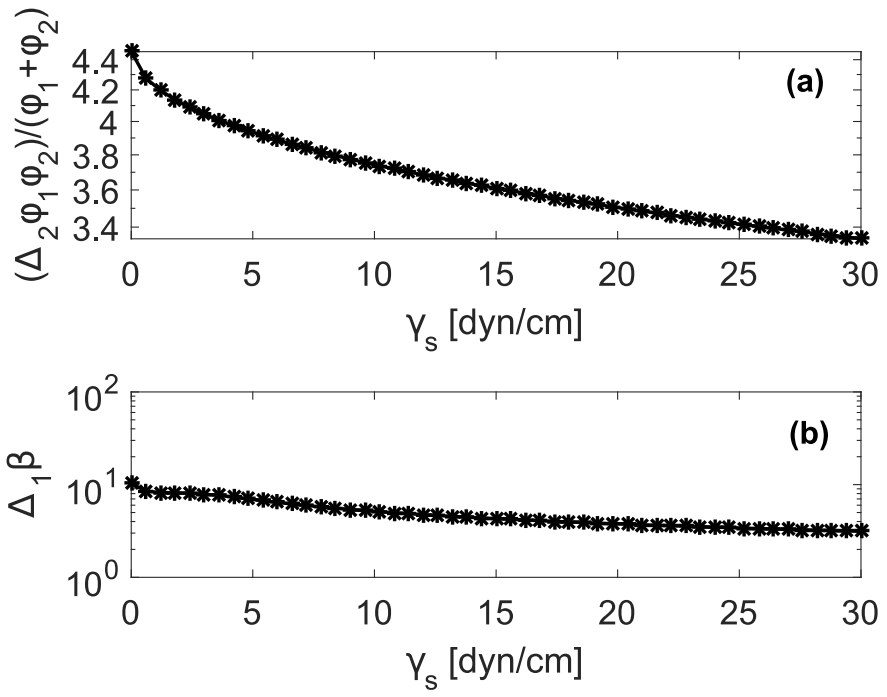

Figure 3A.14: Ratio of regions of influence of disjoining pressure to relevant scale plotted against γ_s. Reproduced with permission from Ref.[113]. Copyright © 2016 Elsevier B.V.

CHAPTER 4

KINETICS OF WETTING AND SPREADING OF NON-NEWTONIAN LIQUIDS OVER POROUS SUBSTRATES

Overview

Kinetics of wetting and spreading of blood as a non-Newtonian colloidal suspension over different porous substrates is investigated theoretically and experimentally in this chapter[1]. The results of investigations were published earlier in *Journal of Colloid and Interface Science* 446, 218–225, 2015 and *Colloids and Surfaces A: Physicochemical and Engineering Aspects* 505, 9–17, 2016 and reused in this chapter with permission. Initially in this chapter, the difference between a partial wetting and complete wetting of the porous substrate is determined in the process of spreading and imbibition. Then a mathematical model is developed for the case of complete wetting. In the next section, the predicted results for the case of complete wetting are compared with the experimental data and then the different features of partial wetting and complete wetting cases are identified and discussed.

4.1 Introduction

In this chapter theoretical and experimental findings on spreading and wetting of dry thin porous substrates by blood droplets is presented. This process is a representation of dried blood spot (DBS) sampling which is a method of blood collection.[3] In DBS sampling a thin porous substrate such as cotton fibres, cellulous fibres or polymer membrane is used to collect a small amount of blood droplet from a fingertip or syringe: the drop spreads over a porous substrate, imbibes into and preserves there as a dried spotted sample. Therefore, the sampling process can be described as spreading of blood, which is a non-Newtonian fluid, over a thin porous substrate with simultaneous spreading and penetration inside the porous substrate.

[1] Statement of contributions of joint authorship: Omid Arjmandi-Tash developed the mathematical model presented in this chapter and the experiments were conducted by Tzu Chieh Chao.

A hydrodynamic based mathematical model under lubrication approximation theory has been developed to describe complete wetting of thin porous layer by blood droplets. The result of comparison between the predicted values and experimental data is given below in the case of complete wetting. In addition, the influence of hydrophobicity of porous substrate has been identified by considering the cases in which the blood droplet wets only partially the porous substrate. To gain a better understanding of the blood drop spreading/imbibition process, firstly the difference between a complete wetting and a partial wetting of porous substrate is discussed below.

4.1.1 Partial wetting case

The spreading and imbibition behaviour of a droplet over a porous substrate in the case of partial wetting can be subdivided into 3 subsequent stages as schematically shown in Fig. 4.1:[116] Stage (1), during this stage the droplet spreads relatively fast over thin porous substrate until the radius of the droplet base reaches the maximum value, L_{ad}, and the contact angle decreases to the value of static advancing contact angle, θ_{ad}; Stage (2), during the second stage the three-phase contact line remains fixed at the maximum value while the contact angle decreases from the static advancing contact angle, θ_{ad}, to static receding contact angle, θ_r, due to the loss of droplet volume caused by the imbibition into the porous substrate; Stage (3), during the third stage of spreading/imbibition the drop base shrinks at approximately constant static receding, θ_r, contact angle until the time the droplet is sucked completely by porous substrate.

The characteristic feature of partial wetting case is the presence of contact angle hysteresis: this results in the existence of Stage 2, in which the edge of the droplet is pinned.

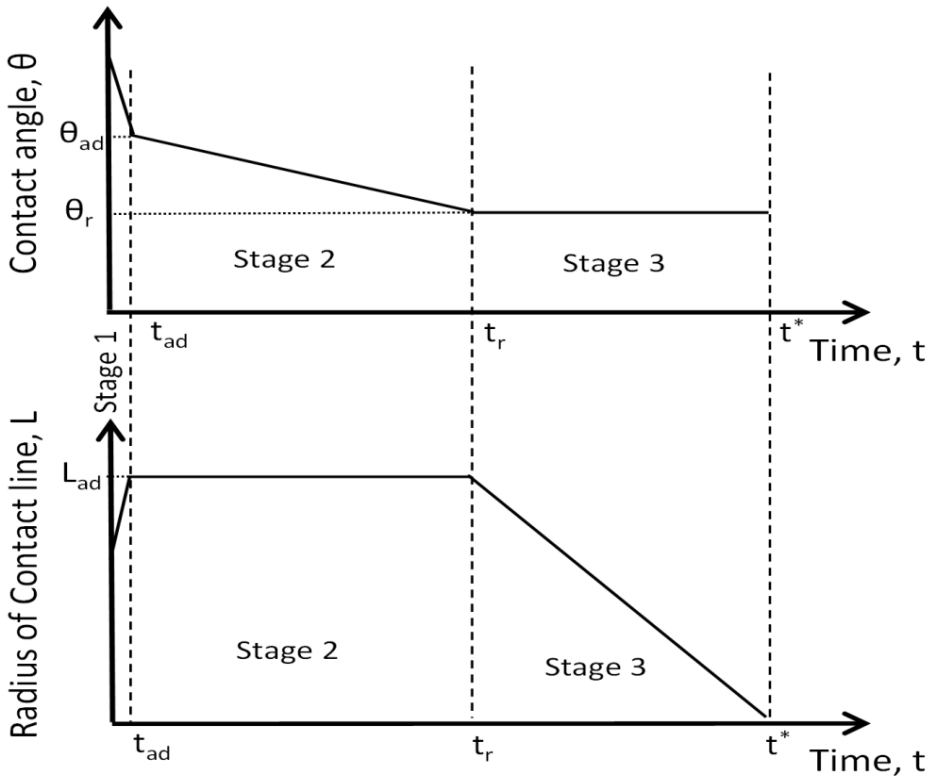

Figure 4.1: Three stages of spreading/imbibition of droplet over porous substrate in the case of partial wetting: L_{ad} is the maximum radius of droplet base, θ_{ad} is the advancing contact angle, t_{ad} is the time when θ_{ad} is reached, θ_r is the receding contact angle, t_r is the time when θ_r is reached and t^* is the time when imbibition is finished completely. Reproduced with permission from Ref.[116]. Copyright © 2016 Elsevier B.V.

4.1.2 Complete wetting case

There is no contact angle hysteresis in the case of complete wetting; therefore, Stage 2 of partial wetting is absent in complete wetting case and there are only two stages of spreading (see Fig. 4.2):[117, 118] Stage (1), during this stage the droplet spreads quickly over porous substrate and radius of the droplet base reaches its maximum value, L_m; Stage (3), in this stage the imbibition prevails over the spreading and the radius of the droplet base shrinks until complete disappearance. Note, over the most part of the Stage 3 in the case of complete wetting the contact angle retains the constant value, which has nothing to do with contact angle hysteresis (there is no contact angle hysteresis in the case of complete wetting) but determined by a pure hydrodynamic reason.

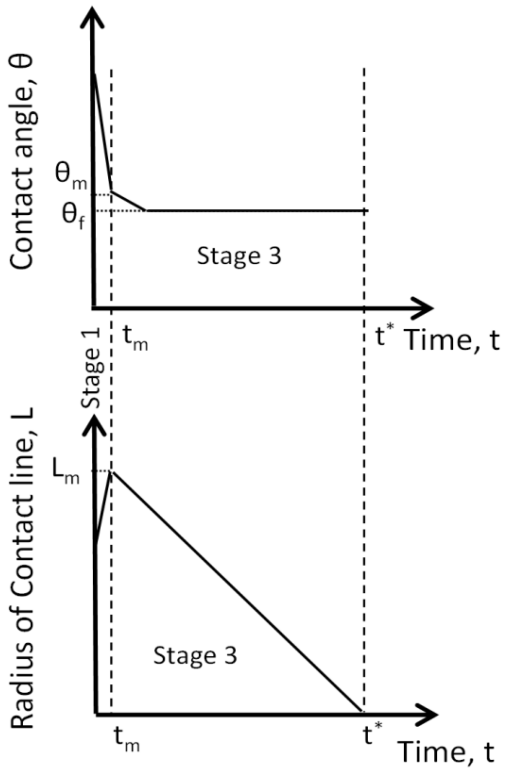

Figure 4.2: Two stages of spreading/imbibition of droplet over porous substrate in the case of complete wetting: L_m is the maximum radius of droplet base, t_m is the time when L_m is reached, θ_m is the contact angle at t_m, t^* is the time when complete imbibition is finished and θ_f is the final contact angle at t^*. Note, in the case of complete wetting the stage 2 is absent (see Fig. 4.1). Reproduced with permission from Ref.[116]. Copyright © 2016 Elsevier B.V.

Below the spreading behaviour of blood, which is a non-Newtonian liquid, over different thin porous substrates is investigated. The problem under investigation is similar to that considered in Ref.[119] when a drop of Newtonian liquid spreads over a dry porous layer, however, the difference is that now the liquid is a non-Newtonian blood. Blood spreading deviates from the corresponding Newtonian liquid in two ways: (i) the droplets spreading governs by a different law as compared with Newtonian liquids and (ii) non-Newtonian liquid imbibition into a porous substrate differs from that of Newtonian liquids.

The problem is treated below under the lubrication theory approximation and in the case of complete wetting. Spreading of "big drops", that is, bigger as compared with thickness of the porous substrate but still small enough to neglect the gravity action over "thin porous layers" is considered below.

4.2 Materials and methods

4.2.1 Theory

The kinetics of blood droplet motion both above and within the porous layer itself is taken into account below in the case of complete wetting. Fig. 4.3 shows the schematic of the axis-symmetric drop spreading over a thin porous substrate with a thickness of Δ, which is considered to be much smaller than the droplet height, i.e. $\Delta << h^*$, where h^* is the scale of the drop height. It was assumed that the slope of the droplet profile is low, $h^*/L^* << 1$, where L^* is the scale of the drop base. That is, only small droplets are under consideration: the gravity action is neglected and only capillary forces are taken into account (Bond number $\rho g L^{*2}/\gamma << 1$, where ρ, g, and γ are the liquid density, gravity acceleration and the liquid-air interfacial tension, respectively). The time evolution of spreading radius, $L(t)$, the droplet height, $h(t)$ and radius of the wetted area inside the porous substrate, $\ell(t)$, were monitored during the spreading experiments.

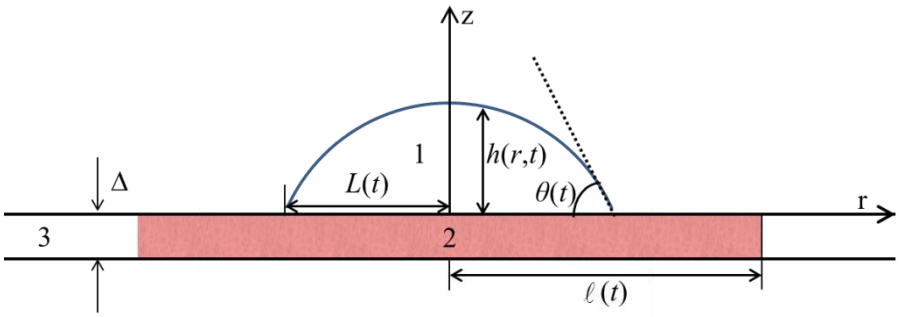

Figure 4.3: Cross-section of the axis-symmetric spreading drop over initially dry porous substrate with thickness Δ. 1- liquid drop; 2- wetted region inside the porous substrate; 3- dry region inside the porous substrate. $L(t)$- radius of the drop base; $\ell(t)$ - radius of the wetted area inside the porous substrate; $\theta(t)$ - contact angle; Δ- thickness of porous substrate; r, z co-ordinate system. Reproduced with permission from Refs.[116, 117].

4.2.1.1 Droplet profile

According to Ref.[57], the droplet profile in the case of capillary spreading, except for a small region close to the three-phase contact line, remains a spherical cap:

$$h(t,r)=\frac{2V}{\pi L^4}(L^2-r^2),\quad r<L(t)\,. \tag{4.1}$$

where V is the droplet volume. The above expression is identical for both Newtonian and non-Newtonian liquids.[57]

A modified Darcy's law is developed in Appendix 4.A to describe the flow of a non-Newtonian liquid in a thin porous layer. The porous layer is assumed to be thin enough and the time for saturation in the vertical direction can be neglected relative to other time scales of the process. The time required for a complete saturation of the porous layer in the vertical direction, t_Δ, can be estimated in the same way as in Ref.[119] and accordingly, the porous layer beneath the spreading drop ($0<r<L(t)$) is always assumed to be completely saturated.

The capillary pressure inside the porous layer can be estimated as $p_c\approx\frac{2\gamma}{a^*}$, where γ is the surface tension and a^* is the scale of capillary radii inside the porous layer. The capillary pressure inside the drop, p-p_g, can be approximated as $p-p_g\approx\frac{\gamma h^*}{L^{*2}}=\frac{h^*}{L^*}\frac{\gamma}{L^*}<<\frac{\gamma}{L^*}<<\frac{\gamma}{a^*}\approx p_c$, where p_g is the pressure in the ambient air. According to the latter expression, the capillary pressure inside the drop can be neglected as compared with the capillary pressure inside the porous layer.

The volume of the droplet over porous layer, $V(t)$, changes over time, t, due to the imbibition of the liquid inside the porous layer, this means:

$$V(t)=V_0-\varepsilon\pi\Delta\,\ell^2(t), \tag{4.2}$$

where V_0 is the initial volume of the drop; ε is the porosity of the porous layer. Here the wetted region inside the porous layer is considered to be a cylinder with radius $\ell(t)$ and the height Δ.

If it is supposed that t^* is the time instant when the drop is completely sucked by the porous substrate, $V(t^*)=0=V_0-\varepsilon\pi\Delta\ell^{*2}$; where ℓ^* is the maximum radius of the wetted region in the porous layer and it can be obtained as

$$\ell^*=\left(\frac{V_0}{\pi\varepsilon\Delta}\right)^{1/2}. \tag{4.3}$$

ℓ^* is used below to scale the radius of the wetted region in the porous layer, $\ell(t)$.

The following value of the dynamic contact angle, θ, ($\tan\theta \approx \theta$) can be deduced from Eq. (4.1):

$$\theta = \frac{4V}{\pi L^3}, \tag{4.4}$$

or

$$L = \left(\frac{4V}{\pi\theta}\right)^{1/3}. \tag{4.5}$$

4.2.1.2 Droplet spreading over porous substrate in the case of complete wetting

The drop motion over porous substrate in the case of complete wetting can be considered to be a superposition of two motions:[65,117] (a) an expansion of the drop base as a result of spreading over already saturated part of the porous layer, and (b) a shrinkage of the drop base as a result of the imbibition into the porous layer. Hence, the following equation can be written for the rate of the drop base motion:

$$\frac{dL}{dt} = v_+ - v_-, \tag{4.6}$$

where v_+, v_- are unknown velocities of the expansion and the shrinkage of the drop base, respectively.

A time derivative of both sides of Eq. (4.5) results in:

$$\frac{dL}{dt} = -\frac{1}{3}\left(\frac{4V}{\pi\theta^4}\right)^{1/3}\frac{d\theta}{dt} + \frac{1}{3}\left(\frac{4}{\pi V^2\theta}\right)^{1/3}\frac{dV}{dt}. \tag{4.7}$$

During the spreading process of the droplet over the porous layer both its contact angle and volume can only decrease over time. Therefore, in the above equation the first term in the right hand side is always positive and the second term is always negative.

Comparison of the Eqs. (4.6) and (4.7) leads to the following expressions for v_+, v_-:

$$v_+ = -\frac{1}{3}\left(\frac{4V}{\pi\theta^4}\right)^{1/3}\frac{d\theta}{dt} > 0, \quad v_- = -\frac{1}{3}\left(\frac{4}{\pi V^2\theta}\right)^{1/3}\frac{dV}{dt} > 0 \tag{4.8}$$

The above equations can be justified as follows: there are two substantially different characteristic time scales in the problem under consideration: $T_\mu = t_\mu^* << t_p^* = T_p$, where t_μ^* and t_p^* are time scales of the viscous spreading and the imbibition into the porous layer, respectively; $\delta = \frac{t_\mu^*}{t_p^*} << 1$ is a smallness parameter (around 0.08 for Newtonian fluid[119]). Accordingly, the following function can be written for the droplet motion: $L = L(T_\mu, T_p)$, where T_μ is a time of the fast viscous spreading and T_p is a time of the slow imbibition into the porous substrate. The time derivative of $L(T_\mu, T_p)$ is

$$\frac{dL}{dt} = \frac{\partial L}{\partial T_\mu} + \frac{\partial L}{\partial T_p}. \tag{4.9}$$

Comparison of Eqs. (4.6), (4.8) and (4.9) results in

$$v_+ = \frac{\partial L}{\partial T_\mu} = -\frac{1}{3}\left(\frac{4V}{\pi\theta^4}\right)^{1/3}\frac{d\theta}{dt}, \quad v_- = \frac{\partial L}{\partial T_p} = -\frac{1}{3}\left(\frac{4}{\pi V^2\theta}\right)^{1/3}\frac{dV}{dt} \tag{4.10}$$

The loss of the droplet volume over time is caused only by the penetration into the porous layer and; hence, the drop volume, *V*, only depends on the slow time scale.

According to the above consideration the whole spreading/imbibition process of droplet over porous substrate in the case of complete wetting can be subdivided into two stages:

(i) First fast stage, when the imbibition into the porous substrate is negligible, and the drop spreads with approximately constant volume. This stage goes in the same way as the spreading over saturated porous layer and the arguments developed in Ref.[120] can be used here;

(ii) Second slower stage, when the spreading process is almost over and the drop evolution is governed mostly by the imbibition into the porous substrate.

For the first stage of the process the spreading radius of the droplet produced from non-Newtonian power-law liquid can be found as:[57]

$$L(t) = \left[\frac{n}{2n+1}\frac{\lambda}{\alpha_n}\left(\frac{\gamma}{k}\right)^{1/n}\frac{V_0^{(n+2)/n}}{(2\pi)^{(n+2)/n}}(t+t_0)\right]^{\alpha_n}, \tag{4.11}$$

where n and k respectively are the flow behavior index and flow consistency index of the known Otswald-de Waele relationship; $\alpha_n = \frac{n}{3n+7}$ and t_0 is the duration of the initial stage of spreading, when the capillary regime of spreading is not applicable; λ is a constant, determined in Ref.[120]. Note, the parameter λ is independent of the droplet volume.[120]

The parameter α_n changes from 0 to 1/3 at n=0 to $n\to\infty$ and it equals to 0.1 in the case of Newtonian liquid at n=1; that is, the limits are: $0<\alpha_n<1/3$. In the case of a Newtonian liquid, Eq. (4.11) leads to the well-known spreading law of $L(t) \sim (t+t_0)^{0.1}$ for a complete wetting case.[26] Eq. (4.11) indicates that pseudo plastic fluids, n<1, spread slower and dilatant fluids, n>1, spread faster than Newtonian liquids.

The characteristic time scale of the first stage of spreading according to Eq. (4.11) can be found as:

$$t_\mu^* = \frac{(2\pi)^{(n+2)/n} L_0^{1/\alpha_n}}{\frac{n}{2n+1}\frac{\lambda}{\alpha_n}\left(\frac{\gamma}{k}\right)^{1/n} V_0^{(n+2)/n}}, \tag{4.12}$$

where $L_0 = L(0)$ is the radius of the droplet base in the end of the very fast initial stage of spreading. Using the above scale Eq. (4.11) can be rewritten as:

$$L(t) = L_0\left[\frac{t+t_0}{t_\mu^*}\right]^{\alpha_n}. \tag{4.13}$$

Combination of Eqs. (4.13), (4.8) and (4.4) gives the expansion velocity of the drop base, v_+:

$$v_+ = \left(\frac{V(t)}{V_0}\right)^{1/3} \frac{\alpha_n L_0}{\left(\frac{t+t_0}{t_\mu^*}\right)^{1-\alpha_n} t_\mu^*}. \tag{4.14}$$

In addition, substitution of Eq. (4.2) into the Eq. (4.8) results in the following expression for the shrinkage velocity of the drop base, v_-:

$$v_- = \frac{2\pi^{2/3}\varepsilon\Delta\ell}{3}\left(\frac{4}{\left(V_0 - \varepsilon\pi\Delta\ell^2\right)^2\theta}\right)^{1/3}\frac{d\ell}{dt}. \tag{4.15}$$

Substitution of Eqs. (4.14) and (4.15) into Eq. (4.6) results in:

$$\frac{\mathrm{d}L}{\mathrm{d}t}=\frac{\alpha_n\left(\frac{V}{V_0}\right)^{1/3}\left(\frac{n}{2n+1}\frac{\lambda}{\alpha_n}\left(\frac{\gamma}{k}\right)^{1/n}\frac{V_0^{(n+2)/n}}{(2\pi)^{(n+2)/n}}\right)^{\alpha_n}}{(t+t_0)^{1-\alpha_n}}-\frac{2\pi^{2/3}\varepsilon\Delta\ell}{3}\left(\frac{4}{\left(V_0-\varepsilon\pi\Delta\ell^2\right)^2\theta}\right)^{1/3}\frac{d\ell}{dt}. \quad (4.16)$$

The only unknown function in the above expression is the radius of the wetted region inside the porous layer, $\ell(t)$, which is determined below section.

4.2.1.3 Inside the porous layer outside the droplet (-Δ<z<0, L<r<ℓ)

The liquid penetrating inside the porous layer obeys the modified Darcy's law (Eq. 4A.10):

$$\frac{1}{r}\frac{\partial}{\partial r}\left(r\frac{\partial v}{\partial r}\right)=0,\quad v=K_n\left(\frac{1}{k}\left|\frac{\partial p}{\partial r}\right|\right)^{1/n}. \quad (4.17)$$

where K_n is the permeability of the porous layer. Solution of the above equations in the case of a non-Newtonian liquid ($n\neq1$) is

$$p=-\left(\frac{c}{K_n}\right)^n k\frac{r^{1-n}}{1-n}+b,\quad v=\frac{c}{r}, \quad (4.18)$$

where b and c are integration constants, which should be determined based on boundary conditions for the pressure at the drop edge, $r=L(t)$, and at the circular edge of the wetted region inside the porous layer, $r=\ell(t)$.

Note that the solution of Eq. (4.17) in the case of the imbibition of a Newtonian liquid is different from the case of power law non-Newtonian liquids:[119]

$$p=-(c\mu/K_p)\ln r+b;\quad v=\frac{c}{r}, \quad (4.19)$$

The boundary condition at the circular edge of the wetted region inside the porous layer is:

$$p=p_g-p_c,\quad r=\ell(t), \quad (4.20)$$

where $p_c\approx\frac{2\gamma}{a^*}$ is the capillary pressure inside the pores of the porous substrate, and a^* is a characteristic scale of the pore radii inside the porous layer.

The boundary condition at the drop edge is

$$p = p_g + p_d, \quad r = L(t), \tag{4.21}$$

where p_d is an unknown pressure inside the drop.[119] It was estimated above in section 4.2.1.1 and in Ref.[119] that $p_d << p_c$. That is, p_d in Eq. (4.21) is neglected below.

Both integration constants, *b* and *c*, in Eq. (4.18) can be determined using the above-mentioned two boundary conditions, and then the following expression can be deduced for the radial velocity:

$$v = \frac{K_n}{r}\left[\frac{(1-n)p_c}{k(\ell^{1-n} - L^{1-n})}\right]^{1/n}. \tag{4.22}$$

The velocity at the circular edge of the wetted region inside the porous layer is:

$$\varepsilon \frac{d\ell}{dt} = v\big|_{r=\ell}. \tag{4.23}$$

Substitution of Eq. (4.22) into Eq. (4.23) results in the following evolution equation for $\ell(t)$:

$$\frac{d\ell}{dt} = \frac{K_n}{\varepsilon \ell}\left[\frac{(1-n)p_c}{k(\ell^{1-n} - L^{1-n})}\right]^{1/n}. \tag{4.24}$$

An approximation of the time scale t_p^* in the same way as in Ref.[119] can be found according to Eq. (4.24) as:

$$t_p^* = \frac{\varepsilon \ell^{*(1+1/n)} k^{1/n}}{K_n p_c^{1/n}}. \tag{4.25}$$

The estimated values of t_μ^* according to Eq. (4.12) and t_p^* based on Eq. (4.25) proves that $t_\mu^* << t_p^*$ under all the experimental conditions.

Substitution of Eq. (4.24) into Eq. (4.16) leads to the following system of differential equations for the evolution of both the radius of the drop base, $L(t)$, and that of the wetted region inside the porous layer, $\ell(t)$:

$$\frac{\mathrm{d}L}{\mathrm{d}t}=\frac{\alpha_n\left(\frac{V}{V_0}\right)^{1/3}\left(\frac{n}{2n+1}\frac{\lambda}{\alpha_n}\left(\frac{\gamma}{k}\right)^{1/n}\frac{V_0^{(n+2)/n}}{(2\pi)^{(n+2)/n}}\right)^{\alpha_n}}{\left(t+t_0\right)^{1-\alpha_n}}, \tag{4.26}$$

$$-\frac{2L\pi\Delta}{3}\frac{K_n}{V_0-\pi\varepsilon\Delta\ell^2}\left[\frac{(1-n)p_c}{k(\ell^{1-n}-L^{1-n})}\right]^{1/n}$$

$$\frac{d\ell}{dt}=\frac{K_n}{\varepsilon\ell}\left[\frac{(1-n)p_c}{k(\ell^{1-n}-L^{1-n})}\right]^{1/n}. \tag{4.27}$$

The system of differential equations (4.26) and (4.27) can be made dimensionless using new scales $\bar{L}=L/L_m$, $\bar{\ell}=\ell/\ell^*$, $\bar{t}=t/t^*$, where L_m is the maximum radius of the droplet base, which is reached at the unknown time instant t_m when $\frac{\mathrm{d}L}{\mathrm{d}t}$=0 in Eq. (4.26). As mentioned above in Section 4.2.1.1 $\ell*$ is the maximum radius of the wetted region which is reached at time t^*. Note that the time instant t^* is unknown but according to the previous considerations, t_p^* (Eq. (4.25)) can be a good approximation of that. That is $t^*=\upsilon t_p^*$, where υ is an unknown parameter, which can depend on the flow behavior index, *n*, of the power law.

The same notations marked with an over-bar are used for dimensionless variables as for corresponding dimensional variables. Using the new scales, the system of Eqs. (4.26) and (4.27) is transformed into:

$$\frac{\mathrm{d}\bar{L}}{\mathrm{d}\bar{t}}=\frac{\upsilon A(1-\bar{\ell}^2)^{\frac{1}{3}}}{(\bar{t}+\bar{t}_0)^{1-\alpha_n}}-\frac{2\bar{L}}{3}\frac{\upsilon}{1-\bar{\ell}^2}\left[\frac{(1-n)}{(\bar{\ell}^{1-n}-\chi\bar{L}^{1-n})}\right]^{1/n}, \tag{4.28}$$

$$\frac{d\bar{\ell}}{d\bar{t}}=\frac{\upsilon}{\bar{\ell}}\left[\frac{(1-n)}{(\bar{\ell}^{1-n}-\chi\bar{L}^{1-n})}\right]^{1/n}, \tag{4.29}$$

where

$$\bar{t}_0=t_0/t^*<<1,\quad \chi=\left(\frac{L_m}{\ell*}\right)^{1-n},$$

$$A=\frac{2}{3}\frac{(\bar{t}_m+\bar{t}_0)^{1-\alpha_n}}{\left(1-\bar{\ell}_m^2\right)^{4/3}\left(\frac{\bar{\ell}_m^{1-n}-\chi}{1-n}\right)^{1/n}},\quad \bar{\ell}_m=\frac{\ell_m}{\ell^*}, \tag{4.30}$$

where ℓ_m is the radius of wetting region at the time instant t_m.

Eqs. (4.28) and (4.29) are a system of two first order differential equations, and, hence, two initial conditions, $\bar{L}(0)$ and $\bar{\ell}(0)$, should be imposed for solving them. The system of Eqs. (4.28) and (4.29) is singular at zero values of $\bar{L}(0)$ and $\bar{\ell}(0)$. Therefore, very small but non-zero values were selected instead:

$$\bar{L}(0) = 0.001, \tag{4.31}$$

$$\bar{\ell}(0) = 0.001, \tag{4.32}$$

The small initial time, $\bar{t}_0$, was selected as $\bar{t}_0 = 0.00001$ and the calculation showed that the results are almost independent of the small initial values selected.

Solution of Eqs. (4.28) and (4.29) should satisfy the following four extra conditions:

$$\bar{L}(1) = 0, \tag{4.33}$$

$$\bar{L}(\bar{t}_m) = 1, \tag{4.34}$$

$$\frac{d\bar{L}(\bar{t}_m)}{d\bar{t}} = 0, \tag{4.35}$$

$$\bar{\ell}(1) = 1. \tag{4.36}$$

Conditions (4.34) and (4.35) were used above to select an expression for *A* in Eq. (4.30) and conditions (4.33) and (4.36) are to be satisfied. Accordingly, the two unknown dimensionless parameters, χ and υ, in the system of differential equations (4.28) and (4.29) are determined by satisfying the precisely two extra conditions (4.33) and (4.36).

Comparison of Eqs. (4.10) and (4.28) gives the dimensionless velocities of the expansion, $\bar{v}_+$, and the shrinkage, $\bar{v}_-$, of the droplet base as:

$$\bar{v}_+ = \frac{\upsilon A (1-\bar{\ell}^2)^{\frac{1}{3}}}{(\bar{t}+\bar{t}_0)^{1-\alpha_n}},\ \bar{v}_- = \frac{2\bar{L}}{3}\frac{\upsilon}{1-\bar{\ell}^2}\left[\frac{(1-n)}{(\bar{\ell}^{1-n}-\chi\bar{L}^{1-n})}\right]^{1/n}. \tag{4.37}$$

Eq. (4.4) can be rewritten using the same dimensionless variables and $\bar{V} = V/V_0 = 1-\bar{\ell}^2$ as:

$$\theta = \frac{4V_0}{\pi L^3}(1-\bar{\ell}^2). \tag{4.38}$$

If we introduce $\theta_m = \frac{4V_0}{\pi L_m^3}(1-\bar{\ell}_m^2)$, which is the value of the dynamic contact angle at the time instant when the maximum value of the drop base is reached, then Eq. (4.38) can be transformed as:

$$\frac{\theta}{\theta_m} = \frac{(1-\bar{\ell}^2)/(1-\bar{\ell}_m^2)}{\bar{L}^3}. \tag{4.39}$$

Let us consider the asymptotic behavior of the system of differential equations (4.26) and (4.27) during the second stage of the spreading: According to the previous considerations and as it will be confirmed below in Fig. 4.5, during the second stage of the spreading/imbibition, velocity of the expansion of the droplet base, v_+, becomes small; therefore, the term corresponding to v_+ in the left hand side of Eq. (4.26) is excluded so as to understand the asymptotic behavior:

$$\frac{\mathrm{d}L}{\mathrm{d}t} = -\frac{2L\pi\Delta}{3}\frac{K_n}{V_0 - \pi\varepsilon\Delta\ell^2}\left[\frac{(1-n)p_c}{k(\ell^{1-n}-L^{1-n})}\right]^{1/n}, \tag{4.40}$$

while Eq. (4.27) is left unchanged. In order to solve analytically the system of differential Eqs. (4.27) and (4.40), Eq. (4.40) is divided by Eq. (4.27), which results in $\frac{dL}{d\ell} = -\frac{2\varepsilon\pi\Delta\, L\,\ell}{3\left(V_0 - \varepsilon\pi\Delta\ell^2\right)}$. If $V = V_0 - \varepsilon\pi\Delta\ell^2$ is used in place of ℓ, the latter equation is transformed into the following form: $\frac{dL}{dV} = \frac{L}{3V}$, which can be easily integrated and the solution is

$$V = C\,L^3 \tag{4.41}$$

where C is an integration constant. Let us rewrite Eq. (4.4) using the same dimensionless variables and $\bar{V} = V/V_0$:

$$\bar{V} = \frac{\pi L_m^3}{4V_0}\,\theta\,\bar{L}^3 \tag{4.42}$$

Comparison of Eqs. (4.41) and (4.42) demonstrates that the dynamic contact angle asymptotically remains constant during the second stage. This constant value is marked below as θ_f. It is necessary to emphasize that in the case under consideration the constancy of the contact angle during the second stage is not related to the contact angle hysteresis as there is no hysteresis in the system in the

case of complete wetting: θ_f is not a receding contact angle but it exists as a result of a self-regulation of the flow in the drop-porous layer system.[119]

4.2.2 Experimental data

All experimental data for the theoretical calculations were taken from the previous published papers,[116,118] where a series of experiments on blood spreading were reported. Blood of different haematocrit levels, 30 % and 50%, was prepared and a droplet of them with a known volume was deposited on different porous substrates: commercial untreated Whatman 903 filter paper, silanized Whatman 903 filter paper and nitrocellulose membranes of two different pore sizes 0.2 and 8 μm. The spreading experiments were performed to monitor time evolution of droplet height, h(t), radius of spreading, $L(t)$, dynamic contact angle, $\theta(t)$, and radius of the wetted spot, $\ell(t)$. Below a brief description of the experimental procedure is presented; however, the details can be found in Refs.[116,118].

4.2.2.1 Materials and instruments

Porcine blood was collected in EDTA anti-coagulated tubes (International Scientific Supplies Ltd. Bradford, UK) and treated to have different hematocrit levels. The blood samples of two different haematocrit levels, 30% and 50%, were prepared and used in the spreading experiments. Whatman 903 filter paper (blood saving card) and nitrate cellulose membranes of pore sizes 0.2 and 8 μm (marked by the supplier), both provided from GE health care (UK), were used as model porous substrates.

In addition, the experiments were also conducted on silanized Whatman 903 filter paper. In order to silanize the filter paper, it was dried for one hour at 140 °C and directly placed into a sealed dried temperature chamber with silicone gel to eliminate the effects of the humidity. APTES (3-aminopropyl-triethoxysilane) purchased from Sigma-Aldrich (UK) was poured into Petri dish and placed into the same temperature chamber at 25 °C for slowly evaporation to silanize the surface of fibers inside Whatman 903 filter paper. Each Whatman 903 paper was silanized for over 48 hours. The goal of silanization was to form organic silane layer on the

surface of cotton fibers which allows obtaining the porous substrates of the same porosity; however, with higher hydrophobicity.

The porosity of the Whatman 903 filter paper was in the range of 0.54 to 0.6 and the thickness was 500 ± 25μm measured by SEM. All samples used of nitrocellulose membranes were plane circles of radius 47mm and thickness in the range of 105-140 μm. The porosity of the membrane ranges between 0.66 and 0.84 as provided by the manufacturer.

AVT Pike F-032 high performance camera (Allied Vision Technologies, UK) was used at 60 frames per second for the top view recording of both porous substrates, nitrocellulose membranes and Whatman filter paper, as well as side view recording of blood spreading over nitrocellulose membrane. I-Speed high speed camera (Olympus, UK) was used for side view recording (600 frames per second) on Whatman 903 filter paper due to the very short duration of the spreading process (less than 0.5 second). The optical objective used in side view experiment for drop spreading was IF-3 standard (INFINITY PHOTO-OPTICAL GmbH, Germany). KRUSS DSA100 and drop shape analysis (KRUSS GmbH, UK) were used to determine the static advancing and static receding contact angles of blood droplets on all porous substrates in the case of partial wetting.

4.2.2.2 Spreading experiments

The experimental setup used for spreading experiments is shown in Fig. 4.4. The porous substrates were placed in the centre of the environmental chamber to control the temperature and humidity. Silicone gel was placed into the chamber to maintain constant humidity. The environmental chamber was mounted on a vibration-control stand to prevent vibrations. In each spreading experiment a constant value of blood droplet volume was produced (using 5.00± 0.25 μl syringe in the case of nitrocellulose membranes and 10.00 ± 0.5μl syringe in the case of silanized and untreated Whatman 903 filter papers) and placed on the porous substrates within less than 1mm dropping distant to ensure the consistency of each experimental measurement. The spreading process of blood drops over porous substrates was recorded and analysed using the top and side views.

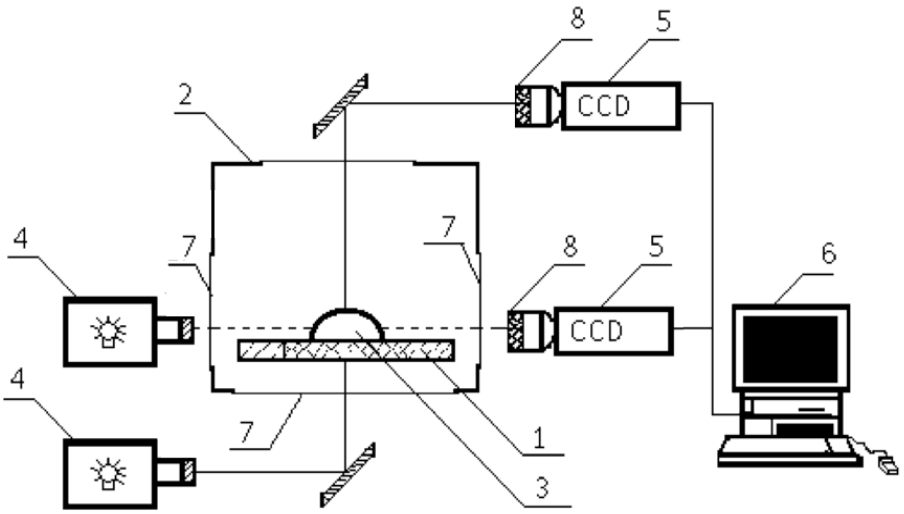

Figure 4.4: Schematic of the setup for spreading experiments: 1 - porous substrate; 2 - hermetically closed, thermostated chamber; 3 - liquid drop; 4 - light sources; 5 - CCD cameras; 6 - PC; 7 - optical windows; 8 - optical objectives. Reproduced with permission from Refs.[116,117]. Copyright © 2015, 2016 Elsevier B.V.

The time evolution of the spreading radius, $L(t)$, and the droplet height, $h(t)$, were monitored using side view camera. The time evolution of wetted region radius, $\ell(t)$, was recorded using top view camera. For each sample the camera recording started as the blood drop touched the porous surface and finished after the complete penetration of the droplet into the porous substrate. The time evolution of dynamic contact angle, $\theta(t)$, was calculated from the experimental results based on spherical shape assumption. Due to the thin thickness of porous substrate, the cross section of the porous substrate was assumed to be fully saturated as shown in Fig. 4.3. All experimental data for each porous substrate were averaged using at least ten repeated spreading experiments.

4.2.2.3 Blood rheology

The blood rheology measurements have been made in Ref.[118] using a rheometer with parallel plate geometry (4 cm diameter, stainless steel) and 250 μm gap. The range of shear rate was from 0.2 to 100 s^{-1}. The power law Otswald- de Waele relationship has been used as the rheological model of blood:

$$\mu = k\dot{\gamma}^{n-1}. \tag{4.43}$$

where k is the flow consistency index, n is the flow behaviour index and $\dot{\gamma}$ is the shear rate. Eq. (4.43) showed a good representation model for the measured blood viscosity as a function of shear rate,[118] where both k and n were fitted for all blood samples under investigation with different haematocrit levels. Table 4.1 shows the fitted values of k and n according to Eq. (4.43).

Table 4.1: Fitted values of k and n for different blood samples according to Eq. (4.43). Data taken from Ref.[118]

Haematocrit levels (%)	k	n
30	57.72	0.394
50	120.60	0.325

4.2.2.4 Measurements of the permeability and effective capillary pressure of porous substrate

In the developed theoretical model for the complete wetting case, the permeability, effective capillary pressure and porosity of porous layer can be considered as a single coefficient, $\frac{K_n p_c^{1/n}}{\varepsilon k^{1/n}}$, in the system of Eqs. (4.26) and (4.27). This coefficient was found from the permeability experiments based on the modified Darcy's law. The horizontal imbibition of blood samples with different haematocrit levels into the silanized and untreated Whatman 903 filter papers was investigated similar to Ref.[119] and the position of imbibition front was recorded by high speed camera over time. As is shown below (see results and discussion section) drop spreading/imbibition over nitrocellulose membranes is a partial wetting behavior; therefore, the coefficient was found only in the case of Whatman 903 filter papers. According to Eq. (4.17) and the modified Darcy's law the position of the imbibition front can be expressed as the following equation:[116,117]

$$d^{1+1/n}(t) = \frac{K_n p_c^{1/n}}{\varepsilon k^{1/n}}(1+1/n)\, t \tag{4.44}$$

where $d(t)$ is the position of the imbibition front inside the porous layer. The value of the coefficient, $\frac{K_n p_c^{1/n}}{\varepsilon k^{1/n}}$, can be determined by the slope of the straight line in the figure of $\frac{d^{1+1/n}(t)}{1+1/n}$ against t. The measured values of $\frac{K_n p_c^{1/n}}{\varepsilon k^{1/n}}$ are presented in Table 4.2 for both silanized and untreated Whatman 903 filter papers.

Table 4.2: The values of $\frac{K_n p_c^{1/n}}{\varepsilon k^{1/n}}$ for silanized and untreated Whatman 903 filter papers with different blood samples. Adapted with permission from Refs.[116,117]. Copyright © 2015, 2016 Elsevier B.V.

Haematocrit level (%)	$\frac{K_n p_c^{1/n}}{\varepsilon k^{1/n}}$ ($mm^{(1+1/n)}s^{-1}$)	
	silanized filter paper	untreated filter paper
30	117.15	43.33
50	30.184	27.01

4.2.3 Numerical solution of the system of differential equations (4.28) and (4.29)

In the developed mathematical model for complete wetting cases, the system of differential equations (4.28) and (4.29) was solved using initial conditions (4.31) and (4.32). The conditions (4.33) and (4.36) were used to determine the two unknown parameters, χ and υ. It should be noted that the system after that does not include any fitting parameters. As is shown in Table 4.3 both parameters, χ and υ, vary insignificantly for the n values used in the calculations.

Table 4.3: Calculated values of the two unknown dimensionless parameters χ and υ for blood samples with different n values. Reproduced with permission from Ref.[117]. Copyright © 2015 Elsevier B.V.

Haematocrit level (%)	n	υ	χ
30	0.394	0.281	0.376047
50	0.325	0.214	0.3454006

Therefore, the three dimensionless dependencies $\bar{L}(\bar{t})$, $\bar{\ell}(\bar{t})$ and θ/θ_m should fall on three almost universal curves. See solid lines in Figs. 4.6, 4.7 and 4.8. The predicted results are in good agreement with the experimental observations (see below): experimental dependencies also show a universal behavior.

4.3 Results and discussion

In all spreading experiments[116,117] with both Whatman 903 filter papers and nitrocellulose membranes, the droplets shape remained a spherical cap over the entire duration of spreading/imbibition process which satisfies the above theoretical assumption. This spherical cap shape allowed calculating the dynamic contact angle of each spreading droplet using the droplet base radius and height according to well-known equations.[118]

4.3.1 Complete wetting

The results of experiments presented in Refs[116,117] indicated that the blood droplets spreading/imbibition on both untreated and silanized Whatman 903 filter papers was a complete wetting. The silanization of filter paper resulted in a considerable increase in the dynamic contact angle, but the spreading behaviour still remained complete wetting. Although there were some differences in the spreading behavior of blood samples with different haematocrit levels on filter papers, in general, the spreading/imbibition results of all samples showed similar features during the whole process. As shown earlier in Fig. 4.2 the whole process can be subdivided into two stages similar to the case of Newtonian liquids[119]: over the duration of the first stage, the expansion of droplet radius, due to the capillary regime of spreading, is faster

than the shrinkage, caused by the imbibition into the filter paper, until they counterbalance each other as the maximum radius is reached. After that the second stage starts in which the droplet base shrinks and the wetted region expands until the complete disappearance of the droplet (see below in Figs. 4.6-4.8).

Fig 4.5 shows dimensionless velocity $\bar{V}_+$ and $\bar{V}_-$ for blood samples with different haematocrit levels (*n* values) spreading in a complete wetting case calculated according to Eq. (4.37), and χ and υ values presented in Table 4.3. This figure confirms that in a complete wetting case:

a) First stage of spreading/imbibition is much shorter than the second stage. During the first stage the capillary spreading prevails over the drop base shrinkage caused by the liquid imbibition into the porous substrate;
b) Spreading of the droplet base over porous substrate almost stops after the first stage and the shrinkage of the droplet base is determined by the imbibition of the liquid from the drop into the porous substrate.

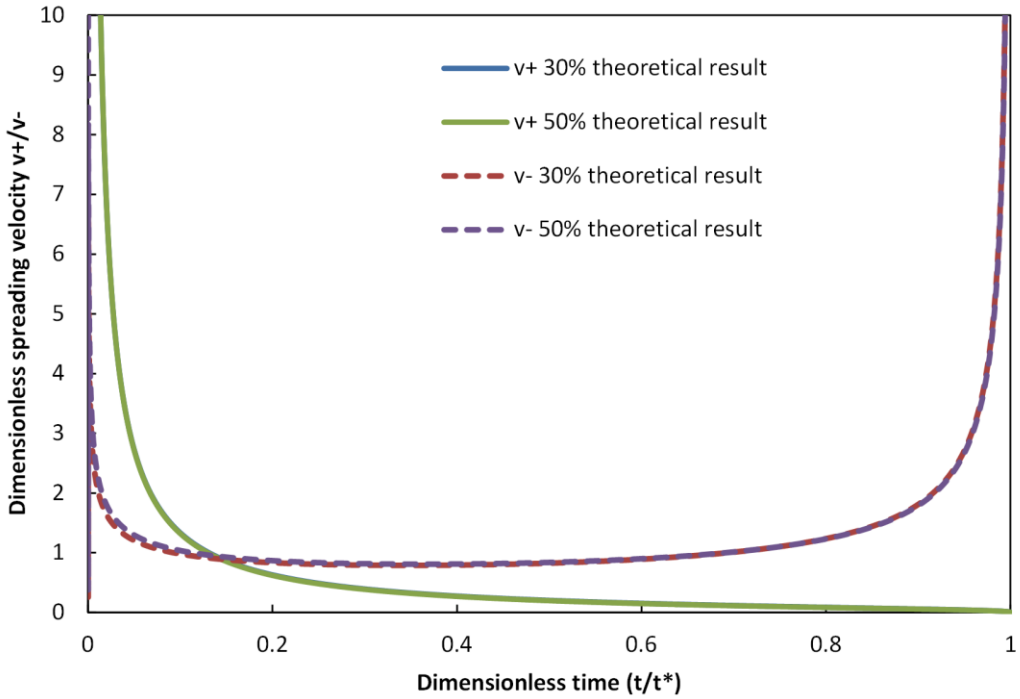

Figure 4.5: The time evolution of the dimensionless velocity $\bar{v}_+$ and $\bar{v}_-$ according to Eq. (4.37) for blood samples with 30% and 50% haematocrit level. Adapted with permission from Ref.[117] Copyright © 2015 Elsevier B.V.

Table 4.4 shows the experimental data obtained from spreading experiments over untreated and silanized Whatman 903 filter papers, which include the maximum spreading radius, $L_{m,\exp}$, contact angle at maximum spreading, $\theta_{m,\exp}$, maximum radius of wetted region, $\ell^*_{\exp}$ and the time of complete imbibition, $t^*_{\exp}$. Experimental time evolution of the radius of the droplet base, $L_{\exp}$, radius of the wetted region, $\ell_{\exp}$ and contact angle, θ_{exp} , were made dimensionless using the values presented in Table 4.4.

Table 4.4 indicates that the main difference between blood spreading over the silanized and untreated filter papers is the value of contact angle, θ_m, which is affected by the silanization (hydrophobization) of the filter paper and it is substantially higher in the case of silanized filter paper in comparison with the untreated one.

Table 4.4: The experiment data of spreading over silanized and untreated Whatman 903 filter paper to make experimental dependences dimensionless for comparison with predicted time dependences according to Eqs. (4.28), (4.29) and (4.39). Adapted with permission from Refs.[116,117]. Copyright © 2015, 2016 Elsevier B.V.

Type of filter paper	Haematocrit level (%)	$t^*_{\exp}$ (s) Time of complete imbibition	$L_{m,\exp}$ (mm) Max radius of droplet base	$\theta_{m,\exp}$ (degree) Contact angle at t_m	$\ell^*_{\exp}$ (mm) Max radius of wetted region
silanized	30	0.226 ±0.032	2.00 ±0.15	40.45 ±3.57	2.97 ±0.07
	50	0.438 ±0.021	2.13 ±0.21	39.4 ±7.6	2.94 ±0.03
untreated	30	0.351 ±0.014	2.18 ±0.07	32.80 ±1.88	3.36 ±0.09
	50	0.508 ±0.022	2.18 ±0.08	30.94 ±2.50	3.32 ±0.06

Figs. 4.6-4.8 compare the experimental data with the predicted results according to Eqs. (4.28), (4.29) and (4.39) for complete wetting cases. These figures show that all the data fall into corresponding universal curves when the dimensionless values are used: L/L_m, ℓ/ℓ^*, t/t^*, and θ/θ_m. The predicted results for blood droplets with different values of *n* are in a good agreement with the experimental data. However, the main conclusion is that both experimental dependences and the calculated theoretical dependences show a remarkable universal behavior independent of *n.* As can be seen in Figs. 4.6-4.8, only two stages of speeding have been identified in the case of complete wetting: a relatively fast initial stage of spreading followed by a shrinkage of droplet base as a result of the droplet volume loss due to the imbibition into porous substrate.

It is necessary to consider that a simple model of blood rheology and its imbibition into the porous substrate is used in this chapter for complete wetting cases: The absorption of red blood cells inside the porous substrate, bi-porous structure of the substrate,[118] and evaporation were not considered within the model.

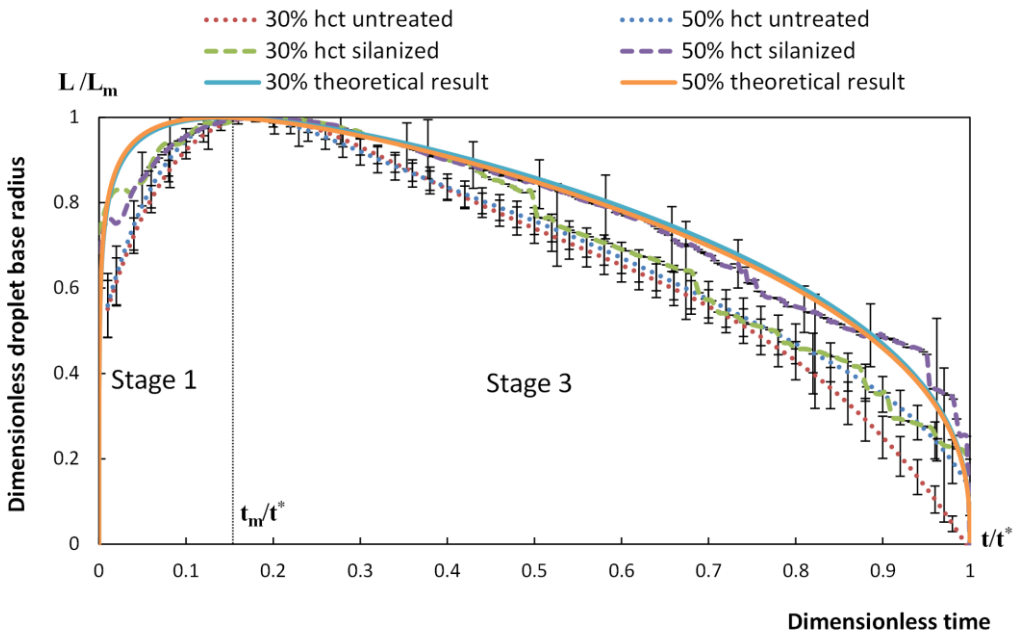

Figure 4.6: Dimensionless radius of the droplet base in the case of spreading over silanized and untreated Whatman 903 paper. Adapted with permission from Ref.[116] Copyright © 2015 Elsevier B.V.

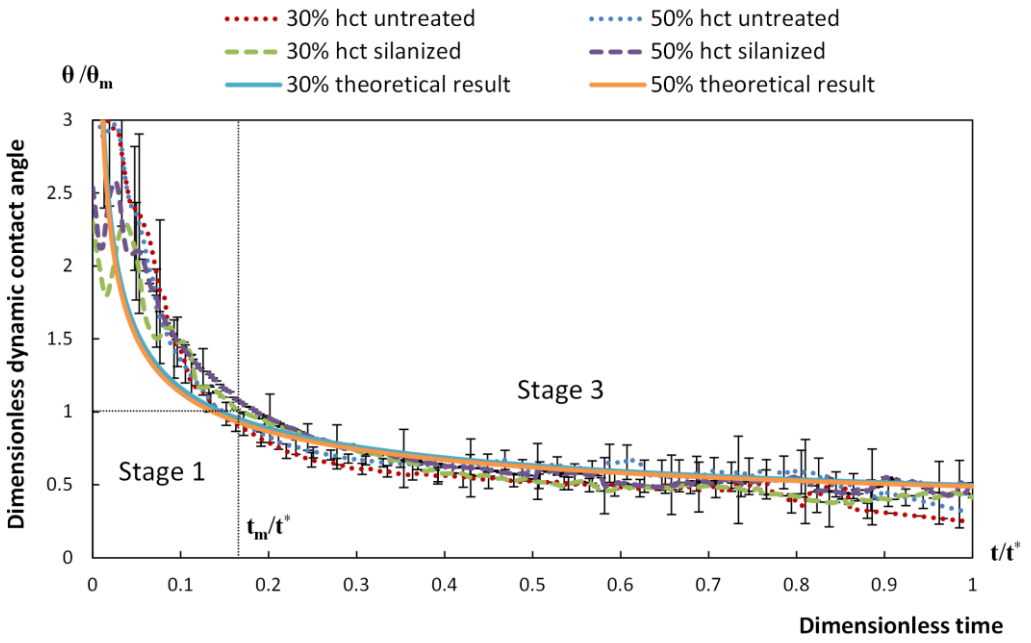

Figure 4.7: Dimensionless dynamic contact angle in the case of spreading over silanized and untreated Whatman 903 paper. Adapted with permission from Ref.[116] Copyright © 2015 Elsevier B.V.

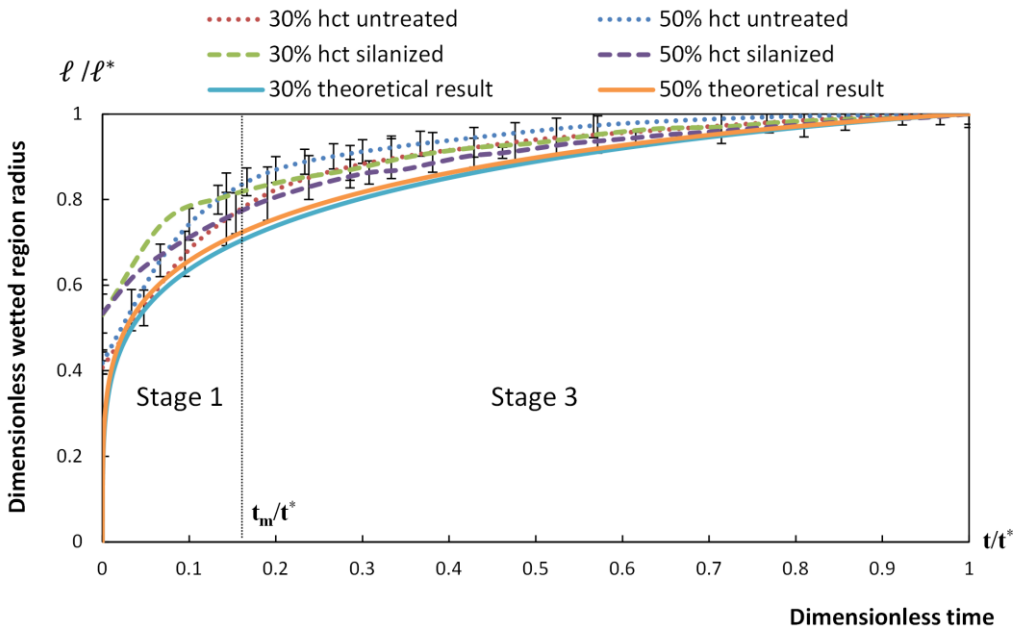

Figure 4.8: Dimensionless radius of the wetted region inside the filter paper in the case of spreading over silanized and untreated Whatman 903 paper. Adapted with permission from Ref.[116] Copyright © 2015 Elsevier B.V.

In order to predict completely the blood spreading/imbibition behavior in the case of complete wetting, the four experimental data, time of complete imbibition, t^*, maximum radius of droplet base, L_m, contact angle at maximum spreading, θ_m, and maximum radius of wetted region, ℓ^*, are determined from the theoretical results and physical parameters which are obtained independently from different experiments. These physical parameters are the viscosity of blood, $\mu = k\dot{\gamma}^{n-1}$, namely, n and k; the surface tension, γ and the physical parameters of porous substrate: the permeability coefficient, $K_n p_c^{1/n}$, the thickness, Δ, and the porosity, ε. The universal dimensionless constants, namely, υ, χ, $\bar{t}_m$ and $\bar{\ell}_m$ could be determined from the result of the dimensionless model.

The value ℓ^* can be determined directly according to Eq. (4.3), where the values of V_0, ε and Δ are equal to 10±0.5µl, 0.57 ± 0.03 and 500 ± 25 µm, respectively.[118] The imbibition time, t^*, can be obtained by $t^* = \upsilon\, t_p^*$, where t_p^* is determined by Eq. (4.25) and the measured values of $\frac{K_n p_c^{1/n}}{\varepsilon k^{1/n}}$ for silanized and untreated Whatman 903 filter papers in Table 4.2 .

Due to the fast expansion of the droplet base radius during the first stage of spreading, the imbibition of blood could be neglected in this stage; therefore, the maximum spreading radius can be approximately by Eq. (4.11) and then, the contact angle, θ_m can be calculated according to Eq. (4.38) as the following equations:

$$L_m = \left[\frac{n}{2n+1} \frac{\lambda}{\alpha_n} \left(\frac{\gamma}{k} \right)^{1/n} \frac{V_0^{(n+2)/n}}{(2\pi)^{(n+2)/n}} t^* (\bar{t}_m + \bar{t}_0) \right]^{\alpha_n} \tag{4.45}$$

$$\theta_m = \frac{4V_0}{\pi L_m^3} (1 - \bar{\ell}_m^2) \tag{4.46}$$

where $\gamma \cong 50 \pm 5$ dyne/cm and the values of the k and n for blood samples with different haematocrit levels are presented in Table 4.1.[118]

The calculated data for t^*_{sim}, $L_{m,sim}$, $\theta_{m,sim}$ and ℓ^*_{sim} based on the mathematical model and independent measurements of physical parameters are given in Table 4.5. The comparison of the simulated result and experimental data (Table 4.4) indicates that the calculated parameters are in a good agreement with the experimental observations.

Table 4.5: The predicted values of blood spreading/imbibition behavior over silanized and untreated Whatman 903 filter paper. Adapted with permission from Refs.[116,117]. Copyright © 2015, 2016 Elsevier B.V.

Type of filter paper	Haematocrit level (%)	t^*_{sim} (s) Time of complete imbibition	$L_{m,\text{ sim}}$ (mm) Max radius of droplet base	$\theta_{m,\text{ sim}}$ (degree) Contact angle at t_m	ℓ^*_{sim} (mm) Max radius of wetted region
silanized	30	0.172	1.954	51.14	3.344
	50	0.973	2.035	42.71	3.344
untreated	30	0.465	2.050	44.30	3.344
	50	1.087	2.044	42.13	3.344

4.3.2 Partial wetting

According to Ref.[116] the blood droplets spreading/imbibition on nitrocellulose membranes shows a partial wetting behaviour. The whole process can be subdivided into three stages, as shown earlier in Fig. 4.1, which is a characteristic feature of the partial wetting case (see Figs. 4.9-4.11). During the fast first stage drop spreads until its base radius reaches the maximum value, L_{ad},; after that the second stage starts in which the three-phase contact line is pinned on the substrate at the maximum position and the contact angle decreases from static advancing contact angle, θ_{ad}, to static receding contact angle, θ_r ; and finally, during the third stage the droplet base radius starts to shrink at approximately constant contact angle equal to the static receding contact angle until the complete imbibition of the droplet (see Fig. 4.10). Therefore, blood drop spreading/imbibition over nitrocellulose membranes was a partial wetting process.

In order to compare the spreading behaviour of blood on different nitrocellulose membranes, the following dimensionless parameters were used: $\bar{L} = L(t)/L_{ad}$, $\bar{\ell} = \ell(t)/\ell^*$, $\bar{\theta} = \theta(t)/\theta_{ad}$ and $\bar{t} = t/t*$, where L_{ad} is the maximum radius of droplet base, ℓ^* is the radius of wetted region at the end of the process, θ_{ad} is the

advancing contact angle, t^* is the time when imbibition is finished (see Fig. 4.1). All corresponding parameters are presented in Table 4.6.

In Figs. 4.9-4.11, time evolution of the dimensionless radius of the droplet base, dynamic contact angle and radius of the wetted area is presented in the case of partial wetting. A corresponding universal behaviour independent of bloods with different haematocrit level and *n* values is also clear here for different nitrocellulose membranes. As mentioned earlier, the whole spreading process on nitrocellulose membranes can be subdivided into three stages. However, note that in the case of spreading over 0.2 μm pore size nitrocellulose membranes the red blood cells did not penetrate inside the membrane pores and only plasma could penetrate inside. That is, the final radius of the droplet base did not vanish (see Fig. 4.9) and only stages 1 and 2 are present in this case.

Table 4.6: The experiment data of spreading over nitrocellulose membranes to make experimental dependences dimensionless. Adapted with permission from Ref.[116]. Copyright © 2016 Elsevier B.V.

Pore size of membrane (μm)	Haem atocrit level (%)	t^* (s) Time of end of spreading process	t_{ad} (s) Time of reaching max radius	L_{ad} (mm) Max radius of droplet base	θ_{ad} (degree) Advancing contact angle	θ_r (degree) Receding contact angle	ℓ^* (mm) Max radius of wetted region
0.2	30	49.2	11.733	1.97 ±0.04	44.03 ±0.9	22.60 ±1.53	3.07
	50	52.2	19.933	2.16 ±0.04	45.84 ±2.4	24.21 ±3.50	2.6
8.0	30	21.2 ±1.9	0.866	1.99 ±0.07	39.82 ±0.517	15.58 ±4.09	3.88
	50	182.3 ±13.3	8.466	1.88 ±0.06	39.10 ±0.44	17.10 ±5.10	3.32

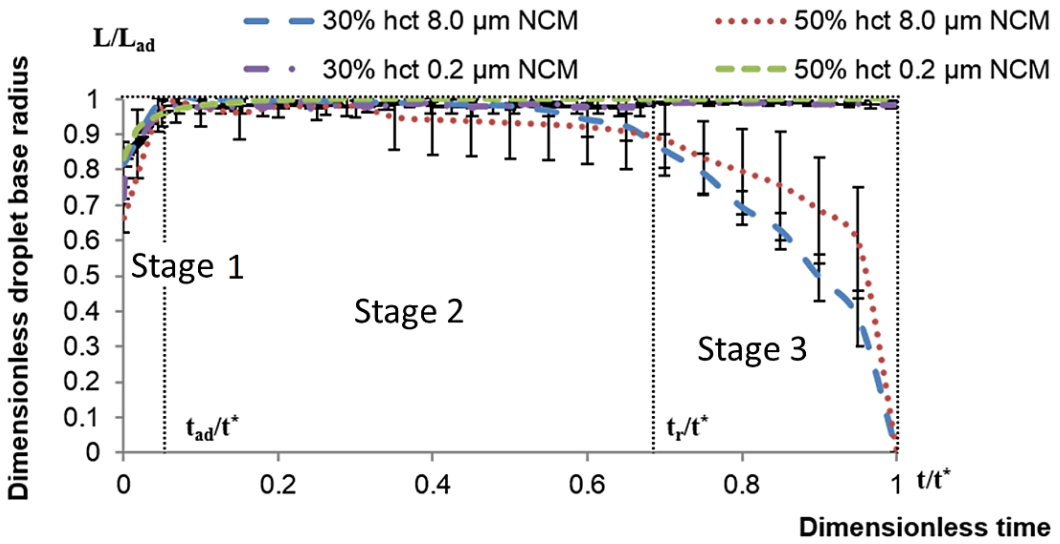

Figure 4.9: Dimensionless radius of the droplet base in the case of spreading over nitrocellulose membrane. In the case of 0.2 µm NCM, only stage 1 and 2 are present. Reproduced with permission from Ref.[116]. Copyright © 2016 Elsevier B.V.

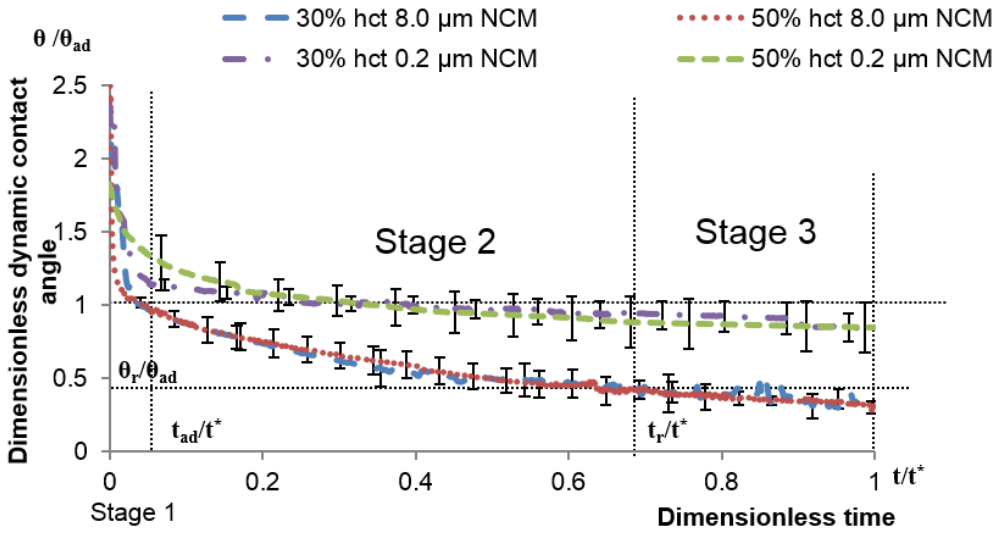

Figure 4.10: Dimensionless dynamic contact angle in the case of spreading over nitrocellulose membrane. Note, in the case of 0.2 µm NCM, there is no stage 3, it is a continuation of stage 2. The contact angle remained almost constant after stage 1. Reproduced with permission from Ref.[116]. Copyright © 2016 Elsevier B.V.

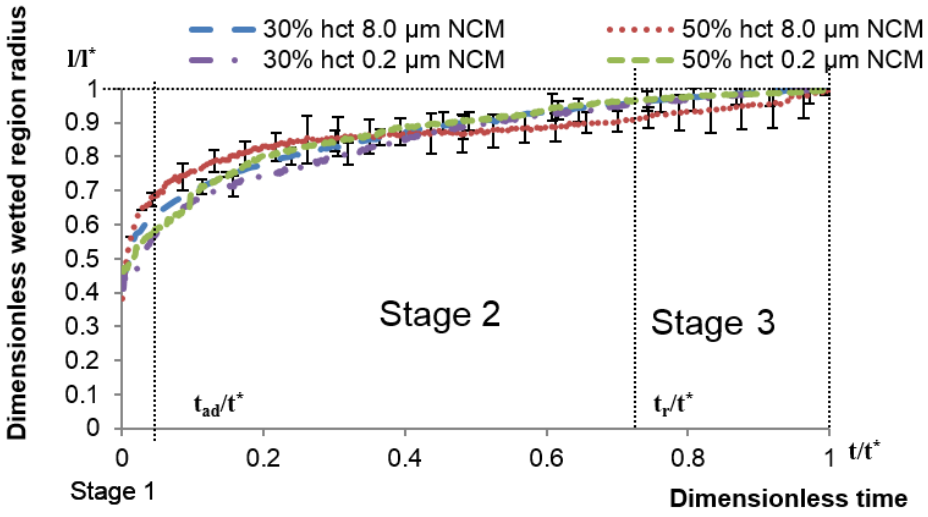

Figure 4.11: Dimensionless radius of the wetted area inside the membrane in the case of spreading over nitrocellulose membrane. Note, in the case of 0.2 µm NCM, stage 3 is only continuation of stage 2. Reproduced with permission from Ref.[116]. Copyright © 2016 Elsevier B.V.

4.4 Conclusions

Spreading/imbibition of small drops of blood, which is a non-Newtonian liquid, over different dry porous layers, is investigated from both theoretical and experimental points of view. A system of two differential equations is derived for the case of complete wetting from the combination of a spherical cap spreading model over porous layer and a modified Darcy's law for power law fluids. The deduced system of differential equations describes the time evolution of radii of both the drop base and the wetted region inside the porous layer during blood spreading/ imbibition over a dry porous substrate. The developed mathematical model does not include any fitting parameters and predicts a universal behavior for the dimensionless dependences of the droplet base radius, the radius of wetted region, and the contact angle of droplet over porous substrate, which are completely independent of the rheological properties of blood. The results of experiments indicated that the blood droplets spreading/imbibition on both untreated and silanized Whatman 903 filter papers was a complete wetting behaviour with two subsequent stages: initial fast spreading and the shrinkage of the drop base. However, in the case of nitrocellulose membranes a partial wetting behaviour with three subsequent stages: initial fast spreading, constant maximum droplet base and the shrinkage of the drop base, was

observed. All experimental data fell on three universal curves independent of bloods with different haematocrit levels and *n* values if appropriate scales are used with a plot of the dimensionless droplet base radius, the wetted region radius, and the contact angle of droplet over porous layers. The predicted theoretical results for complete wetting cases are also three universal curves accounting quite satisfactory for the experimental data. The simulated results show a good agreement with experiment data although the bi-porous structure of the filter paper and adsorption of red blood cells inside the porous substrate were not taken into account according to the suggested model.

Nomenclature 4

a^*	characteristic scale of the pore radii inside the porous layer, m
A	dimensionless parameter defined in Eq. (4.30)
b, *c*, C	integration constants
d	position of the imbibition front inside the porous layer, m
g	gravity acceleration value, $m \cdot s^{-2}$
h	height of the drop, m
h^*	scale of the drop height, m
$K_{n,p}$	permeability of the porous layer, $m^{1+1/n}$
k	flow consistency index, $Pa \cdot s^n$
L	radius of the drop base, m
L_{ad}	maximum value of the drop base radius in a partial wetting, m
L_m	maximum value of the drop base radius in a complete wetting, m
L_0	radius of the drop base in the end of the very fast initial stage of spreading, m
L^*	scale of the drop base, m
ℓ	radius of the wetted region inside the porous layer, m
ℓ_m	radius of wetting region at time instant t_m, m
ℓ^*	maximum radius of the wetted region inside the porous layer, m
n	flow behavior index
p	pressure, Pa
p_c	capillary pressure inside the porous layer, Pa

p_d	capillary pressure inside the drop, Pa
p_g	ambient pressure, Pa
Q	flow rate, $m^3.s^{-1}$
r, x, z	co-ordinate system
R	Radius of tube, m
t	time, s
t_{ad}	time when θ_{ad} is reached in a partial wetting, s
t_m	time of maximum spreading radius in a complete wetting, s
t_r	time when θ_r is reached in a partial wetting, s
t_Δ	time required for a complete saturation of the porous layer, s
t_0	duration of the very fast initial stage of spreading, when the capillary regime of spreading is not applicable, s
t^*	time when imbibition is finished in partial and complete wetting, s
t^*_p	time scale of imbibition into the porous layer, s
t^*_μ	time scales of viscous spreading over porous layer, s
T_p	time of the slower imbibition into the porous substrate, s
T_μ	time of the fast viscous spreading over porous layer, s
u, v	vertical and radial velocity components, $m.s^{-1}$
v_+	velocities of the expansion of the drop base, $m.s^{-1}$
v_-	velocities of the shrinkage of the drop base, $m.s^{-1}$
V	volume of the drop, l
V_0	initial volume of the drop, l

Greek symbol

α_n	dimensionless parameter defined as $n/(3n+7)$
γ	surface tension, $N.m^{-1}$
$\dot{\gamma}$	shear rate, s^{-1}
ε	porosity of the porous layer
Δ	thickness of the porous layer, m
δ	smallness parameter
μ	effective viscosity, Pa.s
θ	dynamic contact angle, degree
θ_{ad}	static advancing contact angle in a partial wetting, degree

θ_f constant contact angle during the second stage of complete wetting, degree

θ_m contact angle at t_m in a complete wetting, degree

θ_r static receding contact angle in partial wetting, degree

υ dimensionless parameter in Eqs. (4.28) and (4.29)

ρ density, $kg \cdot m^{-3}$

λ effective lubrication parameter

χ dimensionless parameter in Eqs. (4.28) and (4.29)

Appendix 4.A

A radial velocity profile for flow of a power law liquid in a pipe is given by the following expression:[121]

$$u(r) = \frac{n}{n+1}\left(\left|\frac{dp}{dx}\right|\frac{1}{2k}\right)^{1/n}\left(R^{1+1/n} - r^{1+1/n}\right). \quad (4A.1)$$

Everywhere below it is assumed that the flow is directed along *x*.

Therefore, the flow rate, Q, is:

$$Q = \pi\frac{n}{3n+1}\left(\left|\frac{dp}{dx}\right|\frac{1}{2k}\right)^{1/n} R^{3+1/n}. \quad (4A.2)$$

According to the latter equation the average velocity of flow, *v*, in the pipe can be found as:

$$v = \frac{Q}{\pi R^2} = \frac{n}{3n+1}\left(\left|\frac{dp}{dx}\right|\frac{1}{2k}\right)^{1/n} R^{1+1/n}. \quad (4A.3)$$

Capillary imbibition of non-Newtonian liquid into a thin capillary

The schematic of capillary imbibition of a non-Newtonian liquid, like blood, into a thin capillary is shown in Fig. 4A.1.

Figure 4A.1: Capillary imbibition of a non-Newtonian liquid into a thin capillary.

The rate of the imbibition can be written according to Eq. (4A.3):

$$\frac{d\ell}{dt} = v = \frac{n}{3n+1}\left(\frac{dp}{dx}\frac{1}{2k}\right)^{1/n} R^{1+1/n}. \tag{4A.4}$$

The gradient of the pressure is equal to, capillary pressures/ℓ:

$$\frac{dp}{dx} = \frac{\gamma \cos\theta / R}{\ell}, \tag{4A.5}$$

where γ is the liquid-air interfacial tension and θ is the contact angle. Substitution of Eq. (4A.5) into Eq. (4A.4) results in

$$\frac{d\ell}{dt} = \frac{n}{3n+1}\left(\frac{\gamma \cos\theta}{\ell}\frac{1}{2k}\right)^{1/n} R, \tag{4A.6}$$

or

$$\ell^{1/n}\frac{d\ell}{dt} = \frac{n}{3n+1}\left(\frac{\gamma \cos\theta}{2k}\right)^{1/n} R, \quad \ell(0) = 0. \tag{4A.7}$$

Integration of the latter expression with the initial condition gives

$$\ell(t) = \left(\frac{nR}{3n+1}\right)^{\frac{n}{n+1}}\left(\frac{\gamma \cos\theta}{2k}\right)^{\frac{1}{n+1}} t^{\frac{n}{n+1}}. \tag{4A.8}$$

Eq. (4A.8) leads to the well-known Washburn solution in the case of a Newtonian liquid, n=1:

$$\ell(t) = \left(\frac{R}{4}\right)^{\frac{1}{2}}\left(\frac{\gamma \cos\theta}{2\mu}\right)^{\frac{1}{2}} t^{\frac{1}{2}}. \tag{4A.9}$$

Comparison of the Eqs. (4A.8) and (4A.9) demonstrate that pseudoplastic fluids (n<1) penetrate into thin capillaries slower than Newtonian liquids, while dilatant fluids (n>1) penetrate faster than Newtonian fluids. It is easy to confirm that the

same conclusion is also valid for the imbibition of non-Newtonian liquids into a porous medium.

One dimensional imbibition of a non-Newtonian liquid into a porous medium

In the case of one dimensional imbibition of a non-Newtonian liquid into a porous medium, Eq. (4A.3) can be rewritten as follows

$$v = K_n \left(\left| \frac{dp}{dx} \right| \frac{1}{k} \right)^{1/n}, \tag{4A.10}$$

where K_n is the permeability of the porous medium for the power law non-Newtonian liquid of power n. In the case of Newtonian liquid the well-known Darcy's law can be recovered from the above equation:

$$v = \frac{K_p}{\mu} \frac{dp}{dx}. \tag{4A.11}$$

CHAPTER 5

KINETICS OF SPREADING OF NON-NEWTONIAN SOLUTIONS OVER HAIR

Overview

In the previous chapter theoretical and experimental findings on kinetics of wetting and spreading of blood as a non-Newtonian colloidal suspension over different thin porous substrates were presented. Below wetting and spreading of two commercially available non-Newtonian polymeric solutions, Aculyn™ 22 and Aculyn™ 33, on hair tresses are investigated experimentally[1]. The results of investigations were published earlier in *Colloids and Interface Science Communications* 9, 12-15, 2015 and reused in this chapter with permission. Initially in this chapter, a description of the material preparation and experimental procedure of wetting of hair tresses with different solutions is explained. Then, bulk and surface properties of the solutions along with the behaviour of the solutions' droplets on dry hair tresses are studied. Spreading kinetics of the droplets is analysed, including wetting, spreading and penetration, as well as the influence of several additives common in cosmetic formulations.

5.1 Introduction

In this chapter wetting and spreading of non-Newtonian polymeric droplets on hair tresses are presented. Hair wetting is a very common phenomenon in our everyday life. Interactions between hair and water occur frequently not only in shower during application of the hair care products such as shampoos, conditioners or hair colorants, but also in contact with the atmospheric moisture. Water can absorb and penetrate into hair making it wet. As a result, the wetted strands stick to each other and form several clumps due to cohesive forces caused by water bridges.[122] Hair

[1] Statement of contributions of joint authorship: The experiments presented in this chapter were conducted by Anna Trybala. Omid Arjmandi-Tash analysed the experimental data and interpreted the findings.

wettability, and how hair care products affect its wetting properties, is of considerable interest in cosmetic science.[123,124] It is important to realise that behaviour of hair care products is different when they are applied on wet or dry hair; generally, wetting should be studied in the conditions which can mimic real applications.

The majority of research presented in the literature concentrate on interaction of a single hair fibre (dry or wet) with various liquids;[124-126] however, wetting of dry hair tresses with polymer solutions is largely unexplored up to now. These properties, however, attract significant interest from the industry, particularly for treatments which are applied on dry hair, e.g. for hair colouring products, hair styling products, leave-on conditioners and serums. Moreover, there is a desire to minimise the use of harsh surfactant in such systems; cosmetic polymers with a pronounced affinity to interfaces, like Aculyn™ 22 (A22) and Aculyn™ 33 (A33) solutions, are such alternatives. These polymers are widely used in production of shampoos, bath foams, foaming facial cleansers, hair styling gels, liquid soaps, lotions, moisturizing creams and hair colorants.[4] Below wetting of dry hair tresses by polymer solutions of A22 and A33 is investigated to determine behaviour of polymeric solutions during real cosmetics applications.

Hair is a natural fibre consisting of a core (cortex and medulla) covered with overlapping cuticle cells. The most important for wetting is the outer surface of the cuticle, which is covered by a covalently attached monolayer of fatty acid (18-methyle-icosanic acid), thus making the fibre slightly hydrophobic.[127-129]

5.2 Materials and methods

As mentioned above, the experiments were conducted using two polyacrylate polymers, A22 and A33, which are broadly applied by hair care industries. A22 is a hydrophobically-modified anionic alkali soluble polymeric emulsion, and A33 is an anionic alkali soluble, lightly crosslinked emulsion of the ethyl acrylate and methacrylic acid.[130,131] General structures of the polymers are presented in Fig. 5.1.

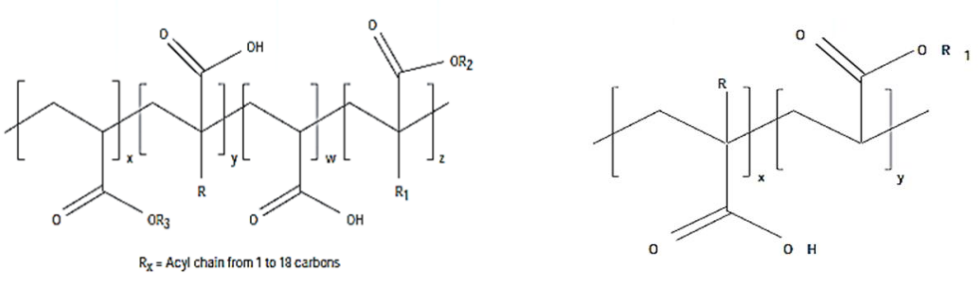

a) b)

Figure 5.1: Schematic structure of a) Aculyn™ 22 and b) Aculyn™ 33.[130, 131]

Aqueous solutions of these polymers are viscous, shear thinning non-Newtonian fluids.[132,133] Both polymer emulsions may contain a trace amount of surfactant (sodium dodecyl sulphate); therefore, some low level of surfactant was expected in the experiments; the surfactant effect was separately investigated in this work. Polymers were used without any pre-processing, like purification to keep condition of the experiments as close to the real application conditions as possible. A22 and A33 emulsions were 30 % w/w and 28 % w/w active in water, respectively, and they were supplied by Dow. The polymers were soluble in water at high pH (>7).[130,131]

Aqueous solutions of the polymers in the concentration range 1.0 – 1.5% w/w were prepared by diluting and neutralising the stock polymer emulsions with a 2 % ammonia solution in ultra-pure water produced by Millipore Q, and further buffered with ascorbic and citric acids (0.2 % w/w each). Sodium chloride (NaCl) was added to the solutions in the range 0-1.5 M, and iso-propyl alcohol (i-propanol, ipr-OH) was used at 0 or 1.67 M (10% w/w) concentration. Sodium dodecyl sulphate surfactant (SDS) was used at the concentration 5 mM. The above compositions have been chosen to represent typical systems used in the cosmetic applications where the polymers are utilized, for example in hair colorant applications. In such systems, salt is often used to control the ionic strength and rheology, and solvents like i-propanol are added to control solubility of the active ingredients (such as dyes). Surfactant is typically used to enhance wetting properties and, in some cases, to produce a good quality foam. In the researches presented in this chapter and in Refs.[132,133] the procedure adapted by Procter & Gamble Company to produce cosmetics formulations was followed.

Rheology and surface tension measurements were conducted as described in Refs.[132,133]. Rheology measurements were conducted on an AR 1000-N rheometer (TA Instruments), using a steel cone of 4 cm diameter, cone angle 1˚59’ and

truncation of 56 μm. The temperature was kept constant at 20 ^{O}C using the Peltier plate. The relative standard error of rheology measurements when the samples were taken from the same solution was below 5 %; the error increased for the solutions prepared at different times, and was estimated at around 10%; this was attributed to variations in the solution preparation and polymer neutralization. Measurements on the surface tension were performed by the drop shape analyser DSA100 (Kruss), using a buoyant air bubble formed at the tip of the hooked capillary immersed in the cuvette containing a polymer solution.

Blended human hair tresses (brown, Caucasian origin) were supplied by International Hair Importers, arranged into flat tresses of 12 cm length, width 2.5 cm and approximately 3 mm thickness. The average weight of the hair tress was 2g and the average number of hair fibres in the tress was 4000. For wetting measurements, the tresses were secured in a special frame to provide as much hair alignment as possible. Frame allows fixing bunch of hair in a way which enables measurement of contact angle on hair. The surface of hair tress was as flat as possible. Example of hair arrangement and SEM images of hair fibres are presented in Fig. 5.2.

a)

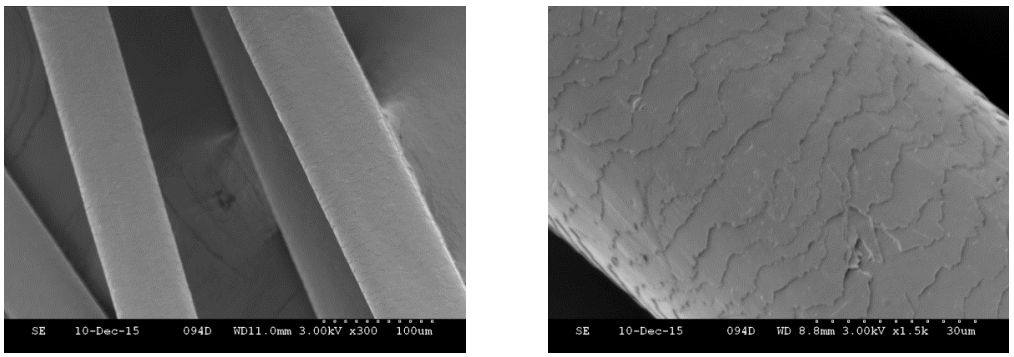

b)

Figure 5.2: a) Example of hair tress used for contact angle measurements; b) SEM images of hair fibers. Reproduced with permission from Ref.[134]. Copyright © 2015 Elsevier B.V.

The thickness of the tress was sufficient to avoid contact of the investigated liquid with the frame material. There was some expected variation in the arrangement of individual hair fibre on the frame in the course of repeated experiments, leading to a considerable standard error of measurements.

Each hair tress was washed by a neutral shampoo, rinsed 3 times in distilled water and dried naturally. Measurements of the apparent contact angle were performed on dry hair tresses using the drop shape analysing software DSA 3, KRUSS. This software provides the contact angles θ, the droplet volume V, and the droplet base diameter DB, all as a function of time t. The movies were recorded with a constant speed of 5 fps. The process time reported below is defined as the time during which the droplet remains on the hair tress. During this time various parallel processes (spreading, penetration and evaporation) occur. The initial contact angle was measured immediately after a droplet was placed on the support material. The final (advancing) contact angle is the contact angle after spreading stops, when the DB reaches a constant value. All measurements were made at 20^{o}C and 40% relative humidity. Teflonated silicon wafers (Teflon below) were selected as a reference support material for the contact angle measurements, as the initial contact angle on Teflon and hair tresses (both hydrophobic) is similar. In present experiments, the droplet volume was 2-3 μl for each measurement. However, different droplet volumes resulted in different base diameters, but the differences were compensated in the equipment software by converting the base diameter into the equivalent volume.

In the case of measurements on Teflon, reproducibility was very good, and the relative standard error was around 2-3%. When measuring on hair tresses, at least 10 repeated measurements were performed, however, the error was still in the range of 10 - 20 % due to variations in the tress arrangement on the frame, as mentioned above.

5.3 Results and discussion

5.3.1 Bulk and surface properties of the polymer solutions

Rheological and surface properties of the solutions under investigation are shown in Table 5.1. Data presented in Table 5.1 show that both polymers reduce surface tension, and the surface tension of the A33 solutions is lower than that of the A22 solutions. According to[132, 133] both A22 and A33 solutions demonstrate well pronounced shear thinning behaviours. Viscosity is presented at shear rate 12 s^{-1} because this particular shear rate is of industrial interest. Viscosity decreases considerably with increase in the salt concentration, and remains always higher for the A22 solutions of comparable concentration vs. the A33 solutions.

Table 5.1: Comparison of Bulk viscosity, surface tension and wetting properties of investigated solutions on hair tresses. Reproduced with permission from Ref.[134]. Copyright © 2015 Elsevier B.V.

Solution	Surface tension (mN/m)	Bulk viscosity at 12 s^{-1} (mPa.s)	Initial contact angle (deg)	Spreading time (s)	Final contact angle (deg)	Process time (s)
Water		1	100	5-10	90	---
A22 1% 0.3M NaCl	42±1	550±10	100	10-20	80	2000
A22 1% 0.3M NaCl 10% ipr-OH	36±1	400±7	80	1-4	60	2400
A22 1% 0.3M NaCl 5mM SDS	35±1	510±15	90	40-50	50	2000
A22 1% 1.3M NaCl	38±1	100±5	100	10-20	80	2000
A22 1% 1.3M NaCl 10% ipr-OH	32±1	40±5	0	immediate penetration		
A33 1% 0M NaCl	30±1	100±10	100	5-25	60	200
A33 1% 0M NaCl 10% ipr-OH	33±1	100±10	90	1-5	30	10
A33 1% 0M NaCl 5mM SDS	32±1	108±10	90	1-5	30	10
A33 1.5% 0M NaCl	27±1	500±50	100	10-30	60	100
A33 1.5% 0M NaCl 10% ipr-OH	30±1	500±50	90	2-3	50	60
A33 1.5% 0M NaCl 5mM SDS	35±1	560±10	80	1-8	25	70
A22:A33=1:1	---	90±10	100	25-80	65	180
A22:A33=1:3	---	40±10	100	10-40	50	140
A22:A33=3:1	---	400±15	100	40-50	60	2000

Addition of 10% i-propanol does not change substantially viscosity of the A33 solutions, but decreases viscosity of the A22 solutions (Table 5.1). The equilibrium surface tension slightly increases for the solutions of A33 with i-propanol; the opposite effect was observed with A22. The results presented in Table 5.1 confirms that the properties of A22 and A33 polymer solutions strongly depend on the composition, and even small changes could results in significant variations in their

bulk and surface properties. Comparison of the results with 10% i-propanol and 5 mM of SDS shows that viscosity of A33 is less sensitive to additives than A22. It is also important to stress that the polymer solutions are non-Newtonian shear thinning liquids, hence viscosity values presented in the Table 5.1 at a chosen shear rate are only indicative of the trends affecting their rheological behaviour across the broad range of shear rates.

5.3.2 Wetting properties of the polymer solutions

Table 5.1 presents comparison of the wetting properties: the initial contact angle, the final contact angle (contact angle after spreading), the spreading time and the process time for the investigated solutions.

Initial contact angle of water on Teflon is around 110^o, and on hair is around 100^o. It confirms the expected hydrophobic nature of the undamaged hair fibre as its primary component is keratin. However, hair tresses are a porous support. Even more than that, it has two-type porous structure: (i) pores built by an array of individual fibres (slightly different in each measurement) and (ii) a fine porous structure of each individual hair fibre (see Fig. 5.2(b)).[128] A hair tress demonstrates hydrophobic properties not only because of the hydrophobic nature of the hair surface, but also because of air pockets in between the fibres. That is, there are three possible wetting regimes: (a) Cassie wetting, where liquid is sitting on the hair tress, without penetration inside the tress, (b) Wenzel wetting, characterized by penetration of liquid into the hair tress, (c) transition from Cassie wetting to Wenzel wetting, after some critical contact angle is reached.[135-137] All three mentioned regimes were observed (see below).

Dynamic contact angle and diameter of the base line of the A22 polymer solution droplets on the hair tress is presented in Fig. 5.3. In the case of Teflon, the initial contact angle of all A22 solutions (1% polymer, 0.3M and 1.3M NaCl) was 110 ^{o}, and fast spreading over a short period of time, around 20 s, was observed. After the fast spreading stage the contact angle remained around 100 ^{o} and the droplet stayed on the support without changing its hemi-spherical shape. The initial contact angle on the hair tress for this polymer was about 100^o. Spreading stopped after 10-20 s, and the contact angle reached the value of 80^o (Fig. 5.3 and Table 5.1). The droplets remained on the surface of the hair tress after the initial fast spreading stage.

Following this stage the total process time (until the droplet complete disappearance) was around 2000 s for both solutions (A22 1% polymer, 0.3M and 1.3M NaCl). During this longer stage a slow evaporation and possible imbibition of the solutions into the hair were observed. Wetting properties of the solutions were very similar in spite of a considerable difference in their viscosities.

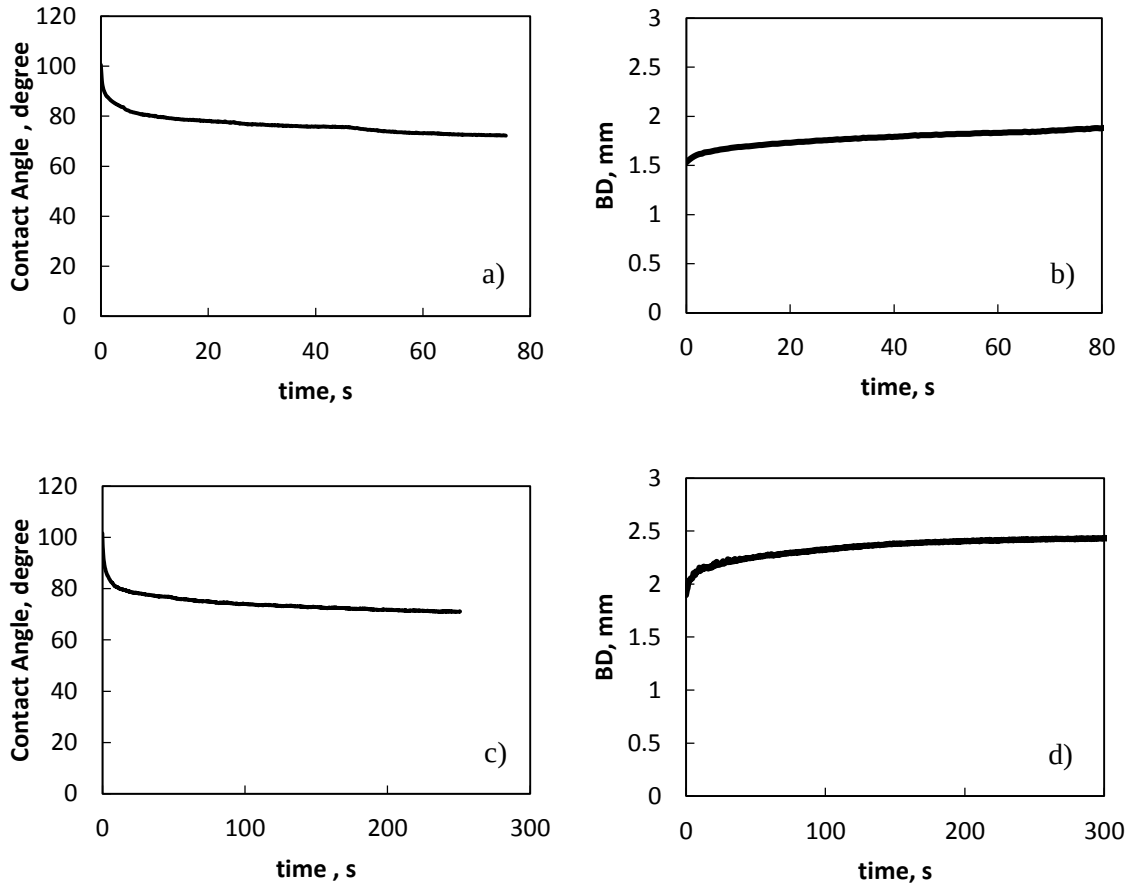

Figure 5.3: a) Contact angle and b) base line diameter of A22 1%, 0.3M NaCl solution on a hair tress; c) Contact angle and d) base line diameter of A22 1%, 1.3M NaCl solution on a hair tress. Partially reproduced with permission from Ref.[134]. Copyright © 2015 Elsevier B.V.

Characteristic droplet shape of the A22 solution on the hair tress is presented on the Fig. 5.4. Droplet remained on top of the tress after initial short time spreading. Droplet volume was decreasing with time due to evaporation and, possibly, slow penetration inside the hair tress.

t=0 s t=20 s t=197 s

Figure 5.4: Behaviour of pure A22 solutions on a hair tress.

Wetting properties of the A33 solutions on Teflon are similar to that of the A22 solutions. Initial contact angle of both A33 solutions (1% and 1.5% polymer, 0M NaCl) on Teflon was about 100 ^{o} and duration of the fast spreading stage was around 40-50 s (slightly longer than A22). The contact angle after spreading was around 80^{o}: the smaller contact angle in comparison with the A22 solutions is consistent with the lower surface tension of the A33 solutions (Table 5.1). The initial contact angle of the A33 solutions on the hair tress was about 100^{o}. For the A33 1% 0M NaCl the first fast stage of spreading was completed after 5-25 s. For the A33 1.5% 0M NaCl this stage took 10-30 s. In both cases the final contact angle after spreading was around 60^{o}. The total process time, during which the droplet disappeared completely, was 100 s for A33 1.5% 0M NaCl and 200 -250 s for A33 1% 0M NaCl (Table 5.1). It is important to notice that the droplet with higher viscosity disappeared faster. Contact angles and base line diameter of the A33 solutions vs. time on the hair tress are presented in Fig. 5.5; an example of the droplet shape change over time is illustrated in Fig. 5.6.

Fig. 5.5 shows that in the case of A33 solutions, where the contact angle reached the critical value (around 60^{o}), fast penetration into the hair tress was observed. This resulted in a "jump" on the graph of contact angle and diameter of the base line (Fig. 5.5). This can be explained by Cassie−Wenzel wetting transition: before reaching the critical contact angle (around 60^{o}) the droplet was in a Cassie state "sitting" on the outer surface of the hair tress; however, after the critical contact angle was reached then penetration of the liquid into the pores inside the porous media (like the hair tress in the case) by liquid started. Schematic penetration of the liquid inside the porous media (hair tress) is presented in Fig. 5.7. In the case of Cassie state, liquid wet only the outer layer of the hair tress; however, at the Wenzel state liquid penetrate inside the hair tress. Capillary transport along fibres started after the

transition. Such wetting transition is also observed on other keratin-built biological tissue, pigeon feathers, when it is irradiated by nitrogen and air plasma.[138]

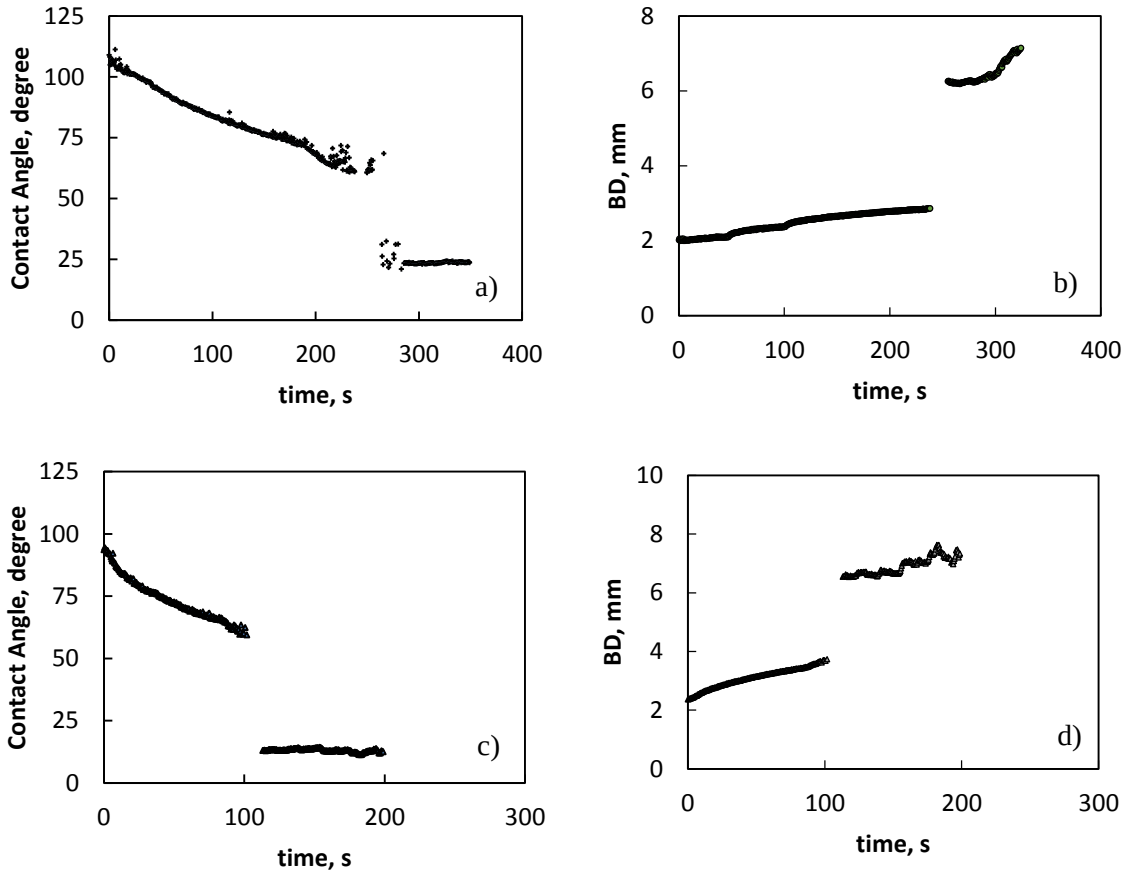

Figure 5.5: a) Contact angle and b) base line diameter of A33 1%, 0M NaCl solution on a hair tress; c) Contact angle and d) base line diameter of A33 1.5%, 0M NaCl solution on a hair tress. Partially reproduced with permission from Ref.[134]. Copyright © 2015 Elsevier B.V.

Figure 5.6: Behaviours of pure A33 solutions on a hair tress.

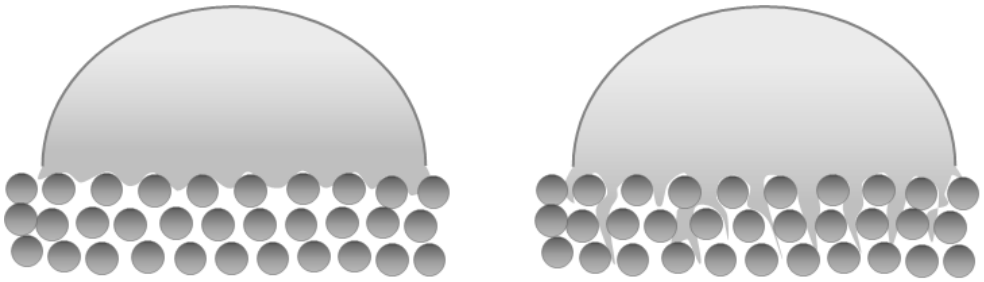

Cassie state **Wenzel state**

Figure 5.7: Behaviour of liquid droplet on a hair tress. Cassie state: only outer layer of the hair tress is wetted; Wenzel state: liquid penetrate dipper into the hair and penetrates along the hair tress. Reproduced with permission from Ref.[134]. Copyright © 2015 Elsevier B.V.

Figures 5.3 and 5.5 proves that the conditions for wetting transition is to reach the critical contact angle, which is around 60^{o} in the case under consideration. This condition is satisfied for the A33 solutions and not satisfied for the A22 solution, the latter showing higher contact angle. The critical value of contact angle was obtained faster for the A33 1.5% solution than that for the A33 1.0% solution. It can be caused by slightly higher concentration of the trace surfactant carried over from the stock emulsion with the higher concentration of the polymer. The decrease of the total process time for the A33 solutions with added SDS confirms this observation.

Differences in wetting behaviour of A22 and A33 solutions could be attributed to the presence of a yield stress for A22 solutions, which was reported in previous publications.[130,132] The presence of yield stress for a liquid can affect its spreading. It was shown earlier in Chapter 3 that equilibrium profile of a droplet over a substrate is determined by the action of surface forces. However, for a viscoplastic fluids with a considerable yield stress, the fluid yield stress may inhibit the spreading of drop, preventing the formation of drop shape governed by equilibrium conditions: contact angle cannot decrease to the equilibrium and it stays with a contact angle higher than equilibrium like an elastic solid. It was found earlier[132] that the A22 solutions demonstrate noticeable yield stress, decreasing with the increase of the NaCl concentration, and increasing with the increase in the polymer concentration. It could be a reason why A22 droplets remained on the surface of the hair tress after the initial fast spreading stage. However, A33 solutions which do not have any yield

point can spread and reach a critical contact angle and accordingly can show a fast penetration over hair tress.

In most cases droplets of the A33 solutions behaved as described above, that is, underwent Cassie-Wenzel transition; however, there were few cases when the droplets only spread on hair tress but did not reach the critical contact angle (60^o), and thus remained on the hair tress for a prolonged period of time. It could be caused by somewhat random arrangement of hair fibres on the surface of the tress (in spite of the forced alignment on the frame), and changed conditions favouring the Cassie−Wenzel wetting transition, which strongly depends on the roughness of the substrates and structure of the porous medium.[136,137] It confirms that in all experiments with hair tresses the hair arrangement plays a very important role.

The effect of i-propanol and SDS additives was also investigated (Table 5.1). Both solvents and surfactants are capable of changing both surface tension and bulk rheology of the polymer solutions. i-propanol and SDS were chosen as they are frequently used in cosmetics formulations. The initial contact angle of the A22 1% 0.3M 10% ipr-OH solution on the hair tress was around 80^o. In the case of the A22 1% 0.3M 10% ipr-OH, very fast spreading (1-4 s) was observed, and the final contact angle was around 60-50 ^{o}. The total process time was still long, though, around 2400 s. The solution showed better spreading on the hair tress than the solution without alcohol, but not better penetration. In the case of the A22 1% 1.3M 10% ipr-OH solution, the droplet penetrated into the hair tress immediately after deposition. It indicates that the initial contact angle was smaller than a critical value corresponding to the Cassie-Wenzel transition mentioned above, and the penetration occurred immediately. The initial contact angle of the solutions with alcohol was slightly smaller, and the total process time was shorter in comparison with the solutions without alcohol. In the case of the A33 1% 0M 10% ipr-OH, the initial contact angle on the hair tress was around 90^o, the spreading time was 1-5 s, the final contact angle was between 30^o- 20^o. The total process time was 10 s only. For the A33 1.5% 0M 10% ipr-OH solution, the initial contact angle on the hair tress was 90 ^{o}, but the final contact angle after 2-3 s spreading was 50^o and the total process time was 60 s.

The addition of 5mM SDS to the A22 1% 0.3M solution resulted in slightly different wetting properties on the hair (Table 5.1). The initial and final contact angles were lower (90 ^{o} and 50 ^{o}, respectively) than those for the solutions without SDS, and

spreading time was longer. The total process time was identical to that for the solutions without SDS. The most important influence of SDS addition on the A33 solutions was the decrease in the total process time. The initial contact angle of the A33 1% 0M NaCl 5mM SDS solution was around 90^{o}, and its spreading time was around 5 s. The total process time was 10 s. The initial contact angle of the A33 1.5% 0M NaCl 5mM SDS on hair tress was about 80 ^{o} and its total process time was 70 s. Similar to A22, wetting properties of the A33 solutions were improved by the addition of SDS. Thus, the addition of SDS and i-propanol to the polymers solutions improved their spreading on hair tress.

In addition, mixtures of the A22 and the A33 solutions with ratios A22:A33 1:1, 1:3 and 3:1 were investigated (Table 5.1). It was found that behaviour of the mixtures follows smoothly the changes in the polymer concentrations. For solutions with the higher content of A22, the droplet behaviour was similar to the pure A22 solutions, and vice versa. As before, no significant interactions between the two polymers in this concentration range were detected.

5.4 Conclusions

Wetting of multi-fiber hair tresses with solutions of two cosmetic polyacrylate polymers was investigated. The neutralized solutions of Aculyn 22^{TM} and Aculyn 33^{TM} polymers were studied in the concentration range 1.0 – 1.5 % w/w, with the bulk solution viscosity 40 – 500 mPa.s. The effect of common viscosity and surface tension modifiers, like sodium chloride, sodium dodecyl sulphate and i-propanol, was also investigated. The bulk viscosity of the solutions can be varied in a broad range by changing concentrations of the polymers or by adding salt, solvent or surfactant. It was found that the nature of the polymer, as well as its concentration and the concentration of additives, can be used to control wetting properties and hence the spreading kinetics on hair tresses. The solutions of both polymers spread on hair tresses. However, they show markedly different behaviour. For the A22 solutions, the droplet remains on the surface of the hair for almost half an hour, and only slow (if any) imbibition is observed. This behaviour could be related to the presence of a yield stress for A22 solutions. For the A33 solutions, the complete penetration/imbibition happens fast, after the contact angle reaches a critical value (around 60^{o}). This can be attributed to the so-called Cassie−Wenzel wetting

transition, when the liquid starts to penetrate inside the hair array. The conditions for this transition are more favourable for the A33 solutions in comparison to the A22. The total process time (time until droplet disappears) for the pure A33 solutions is much shorter than for the pure A22 solutions. In other words, the A33 solutions are readily absorbed by dry hair bulk, whereas the A22 solutions are absorbed very slowly if at all. Addition of a surfactant or a solvent (SDS and i-propanol in this study) can improve wetting properties of both polymers. In the case of the relatively low viscosity A22 solution (1% polymer, 1.3M NaCl, 100 mPa.s) addition of 10% i-propanol causes immediate imbibition of the solution into the hair. For a mixture of A22 and A33, the wetting properties follow behaviour of the polymer with the higher fraction.

CHAPTER 6

FREE DRAINAGE OF FOAMS PRODUCED FROM NON-NEWTONIAN SOLUTIONS

Overview

In the previous chapter the result of wetting and spreading of non-Newtonian polymeric droplets on hair tresses was presented. Below the free drainage of foams produced from those non-Newtonian polymeric solutions is investigated theoretically and experimentally. The results of investigations are in press in *Colloids and Surfaces A: Physicochemical and Engineering Aspects*, 2016 and reused in this chapter with permission. Initially in this chapter, a short description of the materials and experimental procedure with regards to the home-made foam generating apparatus is explained. Then a mathematical model along with appropriate boundary conditions and equilibrium profile is derived for the free drainage of non-Newtonian foams. In the next section, the predicted results for different foaming solutions are compared with the experimental data.

6.1 Introduction

In this chapter theoretical and experimental findings on free drainage of foams produced from non-Newtonian polymeric solutions is presented. Foams are conventionally stabilised by surfactants; however, polymers (polyelectrolytes) grow in popularity during the last decade as alternative stabilising additives to foaming solutions and they show increasing benefits in different industrial applications. For example, polymer enhanced foams are increasingly being utilised for reservoir recovery in petroleum industry.[139-141] Polymers are also used in firefighting foams on polar fuels to prevent the foam from collapse.[80] In addition, polymer stabilized hair colouring foams were recently patented in Ref.[4] to provide improvements in colour delivery.

Understanding the rate of foam drainage/liquid release from foam is of great importance in various industries because it shows the rate of delivery of active

components to the target places. Incorporating polymers into foaming solutions can affect the rate of drainage and thus, efficiency of the application. Addition of polymers often increases the viscosity of foaming solutions and therefore it affects the kinetics of foam drainage and the rate of inter-bubble gas diffusion.[132, 133, 142] For example, polymers used in firefighting foams can significantly lengthen the drainage time by viscosifying the aqueous phase. In general polymeric additives make the foaming solution shear thinning non-Newtonian fluids.

To date only a few foam drainage studies have been devoted to non-Newtonian fluids, such as polymer solutions,[143, 144] while the majority of researches deal with Newtonian liquids, such as water, glycerin or oil. Despite intensive research in the field, to the best of our knowledge, only semi-empirical approaches have been developed so far and there is no comprehensive theory of foam drainage of non-Newtonian solutions. In previous publications[132,133,145] the influence of rheology of commercially available polymers Aculyn^{TM}22 (A22) and Aculyn^{TM}33 (A33) on the free foam drainage was investigated experimentally and the results of the properties modification (polymer type, concentration, mixtures, salt and iso-propanol addition) of A22 and A33 polymeric solutions were presented. Below a theory of foam drainage is developed for the non-Newtonian polymeric solutions in the case of free drainage and its results are compared with experimental data.

6.2 Materials and methods

6.2.1 Experiments

A22 is a hydrophobically-modified alkali soluble emulsion (HASE) and A33 is an anionic alkali polymer emulsion, water soluble, lightly crosslinked. Polymer emulsions were supplied by Dow. Both polymers are soluble in water at high pH (~12) and thus aqueous solutions of them were prepared by neutralising the stock polymer emulsions with a 2% ammonia solution in ultra-pure water produced by Millipore Q, with ascorbic and citric acids added (0.2 mass % each). NaCl was added to solutions in the range of 0-1.3 M concentrations. This composition represents the common system utilised in cosmetic products such as hair colourants where the ionic strength can be controlled by the added salt. The details about the preparation of polymeric solutions can be found in Refs.[132,133].

The rheometer AR 1000-N, TA Instruments with the cone and plate geometry (4 cm diameter, cone of 1°59′ and truncation of 56 μm) was used for the rheology measurements. Peltier plate was used to keep the temperature constant at 20°C. In the oscillating mode the strain sweep measurements have been performed in the range of 0.1–10 at frequency 1 Hz and in the flow mode shear rate measurements have been made at the values higher than 3 s^{-1} which corresponds to the local shear rates during the foam drainage.[143] The experimental error was lower than 5% at measuring probes taken from the same sample; however, the difference between individual samples of the same composition was higher, roughly 10%.

Surface tension measurements have been performed by the Drop shape analyser DSA100, Kruss, Germany. Buoyant air bubble was formed at the tip of the hooked capillary immersed in the cuvette containing a polymer solution in these experiments.

Foaming experiments have been performed in a home-made glass column of 380 mm height and 43 mm inner diameter. The foaming head, fitted at the bottom of the column, consisted of 19 capillaries of 0.18 mm inner diameter for a gas supply. The foaming gas was air. To study the kinetics of foam drainage, a foaming liquid was poured into the column to the height of about H_0=45 mm and bubbling was started at a constant flow rate. Bubbling was stopped after the foam height increased to about 150 mm. Time evolution of the height of the foam, H_2-H_1 (Fig. 6.1) and the liquid under the foam, H-H_2, (Fig. 6.1) were measured during the experiments. The average liquid volume fraction inside the foam during the drainage was calculated as (H_0-(H-H_2))/(H_2-H_1) and results of calculations are reported below. The produced foam was quite uniform and the variation of bubble size due to coarsening was negligible during the drainage (bubble coarsening parameter C was less than 10% for the solutions used in the experiments).[133] Accordingly, an average bubble size was determined for each foam drainage experiment by analysing the pictures taken from the whole column during the drainage. Each experimental run was repeated at least twice and the average values are reported below. The details of foam drainage experiments can be found in Refs.[132,133].

6.2.2 Theory

Let us consider foam composed of bubbles of uniform size and produced from polymeric solutions in a column of height *H* (Fig. 6.1). Drainage occurs in the vertical direction along the co-ordinate axis z directed downward, with z=0 at the top of the column. Time evolutions of the foam height and free liquid under the foam are H_2(t)-H_1(t) and *H*-H_2(t), respectively (Fig. 6.1). It is assumed below that the bubble size remains constant during the drainage, the dissipation occurs in the Plateau borders only and the contribution of the liquid flow in the films and nodes is neglected.

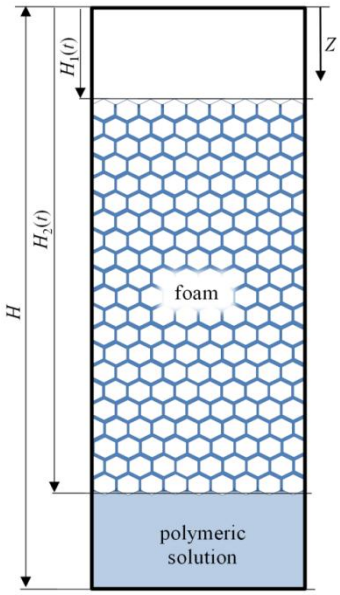

Figure 6.1: Schematic of free foam drainage experiment. Reproduced with permission from Ref.[146]. Copyright © 2016 Elsevier B.V.

It was determined in Ref.[133] (and shown below) that the polymeric solutions of A22 and A33 are non-Newtonian power-law liquids, which show a shear-thinning behaviour. For a power-law liquid dependence of the effective viscosity, μ, on applied shear rate is given by the well-known Ostwald–de Waele relation:

$$\mu = k\dot{\gamma}^{n-1}, \tag{6.1}$$

where *k* is flow consistency index, *n* is the flow behaviour index and $\dot{\gamma}$ is the shear rate.

A velocity profile for flow of a power-law fluid in a pipe of radius *R* with no-slip boundary condition is given by the following expression:[121]

$$u(r) = \frac{n}{n+1}\left(\left|\frac{dP}{dz}\right|\frac{1}{2k}\right)^{1/n}\left(R^{1+1/n} - r^{1+1/n}\right), \tag{6.2}$$

where *dP/dz* is the pressure gradient and everywhere below we assume that the flow directed downward along z. According to Eq. (6.2), the average velocity, *V*, in a circular tube of cross-sectional area of *A*, identical to that of actual Plateau border, is determined as follows:

$$V = \frac{n}{3n+1}\frac{1}{\pi^{1/2+1/(2n)}}\left(\left|\frac{dP}{dz}\right|\frac{1}{2k}\right)^{1/n} A^{1/2+1/(2n)}. \tag{6.3}$$

According to Ref.[147] the average velocity in the actual Plateau border geometry, *v*, is related to that given by Eq. (6.3) as:

$$v = cV, \tag{6.4}$$

where the coefficient *c* is:[147]

$$c = a(n). \tag{6.5}$$

In the above equation *a(n)* are functions of flow behaviour index, *n*, and their values are presented in Table 6.1. Here it is assumed that the interface is completely immobile (i.e. the Poiseuille flow).

Table 6.1: The values of velocity coefficient in Eq. (6.5) for different values of flow behaviour index. Data taken from Ref.[147]

n	1	0.8	0.6865	0.6	0.5	0.35
a(*n*)	0.5169	0.4851	0.459	0.434	0.3922	0.2942

Substitution of Eq. (6.3) into Eq. (6.4) results in

$$v = c\frac{n}{3n+1}\frac{1}{\pi^{1/2+1/(2n)}}\left(\left|\frac{dP}{dz}\right|\frac{1}{2k}\right)^{1/n} A^{1/2+1/(2n)}. \tag{6.6}$$

Hence, the flow rate, q_{Pb}, in a Plateau border is as follows:

$$q_{Pb} = c\frac{n}{3n+1}\frac{1}{\pi^{1/2+1/(2n)}}\left(\left|\frac{dP}{dz}\right|\frac{1}{2k}\right)^{1/n} A^{3/2+1/(2n)}. \tag{6.7}$$

The quantity *P* in Eqs. (6.2)-(6.7) is referred to *modified pressure* and it is an abbreviation for the sum of the capillary pressure and gravitational contributions. Accordingly, the driving force for Plateau border drainage *dP/dz* is:

$$\left|\frac{dP}{dz}\right| = \rho g + \frac{d}{dz}\left(\frac{\gamma}{R_{pb}}\right), \tag{6.8}$$

where γ is the liquid-air interfacial tension, R_{pb} is the radius of curvature of Plateau border; ρ and g are the liquid density and the gravity acceleration, respectively. According to Ref.[73]:

$$A = C^2 R_{pb}^2 = \frac{V_b}{n_p l}\frac{\varphi}{1-\varphi} = C_1 R_b^2 \frac{\varphi}{(1-\varphi)^{2/3}}, \tag{6.9}$$

where φ is liquid volume fraction, V_b is the volume of a bubble of radius R_b, l is the length of the Plateau border, n_p is the number of plateau borders per bubble; C^2~0.161, C_1 a geometrical coefficient, $C_1=4\pi/(3n_p\delta)$~0.378-0.972 for a foam with structures between bcc (body-centred cubic) and fcc (face-centred cubic) and bubbles of the same size ($l=\delta R_b(1-\varphi)^{-1/3}$, δ=0.718-1.108, n_p=6-10).[73] Substituting Eqs. (6.9) and (6.8) into Eq. (6.7) results in the following equation for the flow rate in a Plateau border:

$$q_{Pb} = c\frac{n}{3n+1}\frac{1}{\pi^{1/2+1/(2n)}}\frac{1}{2^{1/n}}\left(\frac{\rho g}{k}A^{3n/2+1/2} - \frac{C\gamma}{2k}A^{3n/2-1}\frac{\partial A}{\partial z}\right)^{1/n}. \tag{6.10}$$

If we define

$$\frac{1}{f_n} = \left(c\frac{n}{3n+1}\frac{1}{\pi^{1/2+1/(2n)}}\frac{1}{2^{1/n}}\right)^n, \tag{6.11}$$

then Eq. (6.10) can be rewritten as

$$q_{Pb} = \left(\frac{\rho g}{k f_n}A^{3n/2+1/2} - \frac{C\gamma}{2k f_n}A^{3n/2-1}\frac{\partial A}{\partial z}\right)^{1/n}. \tag{6.12}$$

According to Eq. (6.11) and Table (6.1), f_n~49 for a Newtonian liquid ($n=1$) and immobile interface which is in complete agreement with the values reported earlier.[75,85,148]

The total volumetric flux through the Plateau borders is therefore calculated as:[149,150]

$$Q = \frac{4}{15} N n_p R_b \left(\frac{\rho g}{k f_n} A^{3n/2+1/2} - \frac{C\gamma}{2k f_n} A^{3n/2-1} \frac{\partial A}{\partial z} \right)^{1/n}, \tag{6.13}$$

where $N=(1-\varphi)/V_b$ is the number of bubbles per unit volume.

The mass conservation law for liquid inside Plateau border channels is[149]

$$\frac{\partial \varphi}{\partial t} + \frac{\partial Q}{\partial z} = 0. \tag{6.14}$$

Substituting Eq. (6.13) into Eq. (6.14) and replacing A with expression (6.9) results in the following equation for the liquid volume fraction, φ:

$$\frac{\partial \varphi}{\partial t} + \frac{\partial}{\partial z} \left(\frac{C_1^{1/2} \rho g}{k \alpha_n} R_b^{n+1} \frac{\varphi^{3n/2+1/2}}{(1-\varphi)^{1/3}} - \frac{C\gamma}{2k\alpha_n} R_b^n \frac{\varphi^{3n/2-1}(1-\varphi/3)}{(1-\varphi)} \frac{\partial \varphi}{\partial z} \right)^{1/n} = 0, \tag{6.15}$$

where

$$\frac{1}{\alpha_n} = \left(c \frac{n}{3n+1} \frac{1}{2^{1/n-3} 3^{3/2} 5} \frac{1}{n_p^{1/2} \delta^{3/2} \pi^{1/(2n)}} \right)^n. \tag{6.16}$$

Let us introduce the following dimensionless variable and co-ordinate:

$$\zeta \to z/z_0, \quad \tau \to t/t_0, \tag{6.17}$$

where

$$z_0 = \sqrt{\frac{\gamma}{\rho g}}, \; t_0 = \left(\frac{2\alpha_n k}{C\gamma^{\frac{1-n}{2}} R_b^n (\rho g)^{\frac{n+1}{2}}} \right)^{1/n}. \tag{6.18}$$

Substitution of these variables into Eq. (6.15) results in

$$\frac{\partial \varphi}{\partial \tau} + \frac{\partial}{\partial \zeta} \left(2\sqrt{Bo} \frac{\varphi^{3n/2+1/2}}{(1-\varphi)^{1/3}} - \frac{\varphi^{3n/2-1}(1-\varphi/3)}{(1-\varphi)} \frac{\partial \varphi}{\partial \zeta} \right)^{1/n} = 0, \tag{6.19}$$

where

$$Bo = \frac{\Delta p_{grav}}{\Delta p_{cap}} = \frac{\rho g \frac{C_1^{1/2}}{C} R_b}{\frac{\gamma}{\frac{C_1^{1/2}}{C} R_b}} = \frac{C_1}{C^2} \frac{\rho g R_b^2}{\gamma}, \tag{6.20}$$

is a corresponding Bond number.

For a fresh foam produced in the foam column, the liquid volume fraction profile is initially uniform, that is, $\varphi(\zeta, \tau = 0) = \varphi_i$.[151,152]

6.2.2.1 Boundary conditions

During the drainage the liquid from the top of the foam drains to the lower parts. Therefore, the liquid volume fraction at the top decreases with time. There is a critical liquid volume fraction, φ_{cr}, below which the coalescence/bubble burst begins.[153] The value of this critical liquid volume fraction is a function of the nature of the surface active substances (polymer and/or surfactant) and their concentration. The critical liquid volume fraction is determined by a disjoining pressure action.[149,154,155] However, in Ref.[153] a mechanism based on a critical film dilatation is proposed for the onset of coalescence and critical liquid content in draining foams. Based on the theory of critical liquid volume fraction, there are two possible scenarios for the boundary condition at the top of the foam (i.e. z=H_1(t) or ζ= ζ_1(t)): (i) If the liquid volume fraction at z=H_1 is higher $_{\text{than}}$ φ_{cr}, then there is no bubble collapsing at the top of the foam (i.e. dH_1/dt=0) and the top boundary condition is zero liquid flux:

$$Q(H_1, t) = 0, \tag{6.21}$$

or in dimensionless form:

$$Q(\zeta_1, \tau) = 0, \tag{6.22}$$

(ii) If the foam continues to dry and the liquid volume fraction at z=H_1 drops to the value of φ_{cr}, then the bubbles at the top of the foam start to rupture and the height of the foam decreases from the top (i.e. dH_1/dt>0). In this case the boundary condition at the top of the foam is a constant liquid volume fraction:

$$\varphi(H_1(t), t) = \varphi_{cr} \tag{6.23}$$

or

$$\varphi(\zeta_1(\tau), \tau) = \varphi_{cr} \tag{6.24}$$

and the rate of foam collapse, dH_1/dt, can be expressed according to the following equation:[149]

$$\frac{dH_1(t)}{dt} = \frac{1}{\varphi_{cr}} Q(H_1(t), t), \tag{6.25}$$

or in dimensionless form:

$$\frac{d\zeta_1(\tau)}{d\tau} = \frac{1}{\varphi_{cr}} Q(\zeta_1(\tau), \tau). \tag{6.26}$$

After the onset of the drainage, the boundary condition at the bottom of the foam is a constant liquid volume fraction, φ_{max}~0.36, which corresponds to random packing limit for spherical particles in three dimensions.[156] However, as we consider a uniform initial liquid volume fraction along the foam height (i.e. $\varphi_{cr} << \varphi(\zeta, \tau = 0) = \varphi_i < \varphi_{max}$), the boundary condition at the bottom of the foam should be zero liquid flux during a very early stage of the drainage until the liquid volume fraction at the bottom of the foam reaches φ_{max}.

As the foam drains the polymeric solution accumulates under the foam and the interface between the foam and polymeric solution, H_2, moves up. The rate of this movement can be found using a mass conservation law of the polymeric solution within the whole column (see Appendix 6.A):

$$\frac{dH_2(t)}{dt} = -\frac{1}{1-\varphi_{max}} Q(H_2(t), t), \tag{6.27}$$

or in dimensionless form:

$$\frac{d\zeta_2(t)}{d\tau} = -\frac{1}{1-\varphi_{max}} Q(\zeta_2(\tau), \tau). \tag{6.28}$$

The above equations could be easily deduced from the fact that the product of the front velocity with the density difference of the two sides of the front is equal to the flux.

The equilibrium profile for liquid content inside the foam is reached when the gravity and capillary gradient forces equilibrate each other inside the foam. The equilibrium profile can be found by assuming zero liquid flux across the foam

height. Integration of Eq. (6.15) in this case using the boundary condition at the bottom of the foam ($\varphi(H_2(t),t)=\varphi_{\max}$) results in:

$$\frac{2C_1^{1/2}\rho g R_b}{C\gamma}\int_z^{H_{2e}}\partial z=\int_{\varphi_{eq}}^{\varphi_{\max}}\varphi^{-3/2}(1-\varphi)^{-2/3}(1-\varphi/3)\partial\varphi\,, \tag{6.29}$$

and

$$(1-\varphi_e(z))^{1/3}\varphi_e^{-1/2}(z)=(1-\varphi_{\max})^{1/3}\varphi_{\max}^{-1/2}+\frac{C_1^{1/2}\rho g R_b}{C\gamma}(H_{2e}-z)\,. \tag{6.30}$$

Eq. (6.30) can be rewritten as the following dimensionless form:

$$(1-\varphi_e(\zeta))^{1/3}\varphi_e(\zeta)^{-1/2}=(1-\varphi_{\max})^{1/3}\varphi_{\max}^{-1/2}+\sqrt{Bo}(\zeta_{2e}-\zeta)\,. \tag{6.31}$$

Eq. (6.31) shows that as expected, the equilibrium profile does not depend on flow behaviour index, *n*, and it is identical to foams produced from Newtonian liquids. The calculated profile of the equilibrium liquid volume fraction is in good agreement with the results presented in Ref.[157] using the concept of an osmotic pressure (see Fig. 6B.1 in Appendix 6.B).

If $\zeta=\zeta_{1e}$ is substituted in the above equation (we suppose that ζ_{1e} is the dimensionless position of the top of the foam at equilibrium), then the equilibrium liquid volume fraction at the top of the foam can be deduced. The latter is a function of the foam height at equilibrium, $\zeta_{2e}-\zeta_{1e}$ and can be calculated as

$$(1-\varphi_e(\zeta_{1e}))^{1/3}\varphi_e(\zeta_{1e})^{-1/2}=(1-\varphi_{\max})^{1/3}\varphi_{\max}^{-1/2}+\sqrt{Bo}(\zeta_{2e}-\zeta_{1e})\,. \tag{6.32}$$

The dependency of the equilibrium liquid volume fraction at the top of the foam on the foam height (according to Eq. (6.32)) is schematically illustrated in Fig. 6.2. As shown in Fig. 6.2, $\varphi_e(\zeta_{1e})$ increases to $\varphi_{\max}$ as the final foam height, $\zeta_{2e}-\zeta_{1e}$, decreases. Substituting $\varphi_e(\zeta_{1e})=\varphi_{cr}$ in Eq. (6.32) allows determining a critical foam height, λ_{cr}. This critical foam height is shown in Fig. 6.2 where $\varphi_e(\zeta_{1e})=\varphi_{cr}$.

If the initial foam height, $\zeta_2(\tau=0)-\zeta_1(\tau=0)=\zeta_{2i}-\zeta_{1i}$ is less than λ_{cr} then over duration of the whole process the liquid volume fraction at the top of the foam remains above the φ_{cr} and the top part of the foam does not move, that is

$\zeta_1(\tau) = \zeta_{1i}$. However, if $\zeta_{2i} - \zeta_{1i}$ is bigger than λ_{cr} then two possibilities can be predicted: (1) over duration of the whole drainage process the liquid volume fraction at the top of the foam remains above the φ_{cr}, which is exactly the same as before, (2) at some moment in time, τ_{cr}, $\varphi(\zeta_1, \tau_{cr}) = \varphi_{cr}$. After that moment the apparent boundary of the foam at the top starts to decrease according to Eq. (6.26).

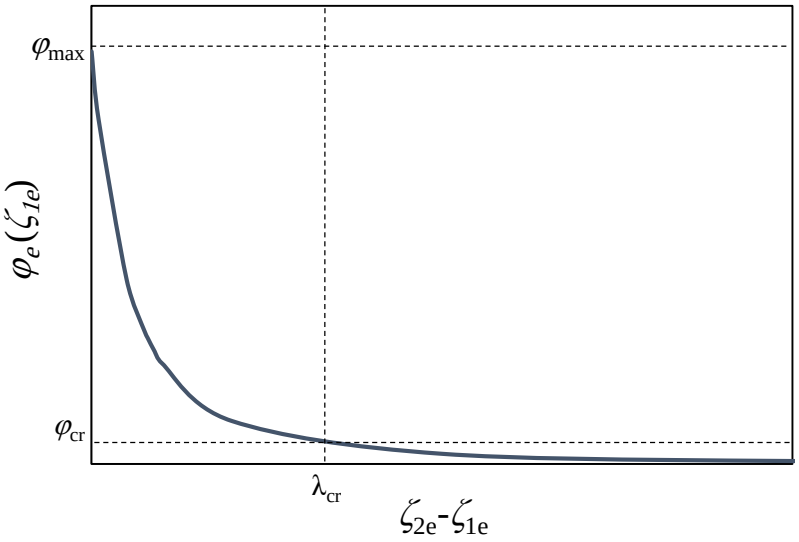

Figure 6.2: The dependency of the equilibrium liquid volume fraction at the top of the foam on the foam height. Reproduced with permission from Ref.[146]. Copyright © 2016 Elsevier B.V.

Therefore, the foam height will decrease from both top and bottom boundaries while $\varphi(\zeta_1, \tau) = \varphi_{cr}$. This reduction in foam height continues until the time when it reaches equilibrium. According to Eq. (6.32) and Fig. 6.2, the final height of the foam in this case is fixed and equal to the critical foam height, $\zeta_{2e} - \zeta_{1e} = \lambda_{cr}$. Considering a mass conservation of the polymeric solution within the whole column at initial and final state of the process, it is possible to predict which of the two above mentioned possibilities will occur:

$$\varphi_i(H_{2i} - H_{1i}) + H - H_{2i} = \int_{H_{1e}}^{H_{2e}} \varphi_e(H)dH + H - H_{2e} \,. \tag{6.33}$$

The left hand side of the equation shows the initial amount of the liquid presented within the whole column while the right hand side of the equation determines the final liquid content at equilibrium. Eq. (6.33) can be rewritten as the following dimensionless form:

$$\varphi_i(\zeta_{2i}-\zeta_{1i})-\zeta_{2i}=\int_{\zeta_{1e}}^{\zeta_{2e}}\varphi_e(\zeta)d\zeta-\zeta_{2e}\,. \tag{6.34}$$

If we suppose that during the drainage the liquid volume fraction at the top of the foam drops to the value of φ_{cr} (i.e. the second possibility occurs), then as mentioned above $\zeta_{2e}=\zeta_{1e}+\lambda_{cr}$. Substituting this expression into Eq. (6.34) results in

$$\varphi_i(\zeta_{2i}-\zeta_{1i})-\zeta_{2i}=\int_{\zeta_{1e}}^{\zeta_{1e}+\lambda_{cr}}\varphi_e(\zeta)d\zeta-(\zeta_{1e}+\lambda_{cr})\,. \tag{6.35}$$

From the above equation

$$\zeta_{1e}-\zeta_{1i}=(\zeta_{2i}-\zeta_{1i})-\varphi_i(\zeta_{2i}-\zeta_{1i})+\int_{\zeta_{1e}}^{\zeta_{1e}+\lambda_{cr}}\varphi_e(\zeta)d\zeta-\lambda_{cr}\,. \tag{6.36}$$

Since the foam height decreases from the top in this case, $\zeta_{1e}-\zeta_{1i}>0$ and the right hand side of Eq. (6.36) should be also a positive value:

$$(\zeta_{2i}-\zeta_{1i})-\varphi_i(\zeta_{2i}-\zeta_{1i})+\int_{\zeta_{1e}}^{\zeta_{1e}+\lambda_{cr}}\varphi_e(\zeta)d\zeta-\lambda_{cr}>0\,. \tag{6.37}$$

According to the above equation the condition for the movement of the top of the foam during the drainage can be written as:

$$\varphi_i<1-\frac{\left(\lambda_{cr}-\int_{\zeta_{1e}}^{\zeta_{1e}+\lambda_{cr}}\varphi_e(\zeta)d\zeta\right)}{(\zeta_{2i}-\zeta_{1i})}, \tag{6.38}$$

or

$$\varphi_i < 1 - \frac{\left(\lambda_{cr} - \int_0^{\lambda_{cr}} \varphi_e(\zeta_{2e} - \zeta)d\zeta\right)}{(\zeta_{2i} - \zeta_{1i})} = \varphi_t \,, \tag{6.39}$$

A comparison between the values of φ_i and φ_t for each foaming solution can predict the state of the top of the foam during the drainage. The integral in Eq. (6.39) (to find the values of φ_t) can be calculated numerically using Eq. (6.31) for different values of Bo number and it is identical to the area under the equilibrium curve from $\zeta_{2e} - \zeta_{1e} = 0$ to $\zeta_{2e} - \zeta_{1e} = \lambda_{cr}$ in Fig. 6.2. Therefore, in the case in which the initial foam height, $\zeta_{2i} - \zeta_{1i}$, is bigger than λ_{cr} the foam height decreases from the top boundary only if the condition specified in Eq. (6.39) is satisfied for the value of initial liquid volume fraction. Otherwise the liquid volume fraction at the top of the foam remains above the φ_{cr} and the top boundary of the foam does not move.

6.2.2.2 Model calculation

The model of foam drainage described by dimensionless Eq. (6.19) has been solved using finite element method on one dimensional regular grid with 800-1200 elements corresponding to the foam height. A backward differentiation formula was used to solve time-dependent variables and time stepping was free taken by solver with initial step size of 10^{-20}. Relative tolerance was set to 10^{-8}, whereas absolute tolerance was set to 10^{-10}. The boundary conditions at the top and bottom of the foam and their locations were imposed and updated as described in the previous section to obtain the evolution of liquid volume fraction inside the foam. The values of t_0, z_0, Bo, λ_{cr}, flow behaviour index, n, and flow consistency index, k, are obtained for different polymeric solutions based on the experimental data shown in the next section.

6.3 Results and discussion

6.3.1 Rheology and surface tension measurements of polymeric solutions

The rheology of polymeric solution is an important parameter in the kinetic of the foam drainage. Fig. 6.3 shows the dependency of the measured effective viscosity of different polymeric solutions on shear rate. The dependencies are fitted according to Eq. (6.1). The obtained values of *k* and *n* for different polymeric solutions are listed in Table 6.2 and are used in calculations below. The shear thinning character of the polymeric solutions was found, as expected. Fig. 6.3(a) shows that the solutions viscosity decreases with increasing of the salt concentration. Fig. 6.3(b) also indicates that solution viscosity increases with the increase of the polymer concentration. The values of surface tension for different polymeric solutions are given in Table 6.2 and they are used in calculations.

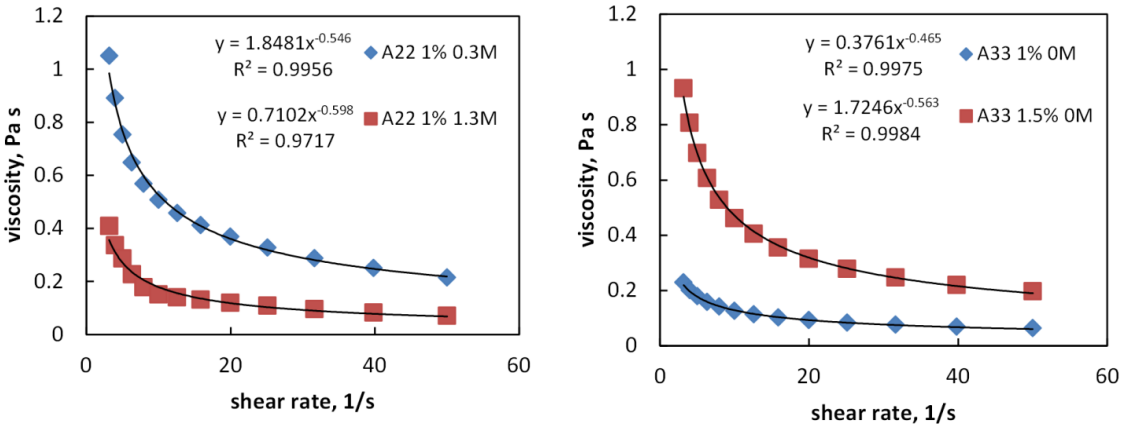

a) b)

Figure 6.3: The dependency of the measured effective viscosity of a) A22 and b) A33 solutions on shear rate. The dependencies are fitted according to Eq. (6.1). Fitted values are given in Table 6.2. Reproduced with permission from Ref.[146]. Copyright © 2016 Elsevier B.V.

6.3.2 Foam drainage of polymeric solutions

Drainage of foams produced from power-law non Newtonian liquids of three compositions of A22 and A33 polymers have been chosen for investigation as shown in Table 6.2. The density of all solutions was around 1000 kg/m^3. Each foam drainage experiment was performed for 120 minutes. The average bubble size reported in Table 6.2 indicates that the foams formed from the more viscous solutions had larger bubbles. Based on the four obtained experimental data, *k, n,* γ and R_b, we calculated *Bo, c,* α_n, z_0, t_0 and λ_{cr} according to Eqs. (6.20), (6.5), (6.16),

(6.18), (6.18) and (6.32) respectively, and their values for each foaming solutions are reported in Table 6.2. The values of velocity coefficient, *c*, were found according to Eq. (6.5) and Table 6.1. To find the critical foam height, λ_{cr}, (according to Eq. (6.32)) the values of critical liquid volume fraction φ_{cr}, are required. In Ref.[153] a narrow field of liquid fraction ranging from 0.0005 to 0.0007 was found as the critical liquid volume fraction in foam stabilised by mixture of surfactants. As a rough estimate, this range was used below to calculate the critical foam height. As can be seen in Table 6.2, the initial foam height (~0.15 m) is higher than the estimated critical values for different polymeric solutions. The values of φ_t in Eq. (6.39) are also calculated for each foaming solution and their values are reported in Table 6.2. The initial liquid volume fraction, φ_i (~0.25-0.30) is lower than the calculated values of φ_t; thus, the condition specified in Eq. (6.39) is satisfied. Although this suggests that the liquid volume fraction at the top of the foam drops to the value of φ_{cr} and the foam height decreases from the top boundary, the measured experimental data showed that the change of the location of the top of the foam, H_1, was negligible compared to the change of the foam height, H_2-H_1, for all polymeric solutions during the drainage (maximum 7.4 %). Foams produced from polymeric solutions are more stable than foams build up by surfactant solutions; thus, φ_{cr} is expected to be lower and λ_{cr} should be higher for foams stabilized by polymers than by surfactants only. It confirms that the liquid volume fraction at the top of the foam $\varphi(H_1,t)$ does not decrease to the value of φ_{cr} during the draining and, hence, zero liquid flux boundary condition (Eqs. (6.21) and (6.22)) was used in the simulations below. Accordingly, the value of φ_{cr} is set so low that there is no collapse for the foams examined here. Our calculations according to Eq. (6.39) suggest a value of roughly 0.0001 for the critical liquid volume fraction φ_{cr} within the foams produced from the polymeric solutions used in our experiments.

Table 6.2: Characteristic values of polymeric solutions and their foam drainage. The first four values, k, n, γ and R_b are extracted from the experimental data. The second seven values, Bo, c, α_n, z_0, t_0, λ_{cr} and φ_t are calculated according to Eqs. (6.20), (6.5), (6.16), (6.18), (6.18), (6.32) and (6.39), respectively. Reproduced with permission from Ref.[146]. Copyright © 2016 Elsevier B.V.

Foaming solutions	k (Pa.s^n)	n (-)	γ (N/m)	R_b (m)	Bo (-)	c (-)	α_n (-)	z_0 (m)	t_0 (s)	λ_{cr} (-), (m)	φ_t (-)
A22_1.0%1.3M	0.7102	0.402	0.038	0.00139	3.003	0.334	20.575	0.00197	38.449	20.976-24.973, 0.041-0.049	0.67-0.72
A33_1.0%0M	0.3761	0.535	0.030	0.00131	3.358	0.408	31.033	0.00175	13.115	19.837-23.617, 0.035-0.041	0.73-0.78
A33_1.5%0M	1.7246	0.437	0.027	0.00158	5.435	0.358	22.916	0.00166	316.148	15.593-18.564, 0.026-0.031	0.80-0.83

Fig. 6.4 shows calculated results on the time evolution of liquid volume fraction, φ, over the foam height, ζ, for "A33_1.0% 0M" solution. In this figure ζ=0 is the top of the foam and φ_i=0.2939, according to the experimental data. In the very beginning of the drainage the liquid volume fraction varies only at the top and bottom of the foam, whereas in the middle part of the foam the initial value is retained. The interface between the foam and polymeric solution at the bottom is moving up during the drainage. This decrease of the foam height is very fast in the early stage of the drainage; however, reduction of the foam height and the profile of the liquid volume fraction approach a steady state over time.

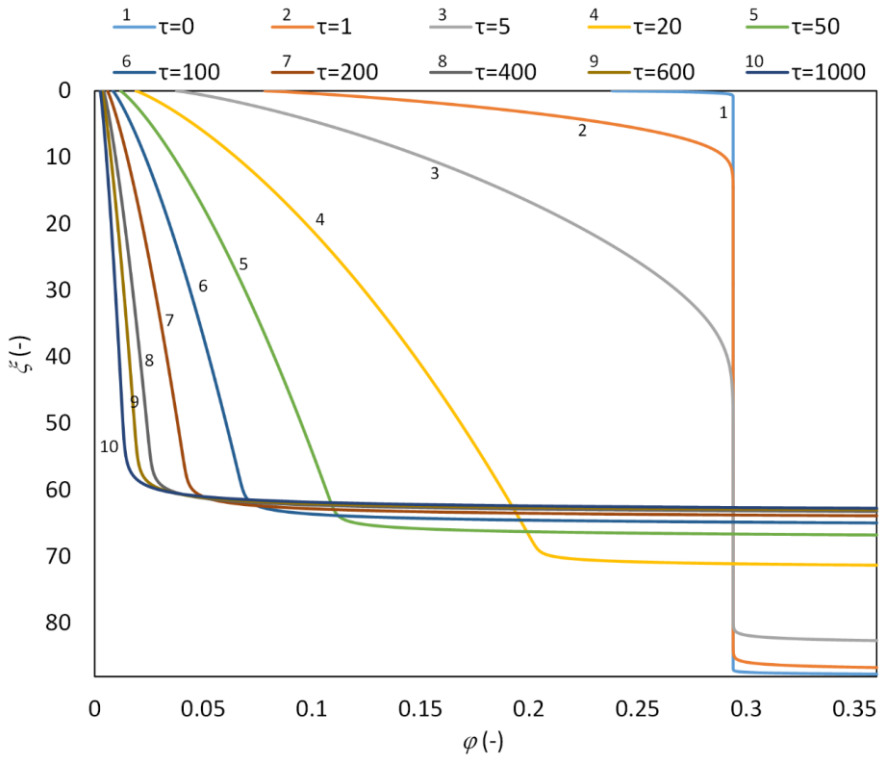

Figure 6.4: Time evolution of the predicted results of liquid volume fraction, φ, over the foam height, ζ, for "A33_1.0% 0M" solution (ζ=0 corresponds to the top of the foam). Reproduced with permission from Ref.[146]. Copyright © 2016 Elsevier B.V.

Comparison of the predicted and experimental time evolution of the height of the foam, ζ_2-ζ_1, and average liquid volume fraction, φ, is shown in Figs. 6.5 and 6.6, respectively for different polymeric solutions. As expected, for all polymeric solutions the foam height and the average liquid volume fraction decrease dramatically in the beginning of the drainage and after some time they reach a plateau. As can be seen in Figs. 6.5 and 6.6, the predicted values are in a quantitative agreement with the measured experimental data (R^2>0.85) especially for lowly viscous non-Newtonian solutions. However, in the case of "A33_1.5% 0M" solution, which has the highest k value (k=1.7246 Pa.s^n), there is a deviation between the theoretical predictions and experimental results in the initial stage of the drainage (see Figs. 6.5(c) and 6.6(c)). The latter can be attributed to the assumption of immobile surface of the Plateau border and Poiseuille-like flow. It seems that in the case of "A33_1.5% 0M" solution (the highest viscosity), the surface of Plateau border is not completely immobile in the initial stage of the drainage and there is some mobility at the surface of Plateau border. According to Ref.[143] elongational properties of the polymeric solution can also affect the foam drainage. It was found

that the rate of the drainage increases by increasing the elongational viscosity of the solutions. This influence can be important at higher concentration of the polymeric solutions and with larger polymer molecular weights,[143,144] this phenomenon could account for the small deviations between predicted results and experimental data presented below.

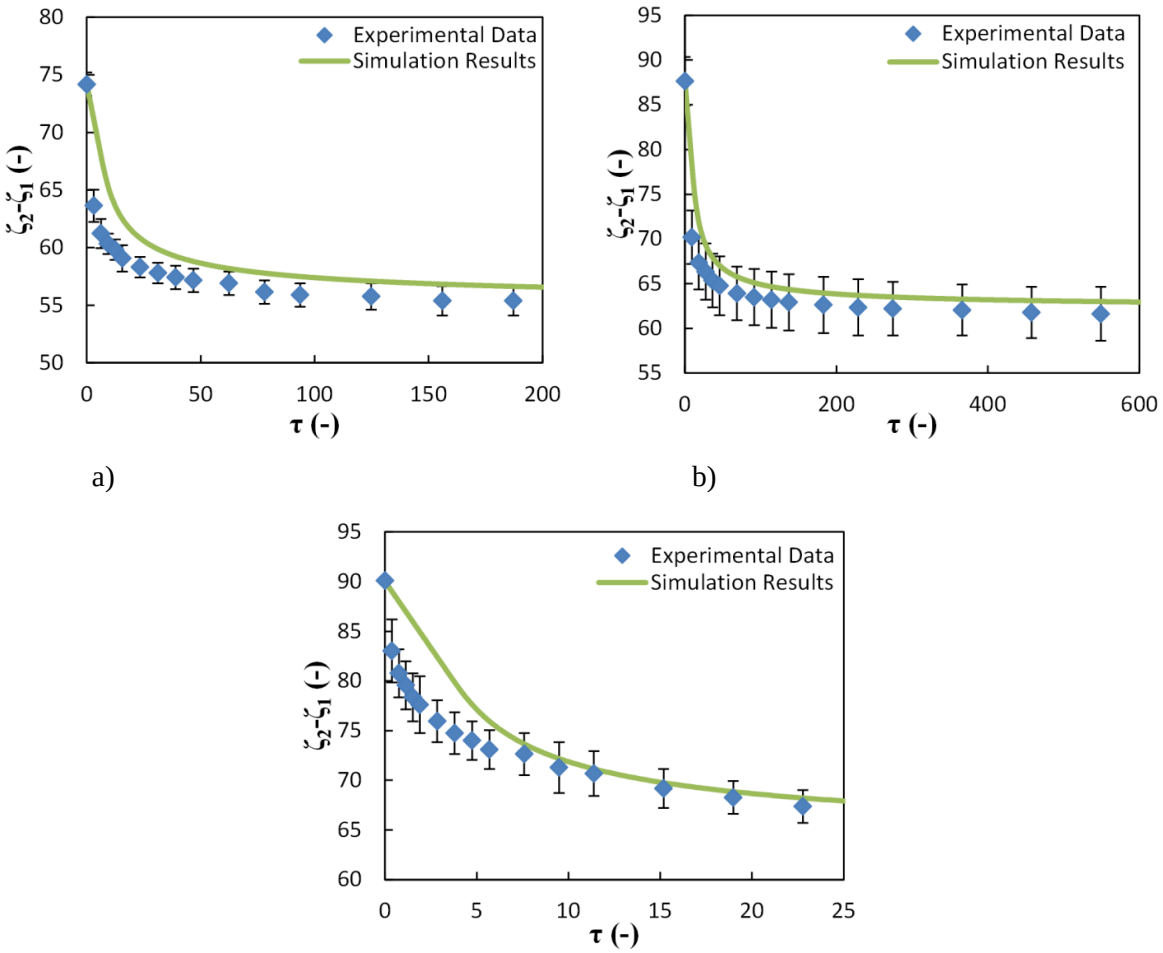

Figure 6.5: Comparison of the predicted time evolution of the height of the foam, ζ_2-ζ_1, with experimental data for a) A22_1.0% 1.3M, b) A33_1.0% 0M and c) A33_1.5% 0M. Reproduced with permission from Ref.[146]. Copyright © 2016 Elsevier B.V.

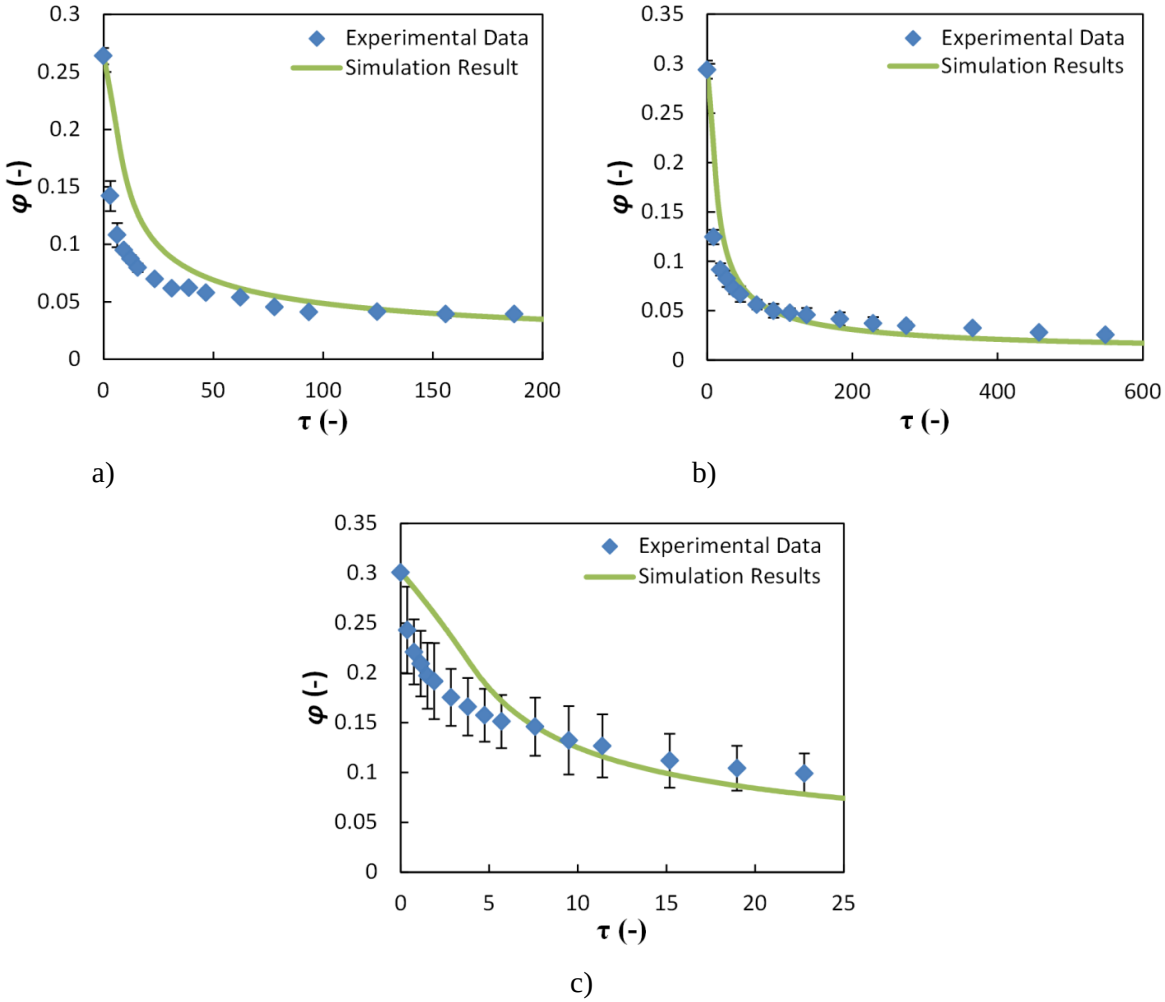

Figure 6.6: Comparison of the predicted time evolution of the average liquid volume fraction along the foam height, φ, with experimental data for a) A22_1.0% 1.3M, b) A33_1.0% 0M and c) A33_1.5% 0M. Reproduced with permission from Ref.[146]. Copyright © 2016 Elsevier B.V.

6.4 Conclusions

A model for free drainage of foams produced from power-law non-Newtonian shear thinning liquids is presented and compared with experimental data for the drainage of foams formed by A22 and A33 polymeric solutions. Equation was deduced, which describes the drainage of foam build up by a power-law non-Newtonian liquid. The boundary condition at foam/liquid interface is a constant liquid volume fraction corresponding to the maximum liquid volume fraction inside the foam. There are two possible boundary conditions at the top of the foam which depends on the initial foam height and initial liquid content within the foam: (i) If the liquid

content at the top is higher than a critical liquid volume fraction, there is no collapsing of bubbles at the top of the foam and boundary condition is zero liquid flux; (ii) If the liquid volume fraction at the top of the foam drops to a critical value, the height of the foam decreases from the top by collapsing of the bubbles at the top of the foam. The predicted values showed that in the early stage of the drainage the liquid content varies only at the top and bottom of the foam, whereas in the middle section of the foam the initial value is retained. The interface between the foam and polymeric solution was moving up during the drainage and the kinetics of this motion is predicted. This decrease in the foam height was very fast in the very beginning of the drainage; however, it reached a steady state over time. The equilibrium profile of the liquid volume fraction is predicted and shown that it does not depend on power law index, *n*, of non-Newtonian liquid. The predicted values of the time evolution of the foam height and liquid content were in good agreement with the experimental data.

Nomenclature 6

a	velocity coefficient
A	Plateau border cross-sectional area, m^2
Bo	Bond number
c	velocity coefficient
C	geometrical coefficient
C_1	geometrical coefficient
$,f_n$	drag coefficient
g	gravity acceleration, m/s^2
H	column height, m
H_0	initial height of the liquid before producing the foam, m
H_1	position of the top of the foam, m
H_{1e}	position of the top of the foam at equilibrium, m

H_{1i}	initial position of the top of the foam, m
H_2	position of the foam/polymeric solution boundary, m
H_{2e}	position of the foam/polymeric solution boundary at equilibrium, m
H_{2i}	initial position of the foam/polymeric solution boundary, m
k	flow consistency index, Pa s^n
l	length of the Plateau border, m
n	flow behaviour index
n_p	number of plateau borders per bubble
N	number of bubbles per unit volume, $1/m^3$
p	pressure, Pa
P	modified pressure, Pa
q_{Pb}	flow rate in Plateau border, m^3/s
Q	total volumetric flux through the Plateau borders, m/s
r	radial co-ordinate, m
R	radius, m
R_b	radius of bubbles, m
R_{Pb}	curvature radius of Plateau border, m
t	time, s
t_0	characteristic time scale, s
u	velocity, m/s
V	average velocity in a circular tube, m/s
V_b	bubble volume, m^3
z	co-ordinate axis, m
z_0	characteristic length scale, m

Greek symbol

α_n	coefficient in Eq. (6.15)
γ	surface tension, N/m
$\dot{\gamma}$	shear rate, s^{-1}
δ	geometrical coefficient
ζ	dimensionless vertical co-ordinate
ζ_1	dimensionless position of the top of the foam
ζ_{1e}	dimensionless position of the top of the foam at equilibrium
ζ_{1i}	dimensionless initial position of the top of the foam
ζ_2	dimensionless position of the foam/polymeric solution boundary
ζ_{2e}	dimensionless position of the foam/polymeric solution boundary at equilibrium
ζ_{2i}	dimensionless initial position of the foam/polymeric solution boundary
λ_{cr}	dimensionless critical foam height
μ_{eff}	effective viscosity, Pa s
ν	average velocity in actual Plateau border geometry, m/s
ρ	liquid density, kg/m^3
τ	dimensionless time
φ	liquid volume fraction
φ_i	initial liquid volume fraction
φ_{cr}	critical liquid volume fraction
φ_e	equilibrium liquid volume fraction
φ_{max}	maximum liquid volume fraction

Appendix 6.A

The rate of the movement of the interface between foam and polymeric solutions

As the foam drains the polymeric solution accumulates under the foam and the interface between the foam and polymeric solution, H_2, moves up. To find the rate of this movement, let us consider a mass conservation law of the polymeric solution within the whole column:

$$\int_{H_1(t)}^{H_2(t)} \varphi(z,t)dz + H - H_2(t) = cons \,. \tag{6A.1}$$

Differentiating Eq. (6A.1) with time results in:

$$\frac{d}{dt}\int_{H_1(t)}^{H_2(t)} \varphi(z,t)dz - \frac{dH_2(t)}{dt} = 0 \,. \tag{6A.2}$$

When the liquid volume fraction at the top of the foam is higher than critical liquid volume fraction, $\varphi(H_1,t) > \varphi_{cr}$, H_1 is constant and in this case applying Leibnitz rule for differentiation of the integral in Eq. (6A.2) leads to the following expression:

$$\varphi_{\max}\frac{dH_2(t)}{dt} + \int_{H_1}^{H_2(t)} \frac{d\varphi(z,t)}{dt}dz - \frac{dH_2(t)}{dt} = 0 \,. \tag{6A.3}$$

Substituting Eq. (6.14) and using expression (6.21) leads to the following equation for the rate of moving boundary between the foam and polymeric solution:

$$\frac{dH_2(t)}{dt} = -\frac{1}{1-\varphi_{\max}} Q(H_2(t),t) \,, \tag{6A.4}$$

or in dimensionless form:

$$\frac{d\zeta_2(t)}{d\tau} = -\frac{1}{1-\varphi_{\max}} Q(\zeta_2(\tau),\tau) \,. \tag{6A.5}$$

However, when the liquid volume fraction at the top of the foam decreases to critical liquid volume fraction, $\varphi(H_1(t),t) = \varphi_{cr}$, H_1 is a function of time and it moves

down. In this case differentiation of the integral in Eq. (6A.2) and using Eq. (6.14) result in:

$$\varphi_{\max}\frac{dH_2(t)}{dt}-\varphi_{cr}\frac{dH_1(t)}{dt}-Q(H_2(t),t)+Q(H_1(t),t)-\frac{dH_2(t)}{dt}=0\,. \qquad (6A.6)$$

If the rate of foam collapse, dH_1/dt, according to Eq. (6.25) is substituted in the above equation then again Eq. (6A.4) is recovered for the rate of moving interface between the foam and liquid.

Appendix 6.B

The comparison of the calculated profile of the equilibrium liquid volume fraction according to Eq. (6.31) with the results reported in Ref.[157] is presented in Fig. 6B.1.

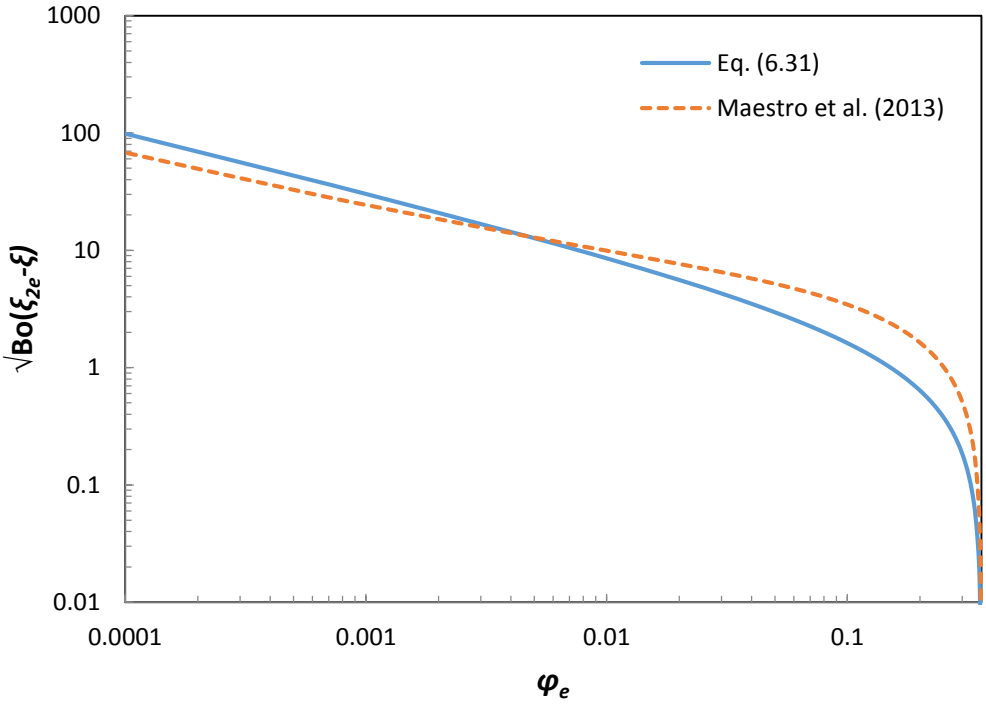

Figure 6B.1: Comparison of the calculated profile of the equilibrium liquid volume fraction according to Eq. (6.31) with the results presented in Ref.[157]. Reproduced with permission from Ref.[146]. Copyright © 2016 Elsevier B.V.

CHAPTER 7

FOAM DRAINAGE PLACED ON POROUS SUBSTRATES

Overview

In the previous chapter a theory of foam drainage was developed for the non-Newtonian polymeric solutions in the case of free drainage. Below a completely new mathematical model of drainage of foam produced from Newtonian solutions and in contact with porous surfaces is introduced. The results of investigations were published in *Soft Matter* 11, 3643–3652, 2016 and *The European Physical Journal Special Topics* 224, 459–471 and reused in this chapter with permission. Initially in this chapter, the difference between the drainage of foam in the case of a free drainage and a drainage of a foam placed on a porous substrate is explained. Then a mathematical model along with appropriate boundary conditions is derived for foam drainage placed on a porous substrate. In the next section, the predicted results for different properties of foam and porous substrate are analysed and accordingly different regimes of the process are identified.

7.1 Introduction

In this chapter theoretical findings on drainage of foams placed on porous surfaces is presented. For many applications, particularly in pharmacy and cosmetics, the interaction of foam with substrate is of considerable importance as often the surfaces where foam is applied on are porous (skin, hair, textile materials). Recent investigations have confirmed that foams are an efficient alternative method of drug delivery on the skin of patients.[5-8] Lotions, creams, gels and ointment are the most common topical vehicle delivery systems that have been applied in dermatology; foams are delivery systems which grow in popularity. The density of foams is much lower than that of traditional vehicles and they spread out more easily.[72] This reduces the requirement of applying pressure or prolonged period of contact with the

sensitive diseased skin.[6] In addition, drugs from foams absorb and penetrate more quickly as compared to other carriers.

The rate of drug delivery from foams can be controlled by the rate of foam drainage and collapse. Kinetics of topical drug delivery can be tailored by varying such foam characteristics as the bubbles size, liquid viscosity, initial liquid content and surface tension. In order to make a proper choice of foam characteristics, processes of drug delivery from foam should be considered in connection with the properties of substrate where the foam is applied to (skin or hair). Skin or bunch of hair have porous structure of their own, therefore an additional phenomenon, a capillary suction into porous substrate affects the foam drainage/imbibition.

Analysis of liquid drainage and flow in foams confined in porous media has been widely investigated in literature[79,158-163] from both theoretical and experimental points of view. However, a theoretical description of foam drainage/imbibition in contact with a porous substrate (i.e. a foam placed on the top of a porous substrate), which is applicable to the analysis of liquid release from foam into skin or bunch of hair, was recently introduced in Refs.[148,164]. The aim of this chapter is to present a new theory of foam drainage in contact with a porous substrate. To identify the methods to control the kinetics of liquid release in this case a direct numerical simulation of foam drainage in contact with a porous substrate is developed. The mathematical model combines the foam drainage equation with the equation describing the imbibition of liquid in the porous substrate coupled with appropriate boundary conditions at foam/porous substrate interface.

7.2 Mathematical model

There is a substantial difference in the drainage/imbibition of foam in the case of a free drainage (for example, foam placed on a solid substrate) and a drainage/imbibition of a foam placed on a porous substrate. In both cases the drainage is caused by the action of both gravity and the capillary forces. However, if foam is initially wet enough, then sooner or later the drainage/imbibition results in a formation of a free water layer under the foam and the water content in the foam layer immediately above the free water layer reaches the rigidity limit[165] which for 3D mono-disperse foam can be estimated as 0.36 corresponding to random packing limit for spherical particles.[166] Sometimes the maximum liquid fraction is estimated

as 0.26, what correspond to the minimum possible voids content at hexagonal packing of equal spheres.[73] The latter value is accepted below. The equilibrium distribution of the water contents in the foam in the end of a free drainage is well known.[73, 85, 146] Important to notice that even in a relatively thin foam layer, the water content distribution is non-uniform over the foam height: from the highest possible at the bottom to the lowest at the top.

The scenario is substantially different in the case of foam placed on a porous substrate: (i) the presence of unsaturated pores inside the porous layer results in an imbibition of water from the Plateau channels into the pores, i.e. drainage/imbibition proceeds faster and (ii) this results in a drier foam layer in contact with a porous substrate and close to the end of the drainage/imbibition process the liquid volume fraction will become lower as compared with the free drainage and below some final value. The final value can be characterised as follows: if the water contents is above this final value then the pressure inside the Plateau channels is positive, that is, the liquid will flow from the Plateau channels to outside. If the final value of the water content is reached then by further drainage the pressure inside the Plateau channels becomes smaller than the capillary pressure inside the pores of the porous substrate and the drainage stops. The previous consideration shows that the final equilibrium distribution of water content over the foam height is lower in the case of drainage/imbibition in contact with the porous substrate than in the case of a free drainage over a non-porous substrate.

7.2.1 Flow inside foam

As can be seen in Fig. 7.1, let us consider a foam composed of bubbles of uniform size (radius of R_b) with Kelvin structure[73]. It is placed on a horizontal porous substrate with pores size of R_{pm}. Drainage occurs in the vertical direction along the co-ordinate axis z directed downward, with z=0 at the top of the foam. The foam height is supposed to be constant equal to H and L is the penetration depth of liquid into the porous medium. The porous medium is supposed to be infinite at the bottom. Therefore, liquid always penetrate from foam into the porous medium and reverse imbibition cannot occur. It is assumed also that the bubble size remains constant during the drainage.

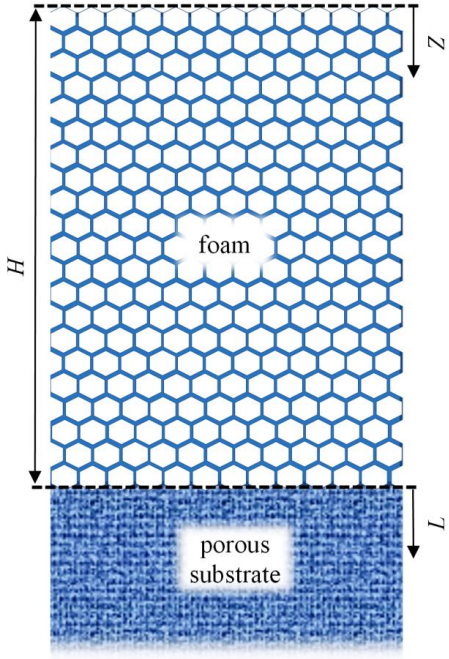

Figure 7.1: Schematic diagram of a foam placed on a porous medium. Reproduced with permission from Ref.[164]. Copyright © 2015 EDP Sciences, Springer-Verlag.

Below we use the model of Plateau borders mediated foam drainage (produced from Newtonian solutions) where the dissipation in the nodes is neglected. In this case the drainage kinetics can be described by the following equation:[85]

$$\frac{\partial A}{\partial t}+\frac{\partial}{\partial z}\left[\frac{1}{3\mu f}\left(\rho g A^{2}-C\gamma\frac{\sqrt{A}}{2}\frac{\partial A}{\partial z}\right)\right]=0\,, \tag{7.1}$$

where μ is the dynamic viscosity of liquid, which foam is built of, f ~49, $A(z, t)$ is the Plateau border cross-section at position z and time t; ρ and g are the liquid density and the gravity acceleration, respectively; $C^2=\sqrt{3}-\pi/2\sim0.161$ is a geometrical constant related to the triangular form of the Plateau border cross section, and γ is the liquid-air interfacial tension. In Eq. (7.1) the first term in parentheses describes the contribution of the gravitation and the second term is the contribution of the capillary forces to the drainage.

According to Ref.[73]

$$R_{pb}=R_b\sqrt{\frac{\varphi C_1}{C^2}} \tag{7.2}$$

or

$$A = C_1 \varphi R_b^2 , \tag{7.3}$$

where R_b and R_{pb} are the radii of the bubble and Plateau border, respectively, φ is liquid volume fraction and C_1 is a geometrical coefficient, C_1~0.4857 for a foam with Kelvin structure.[73]

Substitution of Eq. (7.3) into Eq. (7.1) results in the following equation for the liquid volume fraction φ:

$$\frac{\partial \varphi}{\partial t} + \frac{\partial}{\partial z}\left(\frac{C_1 \rho g R_b^2}{3\mu f} \varphi^2 - \frac{C\sqrt{C_1}\gamma R_b}{6\mu f} \sqrt{\varphi} \frac{\partial \varphi}{\partial z} \right) = 0 . \tag{7.4}$$

Let us introduce the following dimensionless variable and co-ordinate: $\zeta \to z/H, \quad \tau \to t/t_0, \quad \phi \to \varphi/\varphi_{cr}$, where H is the foam height, t_0 is the time scale of the process to be determined below and φ_{cr} is the liquid volume fraction after the pressure inside the Plateau channels and the pressure inside the porous substrate equilibrate. Substitution of these variables into Eq. (7.4) results in

$$\frac{\partial \phi}{\partial \tau} + \frac{\partial}{\partial \zeta}\left(\frac{t_0 C_1 \rho g R_b^2 \varphi_{cr}}{3\mu f H} \phi^2 - \frac{t_0 C\sqrt{C_1}\gamma R_b \sqrt{\varphi_{cr}}}{6\mu f H^2} \sqrt{\phi} \frac{\partial \phi}{\partial \zeta} \right) = 0 , \tag{7.5}$$

There are two dimensionless parameters in the latter equation. Their ratio is $\frac{t_0 C_1 \rho g R_b^2 \varphi_{cr}}{3\mu f H} / \frac{t_0 C\sqrt{C_1}\gamma R_b \sqrt{\varphi_{cr}}}{6\mu f H^2} = \frac{2\rho g R_b H \sqrt{C_1}}{C\gamma} \sqrt{\varphi_{cr}}$. The latter means that if we select the characteristic time scale from the following condition: $\frac{t_0 C\sqrt{C_1}\gamma R_b \sqrt{\varphi_{cr}}}{6\mu f H^2} = 1$, then:

$$t_0 = \frac{6\mu f H^2}{C\sqrt{C_1}\gamma R_b \sqrt{\varphi_{cr}}} , \tag{7.6}$$

Substitution of Eq. (7.6) into Eq. (7.5) results in

$$\frac{\partial \phi}{\partial \tau} + \frac{\partial}{\partial \zeta}\left(\frac{2\rho g R_b H \sqrt{C_1}}{C\gamma} \sqrt{\varphi_{cr}} \phi^2 - \sqrt{\phi} \frac{\partial \phi}{\partial \zeta} \right) = 0 . \tag{7.7}$$

Assuming that the liquid films between bubbles in foam are flat (i.e. in a dry foam, $R_b >> R_{pb}$) the pressure in all bubbles is identical[167] and equals to:

$$P_b = P_a + \frac{4\gamma}{R_b}, \tag{7.8}$$

where P_a is the atmospheric pressure. The pressure in the Plateau border is lower than that in the bubbles on the value of the capillary pressure:[167]

$$P_c = \frac{\gamma}{R_{pb}}, \tag{7.9}$$

From Eqs. (7.2), (7.8) and (7.9) the pressure in the Plateau border is

$$P_{pb}(z,t) = P_a + \frac{\gamma}{R_b}\left(4 - \frac{C}{\sqrt{C_1\varphi(z,t)}}\right). \tag{7.10}$$

Let us introduce P_{pm} as the mean capillary pressure inside capillaries in the porous substrate, which can be estimated by $P_{pm} \sim n\gamma/R_{pm}$, where R_{pm} is radius of pores, n =1 in the case of porous media built by cylinders and n=2 in the case of two dimensional geometry. Accordingly, the pressure difference, which results in the liquid flow from the Plateau channel into the porous substrate at the foam/porous substrate interface, will be

$$\Delta P = P_{pb} - P_{pm} = \frac{\gamma}{R_b}\left(4 - \frac{C}{\sqrt{C_1\varphi(z=H,t)}}\right) + \frac{n\gamma}{R_{pm}}. \tag{7.11}$$

If $\Delta P > 0$, then liquid from the Plateau border will penetrate into the porous substrate. If $\Delta P < 0$, then penetration will not happen. The latter consideration and Eq. (7.11) determine the final liquid content, when $\Delta P=0$:

$$\frac{\gamma}{R_b}\left(4 - \frac{C}{\sqrt{C_1\varphi_{cr}}}\right) + \frac{n\gamma}{R_{pm}} = 0 \tag{7.12}$$

Hence,

$$\varphi_{cr} = \frac{\left(\frac{C^2}{16C_1}\right)}{\left(1 + \frac{nR_b}{4R_{pm}}\right)^2} \tag{7.13}$$

If we introduce α as a ratio of capillary pressure in the porous substrate to capillary pressure in the bubbles:

$$\alpha = \frac{\Delta P_{\text{cap in substrate}}}{\Delta P_{\text{cap in bubbles}}} = \frac{\frac{n\gamma}{R_{pm}}}{\frac{4\gamma}{R_b}} = \frac{nR_b}{4R_{pm}}, \tag{7.14}$$

then, Eq. (7.13) can be rewritten as:

$$\varphi_{cr} = \frac{\left(\frac{C^2}{16C_1}\right)}{(1+\alpha)^2} \tag{7.15}$$

Substitution of expression (7.13) into Eq. (7.6) results in the following expression for the characteristic time of the foam drainage:

$$t_0 = \frac{6\mu f H^2}{C^2\gamma}\left(\frac{4}{R_b} + \frac{n}{R_{pm}}\right). \tag{7.16}$$

If we introduce Bond number as a ratio of hydrostatic pressure in foam to capillary pressure in bubbles:

$$Bo = \frac{\Delta p_{grav}}{\Delta p_{cap}} = \frac{\rho g H}{\frac{4\gamma}{R_b}}, \tag{7.17}$$

then substitution of Eq. (7.13) into Eq. (7.7) results in the following dimensionless equation for the foam drainage:

$$\frac{\partial \phi}{\partial \tau} + \frac{\partial}{\partial \zeta}\left(2\frac{Bo}{1+\alpha}\phi^2 - \sqrt{\phi}\frac{\partial \phi}{\partial \zeta}\right) = 0. \tag{7.18}$$

7.2.2 Liquid imbibition into porous substrate

The kinetics of imbibition of a liquid into a porous substrate is described by the Darcy's equation:

$$Q_{pm} = \frac{\kappa}{\mu}\frac{\Delta P}{L} \tag{7.19}$$

and

$$\varepsilon\frac{dL}{dt} = \frac{\kappa}{\mu}\frac{\Delta P}{L}, \tag{7.20}$$

where Q_{pm} is the flux of the liquid inside the porous substrate, ε is the porosity, L is the depth of the wetted part inside the porous layer, κ is permeability of the porous substrate, ΔP is the pressure difference causing the liquid imbibition, according to Eq. (7.11). Substitution of Eq. (7.11) into Eq. (7.20) results in

$$\varepsilon \frac{dL}{dt} = \frac{\kappa}{\mu} \frac{\frac{\gamma}{R_b}\left(4 - \frac{C}{\sqrt{C_1 \varphi(z=H,t)}}\right) + \frac{n\gamma}{R_{pm}}}{L(t)}, \quad L(0) = 0 . \tag{7.21}$$

Let us introduce the following dimensionless variables: $l \to L/L_0, \quad \tau \to t/t_0, \quad \phi \to \varphi/\varphi_{cr}$, where L_0 is the characteristic depth of penetration which is defined as:

$$L_0 = 2\sqrt{\frac{\kappa \gamma t_0}{\varepsilon \mu R_b}(1+\alpha)}, \tag{7.22}$$

and t_0 and φ_{cr} are defined by Eqs. (7.16) and (7.15), respectively. Now Eq. (7.21) can be rewritten as:

$$\frac{dl}{d\tau} = \frac{\left(1 - \frac{1}{\sqrt{\phi(\zeta=1,\tau)}}\right)}{l(\tau)}, \quad l(0) = 0 . \tag{7.23}$$

The above dimensionless equation describes the kinetics of liquid penetration into the porous substrate.

7.2.3 Foam/porous substrate interface

The boundary condition at the foam/porous substrate interface is a mass conservation of the liquid in the case when the free liquid layer does not form:

$$Q_f = Q_{pm}, \tag{7.24}$$

where Q_f is the flux of liquid from foam to the interface. It can be concluded using Eq. (7.4):

$$Q_f = \frac{C_1 \rho g R_b^2}{3\mu f} \varphi^2(z=H,t) - \frac{\sqrt{C_1} C \gamma R_b}{6\mu f} \sqrt{\varphi(z=H,t)} \frac{\partial \varphi(z=H,t)}{\partial z} . \tag{7.25}$$

On the other hand, from Eqs. (7.19) and (7.11), the flux of liquid from interface into the porous substrate is:

$$Q_{pm} = \frac{\kappa}{\mu} \frac{\frac{\gamma}{R_b}\left(4 - \frac{C}{\sqrt{C_1 \varphi(z=H,t)}}\right) + \frac{n\gamma}{R_{pm}}}{L(t)} . \tag{7.26}$$

Substitution of Eqs. (7.25) and (7.26) into Eq. (7.24) results in the following expression for the mass conservation of the liquid at the interface (no free liquid film):

$$\frac{C_1 \rho g R_b^2}{3\mu f}\varphi^2(H,t) - \frac{\sqrt{C_1} C \gamma R_b}{6\mu f}\sqrt{\varphi(H,t)}\frac{\partial \varphi(H,t)}{\partial z} = \frac{\kappa}{\mu}\frac{\frac{\gamma}{R_b}\left(4 - \frac{C}{\sqrt{C_1 \varphi(H,t)}}\right) + \frac{n\gamma}{R_{pm}}}{L(t)}. \qquad (7.27)$$

Using dimensionless variables and co-ordinate as before: $\zeta \to z/H, \quad l \to L/L_0, \quad \tau \to t/t_0, \quad \phi \to \varphi/\varphi_{cr}$, Eq. (7.27) can be rewritten as:

$$2\frac{Bo}{1+\alpha}\phi^2(1,\tau) - \sqrt{\phi(1,\tau)}\frac{\partial \phi(1,\tau)}{\partial \zeta} = \left(\frac{16C_1}{C^2}\right)\varepsilon(1+\alpha)^2\frac{L_0}{H}\frac{\left(1 - \frac{1}{\sqrt{\phi(1,\tau)}}\right)}{l(\tau)}. \qquad (7.28)$$

Substituting Eq. (7.22) into Eq. (7.28) and introducing Darcy number as:

$$Da = \frac{n^2 \kappa}{R_{pm}^2} \qquad (7.29)$$

results in the following dimensionless equation for the conservation of liquid at the interface:

$$2\frac{Bo}{1+\alpha}\phi^2(1,\tau) - \sqrt{\phi(1,\tau)}\frac{\partial \phi(1,\tau)}{\partial \zeta} = C_2\sqrt{\varepsilon Da}\frac{(1+\alpha)^3}{\alpha}\frac{\left(1 - \frac{1}{\sqrt{\phi(1,\tau)}}\right)}{l(\tau)} \qquad (7.30)$$

where $C_2 = 16C_1\sqrt{6f}/C^3 \sim 2057.8$.

Let us use the Kozeny-Carman[168] model of the capillary tubes as the porous medium in the present study. According to Ref.[168], the permeability of this model can be found by the following equation:

$$\kappa = \frac{\varepsilon}{k_z S_{pv}^2} \qquad (7.31)$$

where k_z and S_{pv} are Kozeny constant and specific surface area per unit pore volume, respectively. For cylindrical pore shape k_z=2 and S_{pv}=2/R_{pm}.[169] Although this model ignores the tortuous character of the flow paths in real porous media, the advantage of using this model, is its simplicity and clarity. Substituting Eq. (7.31) into Eq. (7.30) leads to the following expression for the continuity of liquid at the interface:

$$2\frac{Bo}{1+\alpha}\phi^2(1,\tau) - \sqrt{\phi(1,\tau)}\frac{\partial \phi(1,\tau)}{\partial \zeta} = C_3\varepsilon\frac{(1+\alpha)^3}{\alpha}\frac{\left(1 - \frac{1}{\sqrt{\phi(1,\tau)}}\right)}{l(\tau)} \qquad (7.32)$$

where $C_3 = 8C_1\sqrt{3f}\,/C^3 \sim 727.5$.

The suggested system of equations (7.18), (7.23) with boundary condition (7.32) is valid only when no liquid layer is formed at foam/substrate interface, i.e. if $\varphi(H,t) < \varphi_{\max}$. In this case porous substrate sucks all liquid coming from the foam.

7.2.4 Accumulation of liquid layer

If the liquid volume fraction at foam/porous substrate interface reaches the maximum limiting value, $\varphi_{\max}$, the accumulation of liquid layer starts (at the moment $t=t_m$) and free liquid layer is formed in between the porous substrate and the foam. This situation continues until $t=t_M$ when porous substrate sucks the liquid above the layer and again all liquid coming from the foam goes directly into the porous substrate. Therefore, the boundary condition at the bottom of the foam is constant liquid volume fraction at $t_m < t < t_M$:

$$\varphi(H,t) = \varphi_{\max}, \tag{7.33}$$

and in dimensionless form at $\tau_m < \tau < \tau_M$:

$$\phi(1,\tau) = \phi_{\max}, \tag{7.34}$$

where $\varphi_{\max}$~0.26, $\tau_m = t_m/t_0$, $\tau_M = t_M/t_0$ and $\phi_{\max} = \varphi_{\max}/\varphi_{cr}$. The boundary condition (7.33) or (7.34) is valid until the moment t_M and afterwards the condition (7.32) is again satisfied.

In the case of liquid accumulation at foam/porous substrate interface, a mass balance of liquid leads to the following equation for the thickness of film in between the foam and the porous substrate:

$$\frac{dh}{dt} = \frac{C_1\rho g R_b^2}{3\mu f}\varphi^2(z=H,t) - \frac{\sqrt{C_1}C\gamma R_b}{6\mu f}\sqrt{\varphi(z=H,t)}\,\frac{\partial\varphi(z=H,t)}{\partial z} - \frac{\kappa}{\mu}\frac{\dfrac{\gamma}{R_b}\left(4 - \dfrac{C}{\sqrt{C_1\varphi(z=H,t)}}\right) + \dfrac{n\gamma}{R_{pm}}}{L(t)}, \tag{7.35}$$

where h is the thickness of the liquid layer. It is assumed in Eq. (7.35) that the thickness of liquid layer, $h(t)$, is so small and the pressure inside the film remains constant and is equal to that given by Eq. (7.10).

We use below the following dimensionless variables and co-ordinate: $\lambda \to h/h_0$, $\zeta \to z/H$, $l \to L/L_0$, $\tau \to t/t_0$, $\phi \to \varphi/\varphi_{cr}$, where h_0 is the characteristic thickness of liquid layer which is determined as:

$$h_0 = \frac{4\kappa\gamma t_0}{\mu R_b L_0}(1+\alpha) = 2\sqrt{\frac{\varepsilon\kappa\gamma t_0}{\mu R_b}(1+\alpha)} = \varepsilon L_0 . \qquad (7.36)$$

Using the above expression, Eq. (7.35) can be rewritten as:

$$C_3\varepsilon\frac{(1+\alpha)^3}{\alpha}\frac{d\lambda}{d\tau} = 2\frac{Bo}{1+\alpha}\phi^2(1,\tau) - \sqrt{\phi(1,\tau)}\frac{\partial\phi(1,\tau)}{\partial\zeta} - C_3\varepsilon\frac{(1+\alpha)^3}{\alpha}\frac{\left(1-\frac{1}{\sqrt{\phi(1,\tau)}}\right)}{l(\tau)} . \qquad (7.37)$$

The suggested system of Eqs. (7.18), (7.23) and boundary condition (7.32) in the case no liquid layer is formed over porous substrate or conditions (7.32), (7.34) and (7.37) in the case of liquid accumulation at the foam-porous substrate interface include three dimensionless parameters: Bo, α (according to Eq. (7.15)) and the porosity of the porous substrate, ε.

7.2.5 Model calculation

The model of foam drainage/imbibition described by dimensionless Eq. (7.18) has been solved below using finite element method on one dimensional regular grid with 50000 elements corresponding to the foam height. The model of liquid imbibition into porous substrate described by Eq. (7.23) was coupled with foam drainage equation at foam/substrate interface. A backward differentiation formula was used to solve time-dependent variables and time stepping was free taken by solver with initial step size of 10^{-20}. Relative tolerance was set to 10^{-6}, whereas absolute tolerance was set to 10^{-8}. The boundary condition at the top of the foam was zero liquid flux. The boundary condition at foam/porous substrate interface was continuity of flux, Eq. (7.32), in case no liquid layer is formed over porous substrate or the combination of conditions (7.32), (7.34) and (7.37) in case of liquid layer accumulation. According to Eqs. (7.18), (7.23), (7.32), (7.34) and (7.37) kinetics of foam drainage/imbibition depends on three dimensionless numbers: Bo, α and ε. Furthermore, the initial value of liquid volume fraction in foam, $\varphi(z, 0)$, was set to

be varied in simulations in order to investigate its effect on the kinetics of foam drainage/imbibition.

7.3 Results and discussion

The typical time evolution of the liquid volume fraction, φ, over the dimensionless foam height, ζ, and time evolution of the depth of imbibition into the porous medium, l, is shown in Fig. 7.2. In the very beginning of the drainage/imbibition the liquid volume fraction decreases only at the top of the foam and near foam/porous substrate interface, whereas in the middle part of the foam the initial value is retained. This is a common feature of foam drainage/imbibition process below. In contrast to the foam placed on a layer of liquid or on a non-porous substrate, the liquid volume fraction at the interface with porous substrate decreases dramatically over a very short time due to imbibition into pores of the porous substrate. After initial considerable decrease in the liquid volume fraction near the interface the difference in the capillary pressure between foam and porous substrate decreases, whereas the penetration depth of the liquid into substrate increases and therefore, according to Eq. (7.23), the imbibition becomes slower. At the same time there is a continuous supply of liquid to this region from the higher parts of the foam. That is why the further decrease in the liquid volume fractions slows down and in some cases after initial drop; the liquid volume fraction starts to increase and experiences a peak point (see τ=0.002 in Fig. 7.2(a)). This process is controlled by Bond number, α, ε and initial liquid volume fraction, $\varphi(z, 0)$. In addition, as is shown in Fig. 7.2(b), in the beginning of the drainage the liquid penetrate into the porous substrate with a higher rate while after a short period of time the depth of liquid imbibition increases very gradually and it plateaus at a maximum value.

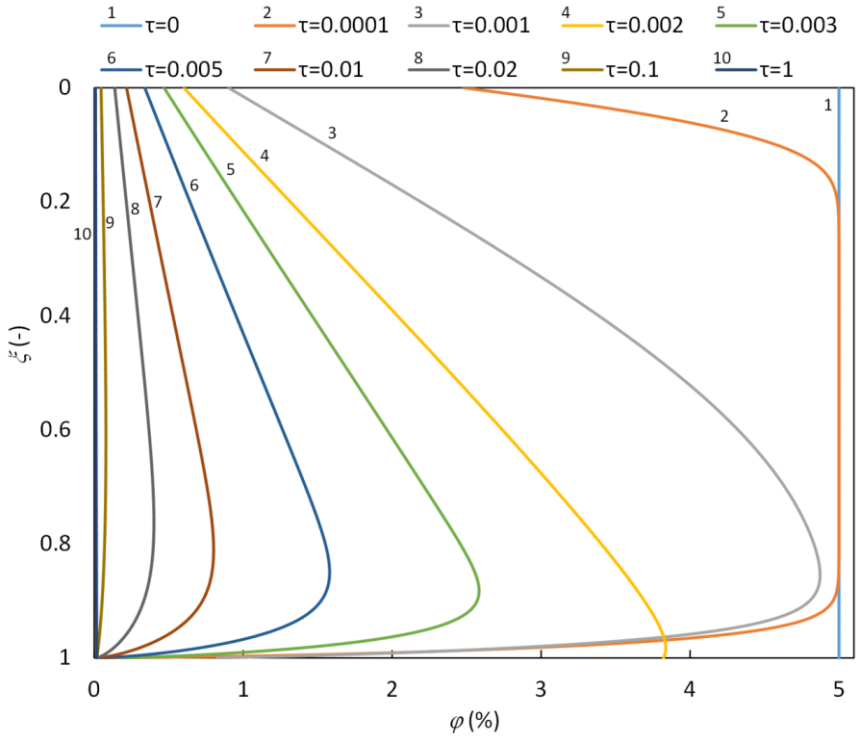

a)

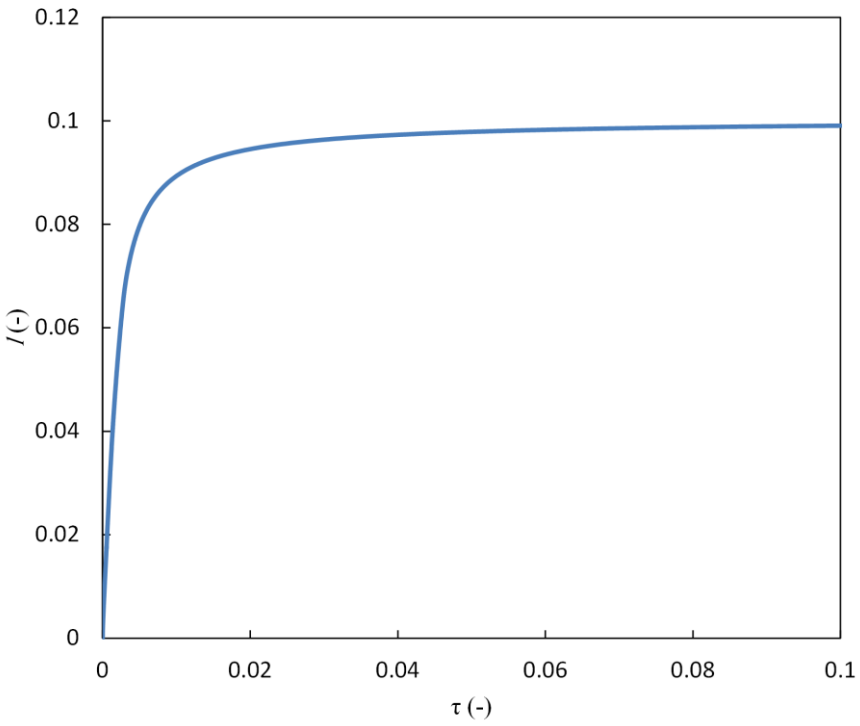

b)

Figure 7.2: Time evolution of a) liquid volume fraction over the foam height b) liquid imbibition into the porous medium at Bo=5.45, α=10, ε=0.03 and $\varphi(z, 0)$= 5%.[148] Reproduced by permission of The Royal Society of Chemistry. Copyright © 2016 Royal Society of Chemistry.

Fig. 7.3 shows the time evolution of the liquid volume fraction at foam/porous substrate interface $\varphi(\zeta=1,\tau)$ at various Bo, α and ε numbers, and with various initial liquid volume fractions, $\varphi(z, 0)$. Based on the value of Bo, α, ε and $\varphi(z, 0)$, there are three possible scenarios for the interaction of foam with a porous substrate.

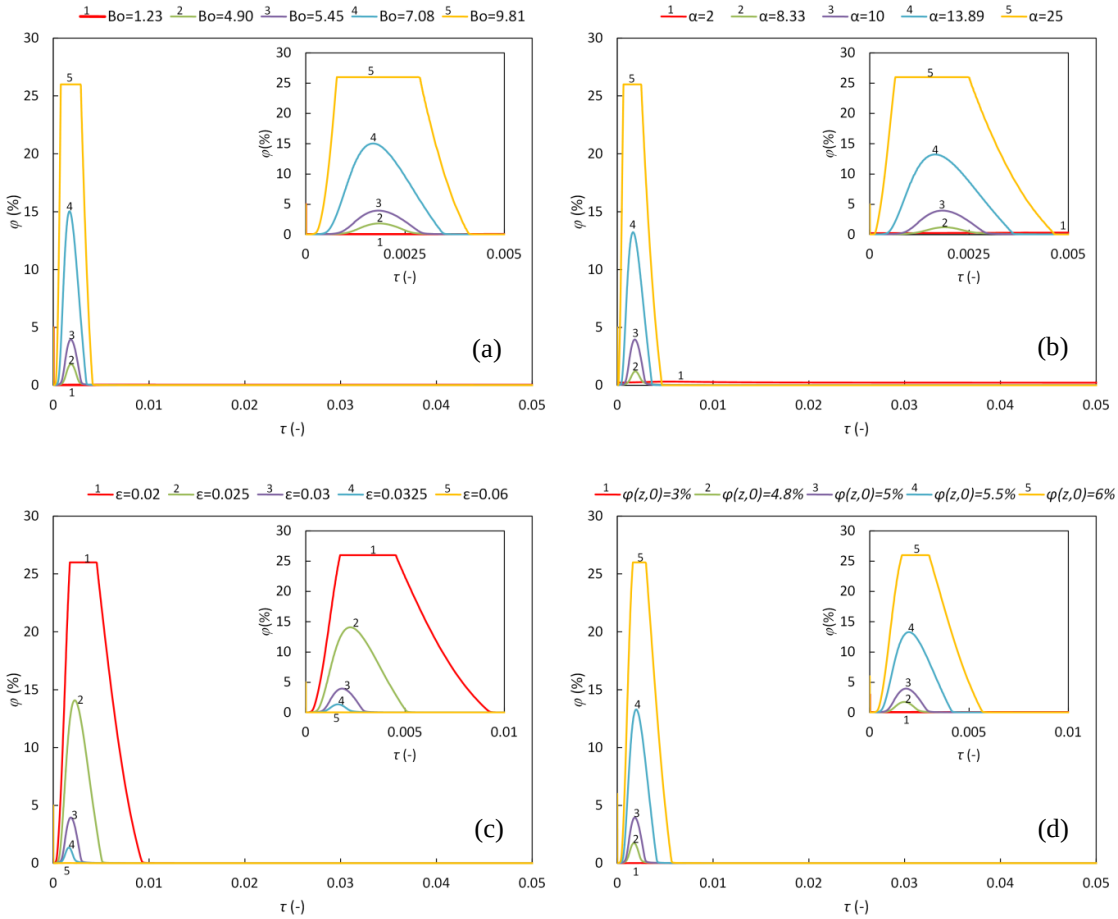

Figure 7.3: Time evolution of liquid volume fraction at foam/porous substrate interface at a) α=10, ε=0.03, $\varphi(z, 0)$=5% and various Bo; b) Bo=5.45, ε=0.03, $\varphi(z, 0)$=5% and various α; c) Bo=5.45, α=10, $\varphi(z, 0)$=5% and various ε; d) Bo=5.45, α=10, ε=0.03 and various $\varphi(z, 0)$. In all cases inserts present enlarged region of time scales from 0 to 0.005-0.01. Note, in Figure 7.3 the first very fast stage when the liquid volume fraction at the foam/porous substrate interface decreases cannot be clearly shown but it is present in all cases considered.[148] Reproduced by permission of The Royal Society of Chemistry. Copyright © 2016 Royal Society of Chemistry.

7.3.1 Rapid imbibition

As shown in Fig. 7.3 $\varphi(\zeta=1,\tau)$ is a decreasing function of time at low Bo, α and $\varphi(z, 0)$, and high porosity values, ε (e.g. Bo=1.23 in Fig. 7.3(a), α=2 in Fig. 7.3(b), ε=0.06 in Fig. 7.3(c) and $\varphi(z, 0)$=3% in Fig. 7.3(d)). In these cases, liquid imbibition into porous substrate occurs quicker as compared with the liquid drainage inside the foam, and liquid volume fraction at the interface does not experience a peak point after initial considerable decrease and it remains constant near final liquid volume fraction. This regime, when the imbibition into porous substrate dominates, is referred to as a *rapid imbibition*.

Fig. 7.4 shows the time evolution of liquid volume fraction over the foam height at low values of Bo, α and $\varphi(z, 0)$ and high value of porosity, corresponding to the regime of rapid imbibition. Bond number is a ratio of hydrostatic pressure in foam to capillary pressure in bubbles as is defined by Eq. 7.17. Accordingly, at lower Bond numbers, the capillary forces in foam dominate the gravitational forces acting downward and thus, liquid drainage due to gravity occurs slower than the imbibition into the pores of porous substrate. Therefore, Figs. 7.2(a) and 7.4(a) show the considerable difference: at identical α, ε and $\varphi(z, 0)$, the liquid supply from higher parts of the foam occurs slower at low Bo numbers (Fig. 7.4(a) as compared with that in Fig. 7.2(a)). α is a ratio of bubbles radius to the radius of pores according to Eq. 7.14. At low α numbers, the drainage at the top of the foam proceed slower while the capillary suction imposed by the porous substrate is not considerable also. Therefore, at identical Bo, ε and $\varphi(z, 0)$, the liquid supply from higher parts of foam occurs slower at lower α numbers (Fig. 7.4(b) as compared with that in Fig. 7.2(a)). It is also possible to conclude from both Fig. 7.4(b) and Eq. 7.15 that final liquid volume fraction is higher at lower values of α. Comparison of Figs. 7.4(c) and 7.4(d) with Fig. 7.2(a) demonstrates that at higher values of ε and lower values of $\varphi(z, 0)$, the liquid volume fraction at the bottom of the foam does not experience a peak point and it remains constant near final liquid volume fraction.

In all three plots presented in Figs. 7.4(a)- 7.4(d) the liquid volume fraction reaches maximum value somewhere inside the foam, while the liquid volume fraction decreases close both the top and the bottom of the foam. However, there is one important difference between plots presented in Fig. 7.4(a) as compared with other plots (Figs. 7.4(b), 7.4(c) and 7.4(d)): position of the maximum is close to the middle of the foam on all plots in Fig 7.4(a) while it is closer to the bottom of the foam in Figs. 7.4(b), 7.4(c) and 7.4(d).

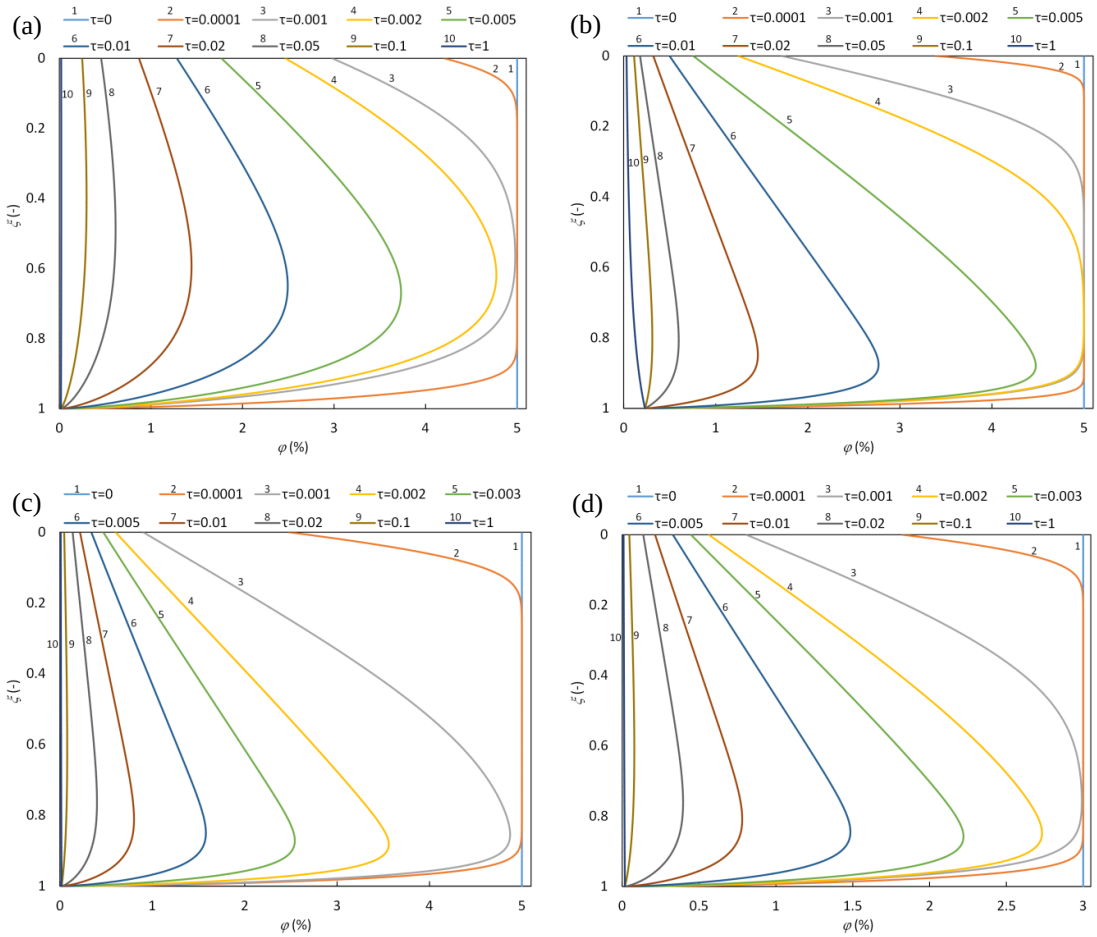

Figure 7.4: Time evolution of liquid volume fraction over the foam height at a) Bo=1.23, α=10, ε=0.03 and $\varphi(z, 0)$=5%; b) Bo=5.45, α=2, ε=0.03 and $\varphi(z, 0)$=5%; c) Bo=5.45, α=10, ε=0.06 and $\varphi(z, 0)$=5%; d) Bo=5.45, α=10, ε=0.03 and $\varphi(z, 0)$=3%.[148] Reproduced by permission of The Royal Society of Chemistry. Copyright © 2016 Royal Society of Chemistry.

7.3.2 Intermediate imbibition

Fig. 7.3 shows that $\varphi(\zeta=1,\tau)$ experiences a maximum value at intermediate Bo, α, ε and $\varphi(z, 0)$ numbers (e.g. Bo=4.90, 5.45 and 7.08 in Fig. 7.3(a), α=8.33, 10 and 13.89 in Fig. 7.3(b), ε=0.025, 0.03 and 0.0325 in Fig. 7.3(c) and $\varphi(z, 0)$=4.8, 5 and 5.5% in Fig. 7.3(d)). This regime, when the rate of the imbibition into the porous substrate is comparable with the rate of drainage, is referred to as an *intermediate imbibition*. Accordingly, as shown in Fig. 7.2(a) the liquid supply from higher parts of foam to the interface occurs quicker, whereas liquid penetration from interface into the porous substrate goes slower at the beginning of the process but the

imbibition is faster during the final stage of the process. That is why at the early stage of the drainage/imbibition, liquid volume fraction at the bottom of the foam reaches a maximum value and then it drops to approximately final value. Note that at this regime, there is not any liquid accumulation between the foam and the porous substrate.

7.3.3 Slow imbibition

The system switched to a different regime at high Bo, α and $\varphi(z, 0)$, and low ε values (e.g. Bo=9.81 in Fig. 7.3(a), α=25 in Fig. 7.3(b), ε=0.02 in Fig. 7.3(c) and $\varphi(z, 0)$=6% in Fig. 7.3(d)). This regime, when the liquid volume fraction at the foam/porous substrate interface can increase to a maximum limiting value and free liquid layer is formed over the porous substrate, is referred to as a *slow imbibition*.
Fig. 7.5 shows the time evolution of liquid volume fraction over the foam height in the case of slow imbibition regime, which happens at high values of Bo, α and $\varphi(z, 0)$ and low values of ε, correspondingly. At slow imbibition regime the liquid supply from higher parts of the foam occurs quicker as compared with liquid imbibition into the porous substrate. Accordingly, $\varphi(\zeta=1,\tau)$ reaches the maximum limiting value, $\varphi_{\max}$, at $\tau=\tau_m$ and free liquid layer starts to accumulate between the porous substrate and the foam. Time evolution of the thickness of the free liquid layer is shown in Fig. 7.6 for Bo=9.81, α=10, ε=0.03 and $\varphi(z, 0)$=5%. The thickness of the free liquid layer increases and reaches a maximum value and then it decreases until the moment $\tau=\tau_M$ when free liquid layer disappears and it is sucked completely by the porous substrate. After that at $\tau>\tau_M$ again all liquid coming from the foam goes directly into the porous substrate and $\varphi(\zeta=1,\tau)$ also drops to approximately final liquid volume fraction (See Fig. 7.3). Fig. 7.5 shows that the drainage at the top of the foam is practically uncorrelated with processes near foam/porous substrate interface.

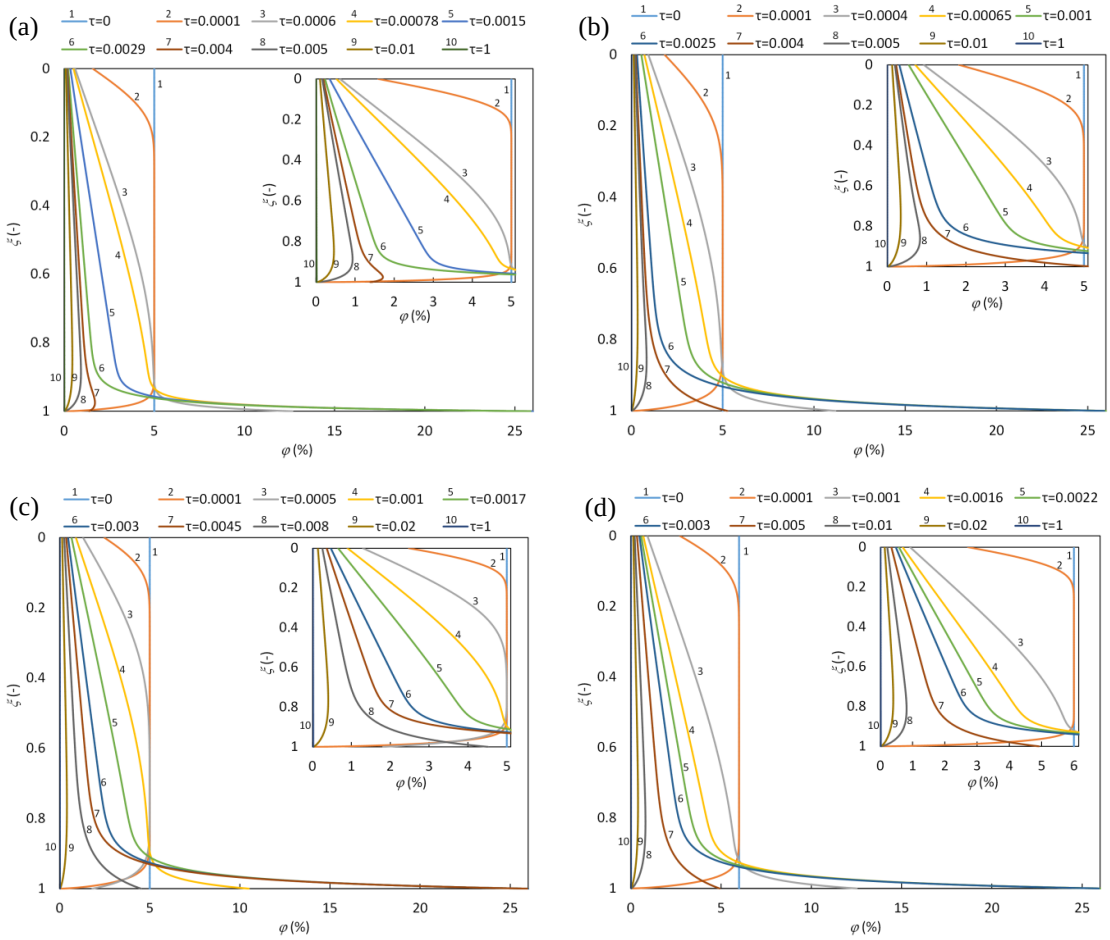

Figure 7.5: Time evolution of liquid volume fraction over the foam height at a) Bo=9.81, α=10, ε=0.03 and $\varphi(z, 0)$=5%; b) Bo=5.45, α=25, ε=0.03 and $\varphi(z, 0)$=5%; c) Bo=5.45, α=10, ε=0.02 and $\varphi(z, 0)$=5%; d) Bo=5.45, α=10, ε=0.03 and $\varphi(z, 0)$=6%. In all cases inserts present enlarged region of liquid content from 0 to 5-6%.[148] Reproduced by permission of The Royal Society of Chemistry. Copyright © 2016 Royal Society of Chemistry.

Note, there is a difference in time dependencies presented in Fig. 7.5(a) from those presented in Figs. 7.5(b)- 7.5(d): at the moment τ=0.004 (just after the free liquid layer disappeared) the dependency of the liquid volume fraction on the foam height has a s-shape character, which is different from all other dependences presented in Figs. 7.5(b)- 7.5(d).

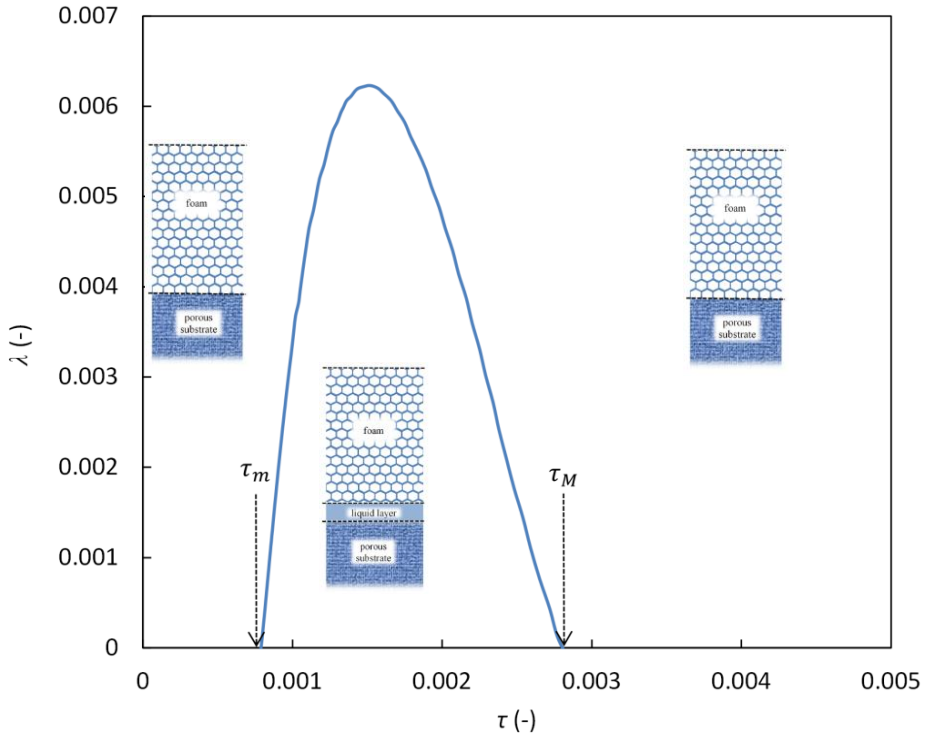

Figure 7.6: Time evolution of the thickness of free liquid layer between foam and porous substrate at Bo=9.81, α=10, ε=0.03 and $\varphi(z, 0)$=5% (corresponds to Fig. 7.5(a)).[148] Reproduced by permission of The Royal Society of Chemistry. Copyright © 2016 Royal Society of Chemistry.

7.3.4 Transition points between three regimes of drainage/imbibition

It was shown earlier that the kinetics of foam drainage/imbibition depends on the values of four parameters: Bo, α, ε, and $\varphi(z, 0)$. Below we try to find relations between these four parameters, which determine transitions between three different regimes of the drainage/imbibition process. At a very early stage of the drainage/imbibition, the liquid volume fraction at the foam/porous substrate interface drops from its initial value to roughly final liquid volume fraction and then based on the drainage/imbibition regime it experiences a peak point or remains constant near final value (see discussion of the results presented in Fig. 7.3). However, even in the fast imbibition regime, there is also a weak peak point, but its value is very close to final liquid volume fraction. If we adopt $\phi(1,\tau)=3$ or $\varphi(H,t)=3\varphi_{cr}$ as a transition point between rapid and intermediate imbibition regimes, using the regression analysis between various simulations we reach the following

dimensionless number which determines the boundary between rapid and intermediate imbibition regimes:

$$RI = \frac{Bo^{1.34}\varphi_0^{3.75}}{\varepsilon^{2.56}} \frac{(1+\alpha)^{2.94}}{\alpha} \approx 19. \quad (7.38)$$

If RI < 19, then the rapid imbibition regime of drainage/imbibition takes place. According to Eq. (7.33) a transition between intermediate and slow imbibition regime occurs at $\varphi(H,t) = \varphi_{max} = 0.26$. Therefore, the same procedure as above allows finding another dimensionless number, IS, which determine the boundary between intermediate and slow imbibition regimes:

$$IS = \frac{Bo^{1.34}\varphi_0^{3.75}}{\varepsilon^{2.56}} \frac{(1+\alpha)^{2.05}}{\alpha} \approx 35. \quad (7.39)$$

At IS > 35, the liquid volume fraction at the foam/porous substrate interface reaches the maximum limiting value and free liquid layer is formed over the porous substrate (slow imbibition). However, at RI > 19 and IS < 35 the system is in intermediate imbibition regime and no liquid layer is formed at the interface.

7.4 Conclusions

A model for foam drainage/imbibition placed on a porous substrate was introduced, which allows describing three different regimes of the process. According to suggested mathematical model, kinetics of foam drainage/imbibition depends on three dimensionless numbers: the ratio of capillary pressure in porous substrate to that in bubbles, α, porosity of the porous substrate, ε, Bond number, Bo, and initial liquid volume fraction, $\varphi(z, 0)$. It was found that there are three different regimes of the drainage/imbibition. All three regimes of drainage/imbibition start with a very fast decrease of the liquid volume fraction at the foam/porous substrate interface. All processes are considered after this short initial stage. At low Bo, α and $\varphi(z, 0)$, and relatively high ε values liquid imbibition into the porous substrate occurs faster as compared with the liquid drainage inside the foam. This case was referred to as a *rapid imbibition*. During foam drainage/imbibition at the rapid imbibition regime, the liquid volume fraction at the bottom of the foam remains almost constant close to a final liquid volume fraction after initial considerable decrease. At intermediate

Bo, α, ε and $\varphi(z, 0)$ numbers the process of drainage/imbibition switched to a different regime, when the liquid volume fraction at the foam/porous substrate interface experiences a maximum value. At this regime the rates of drainage and imbibition are comparable and this regime is referred to as an *intermediate imbibition*. At even higher Bo, α and $\varphi(z, 0)$, and lower ε values the liquid volume fraction at foam/porous substrate interface increases to a maximum limiting value and free liquid layer is formed over the porous substrate. This case is referred to as a *slow imbibition*. Applying the regression analysis between various simulation results, transition points between three different regimes of drainage/imbibition were determined by introducing two dimensionless numbers.

Nomenclature 7

A	Plateau border cross-sectional area, m^2
Bo	Bond number
C	geometrical coefficient
C_1	geometrical coefficient
C_2	coefficient
C_3	coefficient
Da	Darcy number
$,f$	drag coefficient
g	gravity acceleration, $m.s^{-2}$
h	thickness of the free liquid layer, m
h_0	characteristic thickness of the free liquid layer, m
H	foam height, m
k_z	Kozeny constant
l	dimensionless depth of penetration
L	penetration depth, m

L_0	characteristic depth of penetration, m
n	geometrical coefficient of porous substrate
P	pressure, Pa
P_a	atmospheric pressure, Pa
P_b	pressure in a bubble, Pa
P_c	pressure difference in bubble and Plateau border, Pa
P_{pb}	pressure in Plateau border, Pa
P_{pm}	pressure in porous substrate, Pa
Q	flow rate, $m^3.s^{-1}$
Q_f	flux of liquid from foam to the foam/porous substrate interface, $m.s^{-1}$
Q_{pm}	flux of liquid into the porous substrate, $m.s^{-1}$
R_b	radius of bubbles, m
R_{pb}	curvature radius of Plateau border, m
R_{pm}	radius of pores inside porous substrate, m
S_{pv}	specific surface area per unit pore volume, m^{-1}
t	time, s
t_m	time instant when a free liquid layer starts to form, s
t_M	time instant when a free liquid layer is sucked by the porous substrate, s
t_0	characteristic time scale, s
z	co-ordinate axis, m

Greek Symbols

α	ratio of capillary pressure in porous substrate to that in bubbles
γ	surface tension, $N.m^{-1}$
ε	porosity

ζ	dimensionless vertical co-ordinate
κ	substrate permeability, m^2
λ	dimensionless thickness of the free liquid layer
μ	dynamic viscosity, Pa.s
ρ	liquid density, $kg.m^{-3}$
τ	dimensionless time
τ_m	dimensionless time instant when a free liquid layer starts to form
τ_M	dimensionless time instant when a free liquid layer is sucked
φ	liquid volume fraction
φ_{cr}	final liquid volume fraction
ϕ	dimensionless liquid volume fraction

CHAPTER 8

CONCLUSIONS AND FUTURE WORK

8.1 Conclusions

The interaction of complex liquids (i.e. droplets or foams) with complex surfaces (i.e. soft deformable or porous surfaces) was addressed in the following areas: (1) wetting of deformable substrates and surface forces, (2) kinetics of wetting and spreading of non-Newtonian liquids over porous substrates, (3) kinetics of spreading of non-Newtonian solutions over hair, (4) free drainage of foams produced from non-Newtonian solutions, and (5) foam drainage placed on porous substrates.

Equilibrium of liquid droplets on deformable substrates was investigated in Chapter 3. Disjoining pressure action in the vicinity of the apparent three phase contact line was taken into account. It was shown that the combined disjoining and capillary pressure action determine the substrate deformation. A simplified linear disjoining pressure isotherm and simple Winkler's model to account for the substrate deformation were used which allows deducing analytical solutions for both the liquid profile and the substrate deformation. The apparent equilibrium contact angle of the liquid profile with the deformable substrate was calculated and its dependency on the system parameters was investigated.

Spreading/imbibition of blood, which is a power law shear thinning non-Newtonian liquid, over a dry porous layer was investigated in Chapter 4 from both theoretical and experimental points of view. It was found that blood droplet spreading/imbibition over porous substrates shows two different behaviours: (i) *partial wetting case* with three subsequent stages: initial fast spreading, constant maximum droplet base and the shrinkage of the drop base; (ii) *complete wetting case* with only two stages: initial fast spreading and the shrinkage of the drop base. A system of two differential equations was derived for the case of complete wetting from the combination of a spherical cap spreading model over porous layer and a modified Darcy’s law for power law fluids. All experimental data fell on three universal curves independent of bloods with different haematocrit levels and n values under the dimensionless scale. The predicted theoretical results for complete

wetting cases were also three universal curves accounting quite satisfactory for the experimental data.

Wetting properties of the neutralized non-Newtonian Aculyn^{TM} 22 (A22) and Aculyn^{TM} 33 (A33) polymer solutions on dry hair tresses were studied experimentally in Chapter 5. Wetting behaviour on the dry undamaged hair tresses was drastically different between the two polymers and, in a first approximation, not directly linked with their bulk rheology. In the case of A22 the droplet spread and remained on the tress after spreading for at least half an hour, during which it slowly evaporated and possibly penetrated inside the hair. For A33 fast penetration of the droplet inside the hair tress was observed when the advancing contact angle reached a critical value of about 60^o. It was attributed to the so-called Cassie−Wenzel wetting transition, in which the liquid starts to penetrate inside the hair array.

A model for foam free drainage of power-law non-Newtonian liquids was presented in Chapter 6 which accounted for the drainage of A22 and A33 polymeric solutions. The predicted values showed that the decrease in the foam height and liquid content is very fast in the very beginning of the drainage; however, it reaches a steady state at long times. Under the assumption of rigid surface of the Plateau border, the predicted values of the time evolution of the foam height and liquid content were in good agreement with the measured experimental data especially for lowly viscose polymeric solutions. However, in the case of highly viscous solutions an interfacial mobility at the surface of the Plateau border has to be taken into account.

A model for drainage/imbibition of a foam placed on the top of a porous substrate was presented in Chapter 7. The equation of liquid imbibition into the porous substrate was coupled with foam drainage equation at the foam/porous substrate interface. The deduced dimensionless equations were solved using finite element method. It was found that the kinetics of foam drainage/imbibition depends on three dimensionless numbers and initial liquid volume fraction. The result showed that there are three different regimes of the process: (i) *rapid imbibition*: the liquid volume fraction inside the foam at foam/porous substrate interface remains constant close to a final liquid volume fraction; (ii) *intermediate imbibition*: the liquid volume fraction at the interface with porous substrate experiences a peak point and imbibition into the porous substrate is slower as compared with the drainage; (iii) *slow imbibition*: the liquid volume fraction at foam/porous substrate interface increases to a maximum limiting value and a free liquid layer is formed between the

foam and the porous substrate. However, the free liquid layer disappears after some time. The transition points between these three different drainage/imbibition regimes were delineated by introducing two dimensionless numbers.

8.2 Future work

In this section some recommendation for future researches are given in each of the above-mentioned area:

- It was shown in Chapter 3 that even in the case of equilibrium the deformation is more complex than it was assumed in earlier investigations. Note, there is a substantial problem here: experimental observation of equilibrium droplets on either non-deformable or deformable substrates is impossible, because according to Kelvin's equation, the droplets should be kept at equilibrium with oversaturated vapour for a prolonged period of time and the oversaturation should be kept constant with enormously high precision. This is currently beyond the experimental capabilities. It is the reason why only static advancing/receding contact angles can be experimentally observed on either non-deformable or deformable substrates. A theory of calculations of hysteresis contact angles was suggested only recently (cited in Chapter 3) on non-deformable solid substrates and has never been attempted in the case of deformable substrates. This is to be done in the future.
- A mathematical model was developed in Chapter 4 to describe wetting and spreading of non-Newtonian liquid droplets over a thin porous substrate in the case of complete wetting and the results were compared with the experimental data of the same process. However, to the best of our knowledge not only there is no available theory to describe the kinetics of wetting and spreading in the case of partial wetting, but the wetting of a thick porous medium is also challenging even in a complete wetting case. These are to be addressed in the future.
- Wetting and spreading of non-Newtonian A22 and A33 polymer solutions over dry hair tresses were studied experimentally in Chapter 5 and it was shown that unlike A33, the A22 droplets remains on the surface of the hair tress after the initial fast spreading stage. This behaviour was attributed to

the presence of a yield stress for A22 solutions. Although the effect of yield stress on wetting and spreading phenomena is an interesting topic, there is only limited number of investigations in this area and it requires to be comprehensively explored in the future.

- It was shown in Chapter 6 that the developed mathematical model for foam free drainage of power-law non-Newtonian liquids was in a good agreement with the measured experimental data especially in the case of lowly viscose polymeric solutions, and the small deviation between the theoretical predictions and experimental results in the case of highly viscose polymeric solutions was attributed to the assumption of immobile surface of the Plateau border and Poiseuille-like flow. It shows that in the case of highly viscous solutions an interfacial mobility at the surface of the Plateau border has to be incorporated in the mathematical model. This is to be done in the future.
- A completely new theory of foam drainage placed on the top of a porous substrate was presented in Chapter 7 for foams produced from Newtonian solutions. The current model can be developed to describe the drainage of foams produced from non-Newtonian solutions.

REFERENCES

(1) Barrat, J.; Hansen, J. In *Basic concepts for simple and complex liquids;* Cambridge University Press: 2003.

(2) Barth, W.; Hulek, K.; Peters, C.; Van de Ven, A. In *Compact complex surfaces;* Springer: 2015; Vol. 4.

(3) Meesters, R. J.; Hooff, G. P. State-of-the-Art Dried Blood Spot Analysis: An Overview of Recent Advances and Future Trends. *Bioanalysis* **2013**, *5*, 2187-2208.

(4) Lane, B. S.; Vohra, F.; Galazka, S. K.; Nally, K. M.; Agostino, E. H.; Kerr, G. S.; Lewis, R. D.; Lund, M. T.; McConaughy, S. D.; Smith III, E. D. , 2012.

(5) Zhao, Y.; Jones, S. A.; Brown, M. B. Dynamic Foams in Topical Drug Delivery. *Journal of Pharmacy and Pharmacology* **2010**, *62*, 678-684.

(6) Purdon, C. H.; Haigh, J. M.; Surber, C.; Smith, E. W. Foam Drug Delivery in Dermatology. *American Journal of Drug Delivery* **2003**, *1*, 71-75.

(7) Feldman, S. R.; Sangha, N.; Setaluri, V. Topical Corticosteroid in Foam Vehicle Offers Comparable Coverage Compared with Traditional Vehicles. *Journal of the American Academy of Dermatology* **2000**, *42*, 1017-1020.

(8) Huang, X.; Tanojo, H.; Lenn, J.; Deng, C. H.; Krochmal, L. A Novel Foam Vehicle for Delivery of Topical Corticosteroids. *Journal of the American Academy of Dermatology* **2005**, *53*, S26-S38.

(9) Stevens, M. M.; George, J. H. Exploring and Engineering the Cell Surface Interface. *Science* **2005**, *310*, 1135-1138.

(10) Pfohl, T.; Mugele, F.; Seemann, R.; Herminghaus, S. Trends in Microfluidics with Complex Fluids. *ChemPhysChem* **2003**, *4*, 1291-1298.

(11) Ghosh, S. K. In *Functional coatings: by polymer microencapsulation;* John Wiley & Sons: 2006.

(12) Ho, C.; Tai, Y. Micro-Electro-Mechanical-Systems (MEMS) and Fluid Flows. *Annual Review of Fluid Mechanics* **1998**, *30*, 579-612.

(13) Starov, V. M. Nonflat Equilibrium Liquid Shapes on Flat Surfaces. *Journal of Colloid and Interface Science* **2004**, *269*, 432-441.

(14) Starov, V. M.; Velarde, M. G.; Radke, C. J. In *Wetting and spreading dynamics;* CRC press: 2007; Vol. 138.

(15) Derjaguin, B.; Churaev, N.; Muller, V. In *Surface Forces*, Consultants Bureau—Plenum: New York, 1987.

(16) Churaev, N.; Sobolev, V. Wetting of Low-Energy Surfaces. *Advances in Colloid and Interface Science* **2007**, *134*, 15-23.

(17) Rowlinson, J. S.; Widom, B. In *Molecular theory of capillarity;* Courier Corporation: 2013.

(18) Starov, V. M.; Velarde, M. Surface Forces and Wetting Phenomena. *Journal of Physics: Condensed Matter* **2009**, *21*, 464121.

(19) Blake, T. D.; De Coninck, J. The Influence of solid–liquid Interactions on Dynamic Wetting. *Advances in Colloid and Interface Science* **2002**, *96*, 21-36.

(20) Blokhuis, E. M.; Widom, B. Wetting. *Current Opinion in Colloid & Interface Science* **1996**, *1*, 424-429.

(21) Boinovich, L.; Emelyanenko, A. Wetting and Surface Forces. *Advances in Colloid and Interface Science* **2011**, *165*, 60-69.

(22) De Gennes, P. Wetting: Statics and Dynamics. *Reviews of modern physics* **1985**, *57*, 827.

(23) Dussan, E. On the Spreading of Liquids on Solid Surfaces: Static and Dynamic Contact Lines. *Annual Review of Fluid Mechanics* **1979**, *11*, 371-400.

(24) Huh, C.; Scriven, L. E. Hydrodynamic Model of Steady Movement of a solid/liquid/fluid Contact Line. *Journal of Colloid and Interface Science* **1971**, *35*, 85-101.

(25) Lee, K.; Ivanova, N.; Starov, V.; Hilal, N.; Dutschk, V. Kinetics of Wetting and Spreading by Aqueous Surfactant Solutions. *Advances in Colloid and Interface Science* **2008**, *144*, 54-65.

(26) Starov, V.; Kalinin, V.; Chen, J. Spreading of Liquid Drops Over Dry Surfaces. *Advances in Colloid and Interface Science* **1994**, *50*, 187-221.

(27) Teletzke, G. F.; Ted Davis, H.; Scriven, L. How Liquids Spread on Solids. *Chemical Engineering Communications* **1987**, *55*, 41-82.

(28) Lu, G.; Wang, X.; Duan, Y. A Critical Review of Dynamic Wetting by Complex Fluids: From Newtonian Fluids to Non-Newtonian Fluids and Nanofluids. *Advances in Colloid and Interface Science* **2016**, *236*, 43-62.

(29) Ralston, J.; Popescu, M.; Sedev, R. Dynamics of Wetting from an Experimental Point of View. *Annual Review of Materials Research* **2008**, *38*, 23-43.

(30) Blake, T. D. The Physics of Moving Wetting Lines. *Journal of Colloid and Interface Science* **2006**, *299*, 1-13.

(31) Hervet, H.; De Gennes, P. The Dynamics of Wetting-Precursor Films in the Wetting of Dry Solids. *Comptes Rendus de l'Académie des Sciences Series Ii* **1984**, *299*, 499-503.

(32) Thompson, P. A.; Troian, S. M. A General Boundary Condition for Liquid Flow at Solid Surfaces. *Nature* **1997**, *389*, 360-362.

(33) Wayner Jr, P. C. Spreading of a Liquid Film with a Finite Contact Angle by the evaporation/condensation Process. *Langmuir* **1993**, *9*, 294-299.

(34) Weidner, D.; Schwartz, L. Contact-line Motion of Shear-Thinning Liquids. *Physics of Fluids* **1994**, *6*, 3535-3538.

(35) Carre, A.; Woehl, P. Spreading of Silicone Oils on Glass in Two Geometries. *Langmuir* **2006**, *22*, 134-139.

(36) Seppecher, P. Moving Contact Lines in the Cahn-Hilliard Theory. *International Journal of Engineering Science* **1996**, *34*, 977-992.

(37) Cox, R. The Dynamics of the Spreading of Liquids on a Solid Surface. Part 1. Viscous Flow. *Journal of Fluid Mechanics* **1986**, *168*, 169-194.

(38) Blake, T. Dynamic Contact Angles and Wetting Kinetics. *Wettability* **1993**, *49*, 251-309.

(39) Blake, T.; Haynes, J. Kinetics of Liquidliquid Displacement. *Journal of Colloid and Interface Science* **1969**, *30*, 421-423.

(40) Joanny, J.; De Gennes, P. Competition between Wetting and Adverse Macroscopic Forces. *Comptes Rendus de l'Académie des Sciences Series II* **1984**, *299*, 605-608.

(41) Briant, A.; Yeomans, J. Lattice Boltzmann Simulations of Contact Line Motion. II. Binary Fluids. *Physical Review E* **2004**, *69*, 031603.

(42) Briant, A.; Wagner, A.; Yeomans, J. Lattice Boltzmann Simulations of Contact Line Motion. I. Liquid-Gas Systems. *Physical Review E* **2004**, *69*, 031602.

(43) Qian, T.; Wang, X.; Sheng, P. A Variational Approach to Moving Contact Line Hydrodynamics. *Journal of Fluid Mechanics* **2006**, *564*, 333-360.

(44) Qian, T.; Wang, X.; Sheng, P. Molecular Scale Contact Line Hydrodynamics of Immiscible Flows. *Physical Review E* **2003**, *68*, 016306.

(45) Pomeau, Y. Recent Progress in the Moving Contact Line Problem: A Review. *Comptes Rendus Mecanique* **2002**, *330*, 207-222.

(46) Pismen, L. M.; Pomeau, Y. Disjoining Potential and Spreading of Thin Liquid Layers in the Diffuse-Interface Model Coupled to Hydrodynamics. *Physical Review E* **2000**, *62*, 2480.

(47) Jacqmin, D. Contact-Line Dynamics of a Diffuse Fluid Interface. *Journal of Fluid Mechanics* **2000**, *402*, 57-88.

(48) Chen, H.; Jasnow, D.; Viñals, J. Interface and Contact Line Motion in a Two Phase Fluid under Shear Flow. *Physical Review Letters* **2000**, *85*, 1686.

(49) Liu, C.; Bonaccurso, E.; Sokuler, M.; Auernhammer, G. K.; Butt, H. Dynamic Wetting of Polyisoprene Melts: Influence of the End Group. *Langmuir* **2009**, *26*, 2544-2549.

(50) Carré, A.; Eustache, F. Spreading Dynamics of a Shear Thinning Liquid. *Comptes Rendus de l'Academie des Sciences Series IIB* **1997**, *12*, 709-718.

(51) Ansini, L.; Giacomelli, L. Shear-Thinning Liquid Films: Macroscopic and Asymptotic Behaviour by Quasi-Self-Similar Solutions. *Nonlinearity* **2002**, *15*, 2147.

(52) Kistler, S. Hydrodynamics of Wetting. *Wettability* **1993**, *6*, 311-430.

(53) De Ruijter, M. J.; De Coninck, J.; Oshanin, G. Droplet Spreading: Partial Wetting Regime Revisited. *Langmuir* **1999**, *15*, 2209-2216.

(54) Brochard-Wyart, F.; De Gennes, P. Dynamics of Partial Wetting. *Advances in Colloid and Interface Science* **1992**, *39*, 1-11.

(55) Decamps, C.; De Coninck, J. Dynamics of Spontaneous Spreading Under Electrowetting Conditions. *Langmuir* **2000**, *16*, 10150-10153.

(56) Starov, V. M. Surface Forces Action in a Vicinity of Three Phase Contact Line and Other Current Problems in Kinetics of Wetting and Spreading. *Advances in Colloid and Interface Science* **2010**, *161*, 139-152.

(57) Starov, V.; Tyatyushkin, A.; Velarde, M.; Zhdanov, S. Spreading of Non-Newtonian Liquids Over Solid Substrates. *Journal of Colloid and Interface Science* **2003**, *257*, 284-290.

(58) Semenov, S.; Trybala, A.; Rubio, R. G.; Kovalchuk, N.; Starov, V.; Velarde, M. G. Simultaneous Spreading and Evaporation: Recent Developments. *Advances in Colloid and Interface Science* **2014**, *206*, 382-398.

(59) Betelu, S.; Fontelos, M. A. Capillarity Driven Spreading of Circular Drops of Shear-Thinning Fluid. *Mathematical and Computer Modelling* **2004**, *40*, 729-734.

(60) Wang, X.; Lee, D.; Peng, X.; Lai, J. Spreading Dynamics and Dynamic Contact Angle of Non-Newtonian Fluids. *Langmuir* **2007**, *23*, 8042-8047.

(61) Liang, Z.; Wang, X.; Duan, Y.; Min, Q. Energy-Based Model for Capillary Spreading of Power-Law Liquids on a Horizontal Plane. *Colloids and Surfaces A: Physicochemical and Engineering Aspects* **2012**, *403*, 155-163.

(62) Liang, Z.; Wang, X.; Duan, Y.; Min, Q.; Wang, C.; Lee, D. Dynamic Wetting of Non-Newtonian Fluids: Multicomponent Molecular-Kinetic Approach. *Langmuir* **2010**, *26*, 14594-14599.

(63) Alleborn, N.; Raszillier, H. Spreading and Sorption of a Droplet on a Porous Substrate. *Chemical engineering science* **2004**, *59*, 2071-2088.

(64) Kumar, S. M.; Deshpande, A. P. Dynamics of Drop Spreading on Fibrous Porous Media. *Colloids and Surfaces A: Physicochemical and Engineering Aspects* **2006**, *277*, 157-163.

(65) Starov, V.; Zhdanov, S.; Kosvintsev, S.; Sobolev, V.; Velarde, M. Spreading of Liquid Drops Over Porous Substrates. *Advances in Colloid and Interface Science* **2003**, *104*, 123-158.

(66) Bou-Zeid, W.; Brutin, D. Effect of Relative Humidity on the Spreading Dynamics of Sessile Drops of Blood. *Colloids and Surfaces A: Physicochemical and Engineering Aspects* **2014**, *456*, 273-285.

(67) Brutin, D.; Sobac, B.; Nicloux, C. Influence of Substrate Nature on the Evaporation of a Sessile Drop of Blood. *Journal of heat transfer* **2012**, *134*, 061101.

(68) Brutin, D.; Sobac, B.; Loquet, B.; Sampol, J. Pattern Formation in Drying Drops of Blood. *Journal of Fluid Mechanics* **2011**, *667*, 85-95.

(69) Sobac, B.; Brutin, D. Structural and Evaporative Evolutions in Desiccating Sessile Drops of Blood. *Physical Review E* **2011**, *84*, 011603.

(70) Exerowa, D.; Kruglyakov, P. M. In *Foams and foam films: Theory, experiment, application;* Studies in Interface Science; Elsevier: Amsterdam, 1998; Vol. 5.

(71) Farrokhpay, S. The Significance of Froth Stability in Mineral flotation—A Review. *Advances in colloid and interface science* **2011**, *166*, 1-7.

(72) Arzhavitina, A.; Steckel, H. Foams for Pharmaceutical and Cosmetic Application. *International journal of pharmaceutics* **2010**, *394*, 1-17.

(73) Weaire, D. L.; Hutzler, S. In *The physics of foams;* Oxford University Press: Oxford, 1999.

(74) Saint-Jalmes, A. Physical Chemistry in Foam Drainage and Coarsening. *Soft Matter* **2006**, *2*, 836-849.

(75) Kruglyakov, P. M.; Karakashev, S. I.; Nguyen, A. V.; Vilkova, N. G. Foam Drainage. *Current Opinion in Colloid & Interface Science* **2008**, *13*, 163-170.

(76) Kristen, N.; von Klitzing, R. Effect of Polyelectrolyte/surfactant Combinations on the Stability of Foam Films. *Soft Matter* **2010**, *6*, 849-861.

(77) Wierenga, P. A.; Gruppen, H. New Views on Foams from Protein Solutions. *Current Opinion in Colloid & Interface Science* **2010**, *15*, 365-373.

(78) Karakashev, S. I.; Grozdanova, M. V. Foams and Antifoams. *Advances in colloid and interface science* **2012**, *176*, 1-17.

(79) Farajzadeh, R.; Andrianov, A.; Krastev, R.; Hirasaki, G. J.; Rossen, W. R. Foam–oil Interaction in Porous Media: Implications for Foam Assisted Enhanced Oil Recovery. *Advances in Colloid and Interface Science* **2012**, *183–184*, 1-13.

(80) Stevenson, P. In *Foam engineering: fundamentals and applications;* John Wiley & Sons: 2012.

(81) Hudales, J. B. M.; Stein, H. N. The Influence of Solid Particles on Foam and Film Drainage. *Journal of Colloid and Interface Science* **1990**, *140*, 307-313.

(82) Ramani, M. V.; Kumar, R.; Gandhi, K. S. A Model for Static Foam Drainage. *Chemical Engineering Science* **1993**, *48*, 455-465.

(83) Bhakta, A. R.; Khilar, K. C. A Network Simulation for Drainage of Static Foam Columns. *Langmuir* **1991**, *7*, 1827-1832.

(84) Verbist, G.; Weaire, D. L. A Soluble Model for Foam Drainage. *EPL (Europhysics Letters)* **1994**, *26*, 631.

(85) Verbist, G.; Weaire, D. L.; Kraynik, A. M. The Foam Drainage Equation. *Journal of Physics: Condensed Matter* **1996**, *8*, 3715-3731.

(86) Jun, S.; Pelot, D. D.; Yarin, A. L. Foam Consolidation and Drainage. *Langmuir* **2012**, *28*, 5323-5330.

(87) Koehler, S. A.; Stone, H. A.; Brenner, M. P.; Eggers, J. Dynamics of Foam Drainage. *Physical Review E* **1998**, *58*, 2097.

(88) Sun, Q.; Tan, L.; Wang, G. Liquid Foam Drainage: An Overview. *International Journal of Modern Physics B* **2008**, *22*, 2333-2354.

(89) Weaire, D. L.; Pittet, N.; Hutzler, S.; Pardal, D. Steady-State Drainage of an Aqueous Foam. *Physical review letters* **1993**, *71*, 2670.

(90) Hutzler, S.; Weaire, D. L. Foam Coarsening under Forced Drainage. *Philosophical magazine letters* **2000**, *80*, 419-425.

(91) Stevenson, P. On the Forced Drainage of Foam. *Colloids and Surfaces A: Physicochemical and Engineering Aspects* **2007**, *305*, 1-9.

(92) Koehler, S. A.; Hilgenfeldt, S.; Stone, H. A. A Generalized View of Foam Drainage: Experiment and Theory. *Langmuir* **2000**, *16*, 6327-6341.

(93) Koehler, S. A.; Hilgenfeldt, S.; Stone, H. A. Flow along Two Dimensions of Liquid Pulses in Foams: Experiment and Theory. *EPL (Europhysics Letters)* **2001**, *54*, 335.

(94) Koehler, S. A.; Hilgenfeldt, S.; Stone, H. A. In *In Foam drainage in two dimensions: A comparison of experiment and theory for pulsed drainage;* Division of Fluid Dynamics Meeting; American Physical Society: 1999; Vol. 1.

(95) Cox, S. J.; Verbist, G. Liquid Flow in Foams under Microgravity. *Microgravity Science and Technology* **2003**, *14*, 45-52.

(96) Caps, H.; Cox, S. J.; Decauwer, H.; Weaire, D. L.; Vandewalle, N. Capillary Rise in Foams under Microgravity. *Colloids and Surfaces A: Physicochemical and Engineering Aspects* **2005**, *261*, 131-134.

(97) Weaire, D. L.; Hutzler, S.; Verbist, G.; Peters, E. In *A Review of Foam Drainage;* Prigogine, I., Rice, S. A., Eds.; Advances in Chemical Physics; John Wiley & Sons, Inc.: Hoboken, NJ, USA, 1997; Vol. 102.

(98) Saint-Jalmes, A.; Vera, M. U.; Durian, D. J. Free Drainage of Aqueous Foams: Container Shape Effects on Capillarity and Vertical Gradients. *EPL (Europhysics Letters)* **2000**, *50*, 695.

(99) Pitois, O.; Fritz, C.; Vignes-Adler, M. Liquid Drainage through Aqueous Foam: Study of the Flow on the Bubble Scale. *Journal of Colloid and Interface Science* **2005**, *282*, 458-465.

(100) Young, T. An Essay on the Cohesion of Fluids. *Philosophical Transactions of the Royal Society of London* **1805**, *95*, 65-87.

(101) Rusanov, A. Theory of Wetting of Elastically Deformed Bodies. 1. Deformation with a Finite Contact-Angle. *Colloid Journal of the USSR* **1975**, *37*, 614-622.

(102) Rusanov, A. Theory of Wetting of Elastically Deformed Bodies. 2. Equilibrium Conditions and Work of Deformation with a Finite Contact-Angle. *Colloid Journal of the USSR* **1975**, *37*, 623-628.

(103) Rusanov, A. On the Thermodynamics of Deformable Solid Surfaces. *Journal of Colloid and Interface Science* **1978**, *63*, 330-345.

(104) Shanahan, M. The Spreading Dynamics of a Liquid Drop on a Viscoelastic Solid. *Journal of Physics D: Applied Physics* **1988**, *21*, 981.

(105) Shanahan, M.; De Gennes, P. The Ridge Produced by a Liquid near the Triple Line Solid Liquid Fluid. *Comptes Rendus de l'Academie des Sciences Series II* **1986**, *302*, 517-521.

(106) Jerison, E. R.; Xu, Y.; Wilen, L. A.; Dufresne, E. R. Deformation of an Elastic Substrate by a Three-Phase Contact Line. *Physical Review Letters* **2011**, *106*, 186103.

(107) Park, S. J.; Weon, B. M.; San Lee, J.; Lee, J.; Kim, J.; Je, J. H. Visualization of Asymmetric Wetting Ridges on Soft Solids with X-Ray Microscopy. *Nature communications* **2014**, *5*.

(108) Schulman, R. D.; Dalnoki-Veress, K. Liquid Droplets on a Highly Deformable Membrane. *Physical Review Letters* **2015**, *115*, 206101.

(109) Shanahan, M.; Carre, A. Viscoelastic Dissipation in Wetting and Adhesion Phenomena. *Langmuir* **1995**, *11*, 1396-1402.

(110) Style, R. W.; Boltyanskiy, R.; Che, Y.; Wettlaufer, J.; Wilen, L. A.; Dufresne, E. R. Universal Deformation of Soft Substrates Near a Contact Line and the Direct Measurement of Solid Surface Stresses. *Physical Review Letters* **2013**, *110*, 066103.

(111) Style, R. W.; Che, Y.; Park, S. J.; Weon, B. M.; Je, J. H.; Hyland, C.; German, G. K.; Power, M. P.; Wilen, L. A.; Wettlaufer, J. S.; Dufresne, E. R. Patterning

Droplets with Durotaxis. *Proceedings of the National Academy of Sciences of the United States of America* **2013**, *110*, 12541-12544.

(112) Derjaguin, B.; Starov, V.; Churaev, N. Pressure on a Wetting Perimeter. *Colloid Journal of the USSR* **1982**, *44*, 770-775.

(113) Ahmed, G.; Kalinin, V. V.; Arjmandi-Tash, O.; Starov, V. M. Equilibrium of Droplets on a Deformable Substrate: Influence of Disjoining Pressure. *Colloids and Surfaces A: Physicochemical and Engineering Aspects* **2016**, In Press.

(114) Winkler, E. Die Lehre Von Der Elastizität Und Festigkeit (the Theory of Elasticity and Stiffness). *H. Dominicus Prague, Czechoslovakia* **1867**.

(115) Churaev, N. V.; Starov, V.; Derjaguin, B. The Shape of the Transition Zone between a Thin Film and Bulk Liquid and the Line Tension. *Journal of Colloid and Interface Science* **1982**, *89*, 16-24.

(116) Chao, T. C.; Arjmandi-Tash, O.; Das, D. B.; Starov, V. M. Simultaneous Spreading and Imbibition of Blood Droplets Over Porous Substrates in the Case of Partial Wetting. *Colloids and Surfaces A: Physicochemical and Engineering Aspects* **2015**.

(117) Chao, T. C.; Arjmandi-Tash, O.; Das, D. B.; Starov, V. M. Spreading of Blood Drops Over Dry Porous Substrate: Complete Wetting Case. *Journal of Colloid and Interface Science* **2015**, *446*, 218-225.

(118) Chao, T. C.; Trybala, A.; Starov, V.; Das, D. B. Influence of Haematocrit Level on the Kinetics of Blood Spreading on Thin Porous Medium during Dried Blood Spot Sampling. *Colloids and Surfaces A: Physicochemical and Engineering Aspects* **2014**, *451*, 38-47.

(119) Starov, V.; Kostvintsev, S.; Sobolev, V.; Velarde, M.; Zhdanov, S. Spreading of Liquid Drops Over Dry Porous Layers: Complete Wetting Case. *Journal of Colloid and Interface Science* **2002**, *252*, 397-408.

(120) Starov, V.; Kosvintsev, S.; Sobolev, V.; Velarde, M.; Zhdanov, S. Spreading of Liquid Drops Over Saturated Porous Layers. *Journal of Colloid and Interface Science* **2002**, *246*, 372-379.

(121) Bird, R. B.; Stewart, W. E.; Lightfoot, E. N. In *Transport phenomena;* John Wiley & Sons: 2007.

(122) Rungjiratananon, W.; Kanamori, Y.; Nishita, T. In *In Wetting effects in hair simulation;* Computer Graphics Forum; Wiley Online Library: 2012; Vol. 31, pp 1993-2002.

(123) Zviak, C. In *The science of hair care;* Informa Health Care: 1986.

(124) Lodge, R. A.; Bhushan, B. Wetting Properties of Human Hair by Means of Dynamic Contact Angle Measurement. *Journal of Applied Polymer Science* **2006**, *102*, 5255-5265.

(125) Molina, R.; Comelles, F.; Juliá, M. R.; Erra, P. Chemical Modifications on Human Hair Studied by Means of Contact Angle Determination. *Journal of Colloid and Interface Science* **2001**, *237*, 40-46.

(126) Kamath, Y. K.; Dansizer, C. J.; Weigmann, H. -. Wetting Behavior of Human Hair Fibers. *Journal of Applied Polymer Science* **1978**, *22*, 2295-2306.

(127) Feughelman, M. In *Mechanical properties and structure of alpha-keratin fibres: wool, human hair and related fibres;* UNSW press: 1997.

(128) Robbins, C. In *Chemical and physical behaviour of human hair*, 3rd ed.; Springer-Verlag: New York, 1994.

(129) Dupres, V.; Langevin, D.; Guenoun, P.; Checco, A.; Luengo, G.; Leroy, F. Wetting and Electrical Properties of the Human Hair Surface: Delipidation Observed at the Nanoscale. *Journal of Colloid and Interface Science* **2007**, *306*, 34-40.

(130) AnonymousAculyn22-Technical Data Sheet-Dow. http://www.dow.com/assets/attachments/business/pcare/aculyn/aculyn_22/tds/aculyn22.pdf.

(131) AnonymousAculyn33-Technical Data Sheet-Dow. http://www.dow.com/assets/attachments/business/pcare/aculyn/aculyn_33/tds/aculyn33.pdf.

(132) Bureiko, A.; Trybala, A.; Huang, J.; Kovalchuk, N.; Starov, V. Bulk and Surface Rheology of Aculyn™ 22 and Aculyn™ 33 Polymeric Solutions and

Kinetics of Foam Drainage. *Colloids and Surfaces A: Physicochemical and Engineering Aspects* **2013**, *43*4, 268-275.

(133) Bureiko, A.; Trybala, A.; Huang, J.; Kovalchuk, N.; Starov, V. Effects of Additives on the Foaming Properties of Aculyn 22 and Aculyn 33 Polymeric Solutions. *Colloids and Surfaces A: Physicochemical and Engineering Aspects* **2014**, *46*0, 265-271.

(134) Trybala, A.; Bureiko, A.; Kovalchuk, N.; Arjmandi-Tash, O.; Liu, Z.; Starov, V. Wetting Properties of Cosmetic Polymeric Solutions on Hair Tresses. *Colloids and Interface Science Communications* **2015**, 9, 12-15.

(135) Bico, J.; Thiele, U.; Quéré, D. Wetting of Textured Surfaces. *Colloids and Surfaces A: Physicochemical and Engineering Aspects* **2002**, *20*6, 41-46.

(136) Bormashenko, E.; Musin, A.; Whyman, G.; Zinigrad, M. Wetting Transitions and Depinning of the Triple Line. *Langmuir* **2012**, *2*8, 3460-3464.

(137) Barbieri, L.; Wagner, E.; Hoffmann, P. Water Wetting Transition Parameters of Perfluorinated Substrates with Periodically Distributed Flat-Top Microscale Obstacles. *Langmuir* **2007**, *23*, 1723-1734.

(138) Bormashenko, E.; Grynyov, R. Plasma Treatment Induced Wetting Transitions on Biological Tissue (Pigeon Feathers). *Colloids and Surfaces B: Biointerfaces* **2012**, *92*, 367-371.

(139) Sarma, D. S. R.; Pandit, J.; Khilar, K. C. Enhancement of Stability of Aqueous Foams by Addition of Water-Soluble polymers—measurements and Analysis. *Journal of Colloid and Interface Science* **1988**, *124*, 339-348.

(140) Schramm, L. L. In *Surfactants: fundamentals and applications in the petroleum industry;* Cambridge University Press: 2000.

(141) Friberg, S. E.; Fang, J. Foams from Aqueous Systems of Polymerizable Surfactants. *Journal of Colloid and Interface Science* **1987**, *118*, 543-552.

(142) Klitzing, R. v.; Müller, H. Film Stability Control. *Current opinion in colloid & interface science* **2002**, *7*, 42-49.

(143) Safouane, M.; Saint-Jalmes, A.; Bergeron, V.; Langevin, D. Viscosity Effects in Foam Drainage: Newtonian and Non-Newtonian Foaming Fluids. *The European Physical Journal E* **2006**, *19*, 195-202.

(144) Safouane, M.; Durand, M.; Saint Jalmes, A.; Langevin, D.; Bergeron, V. Aqueous Foam Drainage. Role of the Rheology of the Foaming Fluid. *Le Journal de Physique IV* **2001**, *11*, Pr6-275-Pr6-280.

(145) Bureiko, A.; Trybala, A.; Kovalchuk, N.; Starov, V. Current Applications of Foams Formed from Mixed surfactant–polymer Solutions. *Advances in Colloid and Interface Science* **2015**, *222*, 670-677.

(146) Arjmandi-Tash, O.; Trybala, A.; Mahdi, F. M.; Kovalchuk, N. M.; Starov, V. Foams Built Up by Non-Newtonian Polymeric Solutions: Free Drainage. *Colloids and Surfaces A: Physicochemical and Engineering Aspects* **2016**, In Press.

(147) Wang, Z.; Narsimhan, G. Model for Plateau Border Drainage of Power-Law Fluid with Mobile Interface and its Application to Foam Drainage. *Journal of Colloid and Interface Science* **2006**, *300*, 327-337.

(148) Arjmandi-Tash, O.; Kovalchuk, N.; Trybala, A.; Starov, V. Foam Drainage Placed on a Porous Substrate. *Soft matter* **2015**, *11*, 3643-3652.

(149) Bhakta, A.; Ruckenstein, E. Decay of Standing Foams: Drainage, Coalescence and Collapse. *Advances in Colloid and Interface Science* **1997**, *70*, 1-124.

(150) Narsimhan, G. A Model for Unsteady State Drainage of a Static Foam. *J. Food Eng.* **1991**, *14*, 139-165.

(151) Magrabi, S.; Dlugogorski, B.; Jameson, G. Free Drainage in Aqueous Foams: Model and Experimental Study. *AIChE J.* **2001**, *47*, 314-327.

(152) Magrabi, S.; Dlugogorski, B.; Jameson, G. Bubble Size Distribution and Coarsening of Aqueous Foams. *Chemical engineering science* **1999**, *54*, 4007-4022.

(153) Carrier, V.; Colin, A. Coalescence in Draining Foams. *Langmuir* **2003**, *19*, 4535-4538.

(154) Bibette, J.; Morse, D.; Witten, T.; Weitz, D. Stability Criteria for Emulsions. *Physical Review Letters* **1992**, *69*, 2439.

(155) Khristov, K.; Exerowa, D.; Minkov, G. Critical Capillary Pressure for Destruction of Single Foam Films and Foam: Effect of Foam Film Size. *Colloids and Surfaces A: Physicochemical and Engineering Aspects* **2002**, *210*, 159-166.

(156) Van Hecke, M. Jamming of Soft Particles: Geometry, Mechanics, Scaling and Isostaticity. *Journal of Physics: Condensed Matter* **2010**, *22*, 033101.

(157) Maestro, A.; Drenckhan, W.; Rio, E.; Höhler, R. Liquid Dispersions under Gravity: Volume Fraction Profile and Osmotic Pressure. *Soft Matter* **2013**, *9*, 2531-2540.

(158) Kornev, K. G.; Neimark, A. V.; Rozhkov, A. N. Foam in Porous Media: Thermodynamic and Hydrodynamic Peculiarities. *Advances in Colloid and Interface Science* **1999**, *82*, 127-187.

(159) Zitha, P. L. Foam Drainage in Porous Media. *Transport in Porous Media* **2003**, *52*, 1-16.

(160) Zitha, P. L.; Nguyen, Q. P.; Currie, P. K.; Buijse, M. A. Coupling of Foam Drainage and Viscous Fingering in Porous Media Revealed by X-Ray Computed Tomography. *Transport in Porous Media* **2006**, *64*, 301-313.

(161) Zitha, P. L.; Vermolen, F. J. Self-Similar Solutions for the Foam Drainage Equation. *Transport in Porous Media* **2006**, *63*, 195-200.

(162) Danov, K. D.; Valkovska, D. S.; Kralchevsky, P. A. Hydrodynamic Instability and Coalescence in Trains of Emulsion Drops Or Gas Bubbles Moving through a Narrow Capillary. *Journal of Colloid and Interface Science* **2003**, *267*, 243-258.

(163) Singh, G.; Hirasaki, G. J.; Miller, C. A. Dynamics of Foam Films in Constricted Pores. *AIChE Journal* **1997**, *43*, 3241-3252.

(164) Bureiko, A.; Arjmandi-Tash, O.; Kovalchuk, N.; Trybala, A.; Starov, V. Interaction of Foam with a Porous Medium: Theory and Calculations. *The European Physical Journal Special Topics* **2015**, *224*, 459-471.

(165) Bolton, F.; Weaire, D. L. Rigidity Loss Transition in a Disordered 2D Froth. *Physical Review Letters* **1990**, *65*, 3449-3451.

(166) Van Hecke, M. Jamming of Soft Particles: Geometry, Mechanics, Scaling and Isostaticity. *Journal of Physics: Condensed Matter* **2010**, *22*, 033101.

(167) Grassia, P.; Cilliers, J.; Neethling, S.; Ventura-Medina, E. Quasi-One-Dimensional Foam Drainage. *The European Physical Journal E* **2001**, *6*, 325-348.

(168) Carman, P. Permeability of Saturated Sands, Soils and Clays. *The Journal of Agricultural Science* **1939**, *29*, 262-273.

(169) Sochi, T. Non-Newtonian Flow in Porous Media. *Polymer* **2010**, *51*, 5007-5023.